1-13-2017

Nonlinear Optical Processes for Spectral Broadening and Short Pulse Generation

Hongyu Hu
University of Connecticut, boyhhy88@gmail.com

Nonlinear Optical Processes for Spectral Broadening and Short Pulse Generation

Hongyu Hu, PhD

University of Connecticut, 2017

The dramatic progress in optical communication is attributed to the development of wavelength-division multiplexing and time-division multiplexing technologies, which employ broadband light source and ultrashort optical pulses respectively to carry signals in optical fibers. Supercontinuum generation is the spectral broadening of narrow-band incident pulses by the propagation through optical waveguides made of nonlinear materials. In this PhD dissertation, I show the design of a tapered lead-silicate optical fiber for supercontinuum generation. The physical mechanisms of optical pulse evolution are explained, which involve various nonlinear optical effects including self-phase and cross-phase modulation, stimulated Raman scattering, four-wave mixing, modulation instability and optical soliton dynamics. I have also proposed planar waveguides with longitudinally varying structure to manage chromatic dispersion, and numerically simulated the generation of (1) broadband and (2) flat octave-spanning supercontinuum output. The coherence property and noise sensitivity of supercontinuum are also investigated in this dissertation, which depend strongly on pumping conditions. A hybrid mode-locked erbium-doped fiber ring laser, which combines rational harmonic active mode-locking technique and graphene saturable absorber, has been designed and experimentally demonstrated to produce optical pulse train. Compared to active mode-locking configuration, the hybrid scheme narrows the pulse width significantly at a high repetition rate of 20 GHz.

Nonlinear Optical Processes for Spectral Broadening and Short Pulse Generation

Hongyu Hu

B.S., Harbin Institute of Technology, Harbin, China, 2011

M.S., University of Connecticut, Storrs, CT, USA, 2013

A Dissertation

Submitted in Partial Fulfillment of the

Requirements for the Degree of

Doctor of Philosophy

at the

University of Connecticut

2017

APPROVAL PAGE

Doctor of Philosophy Dissertation

Nonlinear Optical Processes for Spectral Broadening and Short Pulse Generation

Presented by

Hongyu Hu, B.S., M.S.

Major Advisor _____
Niloy K. Dutta

Associate Advisor _____
Boris Sinkovic

Associate Advisor _____
Peter Schweitzer

University of Connecticut
2017

Acknowledgement

First of all, I would like to express my sincere gratitude to my major advisor, Dr. Niloy K. Dutta, for his continuous guidance, assistance, patience and encouragement during my PhD study. He has provided me with not only valuable scientific advice on research work, but also insightful suggestions on life outside the lab. Without his support and contributions of time and ideas, my graduate experience would not be so productive.

I would like to thank all the members of my advisory committee, Dr. Menka Jain, Dr. Jason Hancock, Dr. Boris Sinkovic, Dr. Peter Schweitzer, Dr. Gayanath Fernando and Dr. Alexander Kovner, for their kind support and helpful comments on my doctoral dissertation.

I would like to thank the present and former members of Dr. Dutta's research group. During the early years, Dr. Shaozhen Ma helped me a lot in adapting to new circumstances and taking the first step towards success in scientific research. Working with Dr. Wenbo Li and Mr. Xiang Zhang, both of whom are smart and brilliant scientists, is always enjoyable.

I would like to extend my appreciation to my friends in the Physics Department: Mr. Di Shu, Mr. Zhiwei Zhang, Mr. Shiqi Yin, Mr. Yiteng Tian, Mr. Cheng Tu, Dr. Hui Chen, Dr. Jia Wang, Mr. Thomas Dodge, Mr. James Dragan, and Mr. Martin Disla. They have been so friendly and I spent so many unforgettable days with them.

Last but not least, I would like to thank my family. I couldn't be more grateful to my parents for their understanding and all of the sacrifices they have made. I also want to send my gratitude to

my girlfriend Xuan Guo. Without her love and support I couldn't have gone through all the difficulties and got what I have achieved today.

TABLE OF CONTENTS

Chapter 1 Introduction

This introductory chapter is intended to provide an overview of fiber optic communication. In Section 1.1, a brief description of fiber optic communication will be provided. Section 1.2 discusses the application of supercontinuum light source and high speed pulsed laser source in optical communication systems. In section 1.3, a brief overview of the entire thesis work will be introduced.

1.1 A Brief Description of Optical Communications

The earliest attempts of optical communication go back thousands of years. In the old time, people in North America and China used smoke as the transmitted signal. In the second half of twentieth century, the development of lasers opened the world of optical communication to new possibilities, since light has an information-carrying capacity 10,000 times that of the highest radio frequencies being used. However, the challenge was that open-air transmission was quite sensitive to environmental conditions. In 1966, Charles Kao and Charles Hockham working at the Standard Telecommunication Laboratory in England proposed a dielectric fiber with a refractive index higher than its surrounding region to be a possible medium for the guided transmission of light [1]. Since then, optical fiber communication technologies have made great strides, and different types of fibers suitable for different situations have been invented. Compared to electrical cables, the most important advantages of using optical fibers are high capacity, low transmission loss, easiness to be reamplified over long distance, low cost, light weight, and immunity to electromagnetic interference. Typically, optical communication operates in three “telecom windows”: 850 nm, 1310 nm and 1550 nm, as illustrated in Figure 1.1. In these regions, conventional silica fibers experience low loss (as low as 0.2 dB/km) [2]. Today, the C

band (1530-1565 nm) near 1550 nm is widely used for long-haul transmission, and L band near 1625 nm is being developed.

The simplest optical fiber communication system is a fiber-optic link composed of transmitters, optical fibers, and receivers. The transmitters are generally diode lasers or LED, which convert electrical signals to optical signals coupled into fibers. At the receiver end, photodetectors convert the optical signals back to electrical signals. Semiconductor or fiber amplifiers (i.e., erbium-doped fiber) are also used to maintain sufficient signal power level after long transmission distance. Moreover, in order to transmit and process digital information more efficiently, different devices such as all-optical Boolean logic gates have been used to replace electrical circuits [3-11].

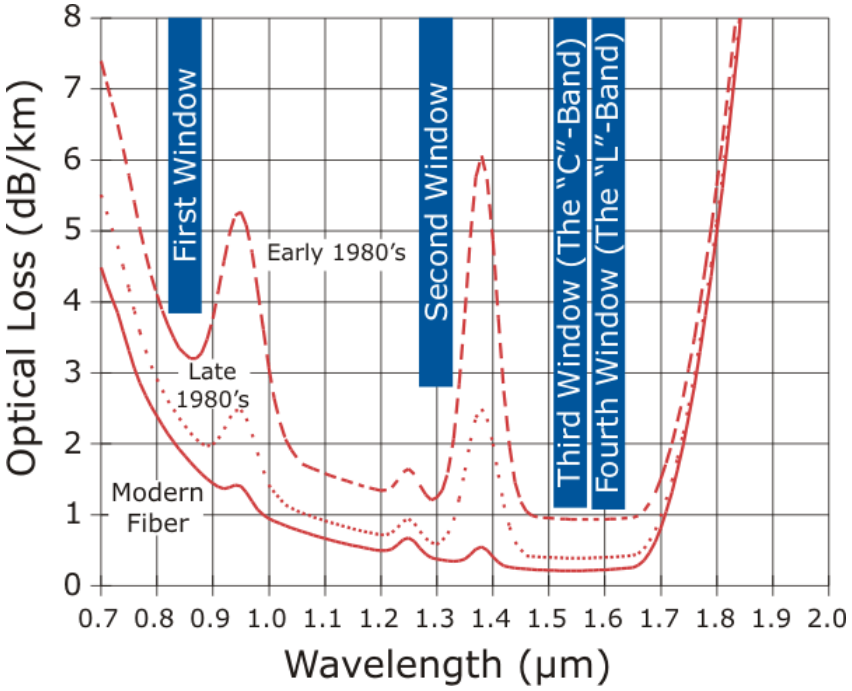

Figure 1.1 Telecom windows of conventional silica fibers.

1.2 Broadband Light Source and Pulsed Laser Source for Optical Communications

So far the optical network capacity has reached over 100 Tb/s in laboratory/research demonstrations, while commercial system capacity record is around 10 Tb/s [12]. The dramatic progress is attributed to the introduction of wavelength-division multiplexing (WDM) technology, which employs distinct wavelength channels to carry information in a single fiber. Supercontinuum (SC) is a promising broadband light source for WDM optical communication system. Supercontinuum generation (SCG) is the spectral broadening of narrow-band incident pulses by the propagation through nonlinear media [13]. SC can be produced by pulses from mode-locked lasers, and it provides an effective way to obtain a large number of wavelength channels while maintaining coherence from pulse to pulse. Generally, SC with broad bandwidth, low noise and high spectral flatness is required for WDM application.

Besides, supercontinuum with a spectrum extending further into the mid-infrared region can be utilized in many other applications such as molecular spectroscopy, microscopy and laser radar. For instance, the "molecular fingerprint region" covers from ~2 μm up to more than 10 μm, and broadband SC has become an attract source for molecular spectroscopy due to its high brightness.

The generation of ultrashort optical pulses is also crucial for high-speed optical communication, especially in time-division multiplexing technology, where several optical pulse train signals modulated at the bit rate B using the same carrier frequency are multiplexed optically to form a composite optical signal at a bit rate of NB in which N is the number of multiplexed optical channels. With increased repetition rate, the pulse-to-pulse spacing is narrower, which can lead to

overlap between adjacent pulses. This is detrimental for data transmission. Therefore, the pulse duration should be sufficiently small to ensure the pulses stay cleanly separated. Recently the use of graphene saturable absorbers in fiber lasers has been a topic of great interest due to the advantages of fast response and broadband operation [14-15].

1.3 Overview of This Thesis

In this doctoral dissertation, I present my research work on all-optical devices including supercontinuum generator and short pulse generator, based on nonlinear optical effects. These devices are theoretically simulated or experimentally demonstrated. Three important properties of supercontinuum generation have been paid close attention to: bandwidth, flatness and coherence. In Chapter 2, I numerically simulate the spectral and temporal evolution of supercontinuum generated in a dispersion-tailored lead-silicate fiber taper with progressively increased core size. Starting from the generalized nonlinear schrödinger equation which governs pulse propagation in optical waveguides, the detailed mechanisms of supercontinuum generation have been discussed, and a collection of linear and nonlinear effects is taken into account, including optical loss, dispersion, self-phase modulation, cross-phase modulation, soliton dynamics, dispersive wave emission, stimulated Raman scattering, four-wave mixing and modulation instability. Broadband output spectrum extending to 4.8 μm is demonstrated, which is caused by the emission of dispersive waves towards longer wavelengths.

In Chapter 3, a tapered planar waveguide is designed and theoretically studied for the generation of supercontinuum with large bandwidth. The Air-SF57 glass-SiO_2 rib waveguide is 2-cm long, with a varying etched depth to manage the total chromatic dispersion. Numerical simulations are

conducted for input pulses at a center wavelength of 1.55 μm, and the proposed waveguide geometry greatly broadens the output spectrum extending from ~1.0 μm to ~ 4.6 μm, resulting from continuous modification of phase matching condition.

In Chapter 4, the coherence property of supercontinuum generated in dispersion-varying optical waveguides is investigated. Simulations are conducted by adding quantum noise seeds into the input pulse field, and the complex degree of first-order coherence function and the overall spectral coherence degree are both calculated. Although the spectral broadening is generally comparable, the coherence degree is shown to vary with different pumping conditions. It decreases with higher peak power and longer pulse width due to the significant competition between soliton-fission process and the noise-seeded modulation instability effect. By controlling the input pulse parameters, it is possible to generate perfectly coherent supercontinuum.

In Chapter 5, a tapered planar waveguide is designed to generate octave-spanning supercontinuum with good flatness in the mid-infrared region. The rib waveguide of lead-silicate glass on silica is 1.8-cm long consisting of a segment with longitudinally changing height. The mechanism involves nonlinear soliton dynamics. The dispersion profile is shifted along the propagation distance, which overcomes the spectral unevenness caused by the gap between solitons and dispersive wave components. With low input pulse energy of 45 pJ, simulation demonstrates the generation of both broadband and flat near-octave spectrum spanning 1.3-2.5 μm at -20 dB level.

In Chapter 6, a hybrid mode-locked erbium-doped fiber ring laser which is easy to set up is proposed and experimentally demonstrated to generate a high-repetition-rate optical pulse train with ultrashort pulse width. The laser combines second-order rational harmonic mode-locking, which is realized via an intra-cavity $LiNbO_3$ Mach-Zehnder modulator, and a graphene passive mode locker. Compared to solely active mode-locking scheme, the hybrid scheme narrows the pulse width by a factor of 0.53 to 2.82 ps at the repetition rate of 20 GHz with 0.52-mW average output power. Numerical simulation of the laser performance is also provided, which shows good agreement with the experimental results.

Chapter 2 Supercontinuum Evolution in Microstructured Fiber Taper

2.1 Introduction

Supercontinuum generation (SCG) is the spectral broadening of narrow-band incident pulses when a collection of nonlinear processes act together upon the pulses in optical waveguides [1, 2]. In recent years, SCG has been a topic of great interest to researchers due to its diverse applications in frequency metrology, optical coherence tomography (OCT), pulse compression, dense wavelength division multiplexing (DWDM) and many others. The physical mechanism of supercontinuum (SC) has been demonstrated to be a combination of linear and nonlinear processes including self-phase modulation (SPM), cross-phase modulation (XPM), stimulated Raman scattering (SRS), four-wave mixing (FWM), modulation instability (MI), soliton dynamics and dispersive wave radiation, on the basis of the waveguide properties (dispersion, nonlinearity and loss).

Recent progress in dispersion-engineering technique has shown that the dispersion profile can be controlled by varying the structure and dimension of optical fibers, especially after the advent of photonic crystal fibers (PCFs) and microstructured optical fibers (MOFs), which has provided great opportunities for broadband SC [3-6]. For example, in [6] it was experimentally demonstrated that anomalous dispersion can be obtained at wavelengths well below 600 nm using air-silica PCFs. Based on this principle, highly nonlinear tapered fibers with longitudinally-varying dispersion can be devised to generate broadband supercontinuum more efficiently[7-9]. In [7], a PCF with continuously-decreasing zero-dispersion wavelength was fabricated, which successfully extended the generation of supercontinuum spectra from the visible into the ultraviolet range.

In this chapter I theoretically investigate the mechanisms of supercontinuum evolution in a lead-silicate microstructured fiber taper. The core size of the fiber increases gradually along the propagation distance, and by pumping optical pulses with center wavelength of 1.55 μm, peak power of 6 kW and FWHM of 100 fs, broadband output extending to 4.8 μm can be obtained due to continuous emission of dispersive waves towards longer wavelengths.

2.2 Physical Mechanisms of Supercontinuum Generation

To fully understand the physical mechanisms of supercontinuum generation, we need to take into account a variety of linear and nonlinear optical phenomena, such as loss, dispersion, self-phase and cross-phase modulation, soliton dynamics, stimulated Raman scattering, four-wave mixing and modulation instability. Mathematically, all the effects are involved in the generalized nonlinear Schrödinger equation, which is the fundamental formula that governs optical pulse propagation in nonlinear media.

2.2.1 Generalized Nonlinear Schrödinger Equation

The theory of nonlinear fiber optics describes the behavior of light traveling through dispersive nonlinear media, which is the basis of supercontinuum generation. Typically, nonlinear phenomena take effect when the intensity of the input optical pulse is so high that the dielectric polarization P is not a linear function of the external electric field E. In order to investigate these phenomena, the time-domain generalized nonlinear Schrödinger equation (GNLSE) has been derived from the Maxwell's equations, which models the pulse evolution:

$$\frac{\partial A}{\partial z}+\frac{\alpha}{2}A+\sum_{k>=2}\frac{i^{k-1}}{k!}\beta_k\frac{\partial^k A}{\partial T^k}=i\gamma\left(1+\frac{i}{\omega_0}\frac{\partial}{\partial T}\right)\left(A\int_{-\infty}^{+\infty}R(T')\left|A(z,T-T')\right|^2dT'\right) \tag{2.2.1}$$

Here, A(z, T) is the pulse envelope, assumed to be a slowly varying function of the propagation distance z. T represents the time. α is the propagation loss, β_k are the Taylor series coefficients of the wave number β, γ is a measure of nonlinearity, and R(T) is the nonlinear response function. These parameters will be further discussed in the upcoming sections. It can be seen that the left-hand side of GNLSE models the linear effects, while the right-hand side indicates the nonlinear effects. Importantly, the key assumption is that the pulse propagation is unidirectional so that any backward wave as well as nonlinear coupling between forward and backward waves is neglected. Under specific conditions (pulse width is long enough), if we ignore the loss α and high-order terms of β_k, the GNLSE will be simplified as:

$$\mathrm{i}\frac{\partial A}{\partial z}=\frac{\beta_2}{2}\frac{\partial^2 A}{\partial T^2}-\gamma|A|^2 A \tag{2.2.2}$$

which has exactly the same form as the Schrödinger equation with a nonlinear potential. This is why equation (2.2.1) is referred to as the GNLSE.

In the frequency domain, we can do Fourier transform for the envelop A(z, T):

$$A(z,T)=F^{-1}\{A(z,\omega-\omega_0)\}=\frac{1}{2\pi}\int_{-\infty}^{+\infty}A(z,\omega-\omega_0)\exp[-i(\omega-\omega_0)T]d\omega \tag{2.2.3}$$

$$A(z,\omega)=F\{A(z,T)\}=\frac{1}{2\pi}\int_{-\infty}^{+\infty}A(z,T)\exp[i(\omega-\omega_0)T]dT \tag{2.2.4}$$

For the nonlinear part, letting

$$g(z,T)=A\int_{-\infty}^{+\infty}R(T')\left|A(z,T-T')\right|^2 dT' \tag{2.2.5}$$

$$g(z,T)=F^{-1}\{g(z,\omega-\omega_0)\}=\frac{1}{2\pi}\int_{-\infty}^{+\infty}g(z,\omega-\omega_0)\exp[-i(\omega-\omega_0)T]d\omega \tag{2.2.6}$$

$$g(z,\omega)=F\{g(z,T)\}=\frac{1}{2\pi}\int_{-\infty}^{+\infty}g(z,T)\exp[i(\omega-\omega_0)T]dT \tag{2.2.7}$$

Substitute equations (2.2.3) and (2.2.6) into (2.2.1), we have:

$$\frac{\partial A(z,T)}{\partial z} = \frac{1}{2\pi}\int_{-\infty}^{+\infty}\left[\frac{\partial}{\partial z}A(z,\omega-\omega_0)\right]\exp[-i(\omega-\omega_0)T]d\omega \tag{2.2.8}$$

$$\frac{\alpha}{2}A = \frac{1}{2\pi}\int_{-\infty}^{+\infty}\frac{\alpha}{2}A(z,\omega-\omega_0)\exp[-i(\omega-\omega_0)T]d\omega \tag{2.2.9}$$

$$\begin{aligned}
&\sum_{k>=2}\frac{i^{k-1}}{k!}\beta_k\frac{\partial^k A}{\partial T^k} \\
&= \sum_{k>=2}\frac{i^{k-1}}{k!}\beta_k\frac{1}{2\pi}\int_{-\infty}^{+\infty}A(z,\omega-\omega_0)[-i(\omega-\omega_0)]^k\exp[-i(\omega-\omega_0)T]d\omega \\
&= \sum_{k>=2}-i\frac{1}{2\pi}\int_{-\infty}^{+\infty}A(z,\omega-\omega_0)\frac{1}{k!}\beta_k(\omega-\omega_0)^k\exp[-i(\omega-\omega_0)T]d\omega \\
&= \frac{1}{2\pi}\int_{-\infty}^{+\infty}-i\left[\beta-\beta_0-\beta_1(\omega-\omega_0)\right]A(z,\omega-\omega_0)\exp[-i(\omega-\omega_0)T]d\omega
\end{aligned} \tag{2.2.10}$$

$$\begin{aligned}
&i\gamma\left(1+\frac{i}{\omega_0}\frac{\partial}{\partial T}\right)g(z,T) \\
&= i\gamma\frac{1}{2\pi}\int_{-\infty}^{+\infty}g(z,\omega-\omega_0)\left[1-\frac{i}{\omega_0}i(\omega-\omega_0)\right]\exp[-i(\omega-\omega_0)T]d\omega \\
&= \frac{1}{2\pi}\int_{-\infty}^{+\infty}i\gamma g(z,\omega-\omega_0)\frac{\omega}{\omega_0}\exp[-i(\omega-\omega_0)T]d\omega
\end{aligned} \tag{2.2.11}$$

Therefore, if we change the variable

$$A'(z,\omega) = A(z,\omega)\exp(-L(\omega)z) \tag{2.2.12}$$

where

$$L(\omega) = i\left[\beta-\beta_0-\beta_1(\omega-\omega_0)\right]-\frac{\alpha}{2} \tag{2.2.13}$$

is the linear operator, we finally obtain the frequency-domain GNLSE:

$$\frac{\partial A'}{\partial z} = i\gamma\frac{\omega}{\omega_0}\exp(-Lz)F\left[A\int_{-\infty}^{+\infty}R(T')\left|A(z,T-T')\right|^2dT'\right] \tag{2.2.14}$$

and $|\tilde{A}(z,\omega)|^2$ gives the spectral power. Either equation (2.2.1) or (2.2.14) can be used to model the pulse propagation in optical waveguides.

Different numerical methods have been developed to solve the GNLSE. One of them that has

been extensively utilized is the split-step Fourier method (SSFM). The basic idea of SSFM is to treat the linear and nonlinear effects separately, so equation (2.2.1) can be written as:

$$\frac{\partial A}{\partial z} = \left(D + N\right) A \tag{2.2.15}$$

where

$$D = -\frac{\alpha}{2} - \sum_{k>=2} \frac{i^{k-1}}{k!} \beta_k \frac{\partial^k}{\partial T^k} \tag{2.2.16}$$

$$N = \frac{1}{A} i\gamma \left(1 + \frac{i}{\omega_0} \frac{\partial}{\partial T}\right) \left(A \int_{-\infty}^{+\infty} R(T') \left|A(z, T - T')\right|^2 dT'\right) \tag{2.2.17}$$

are the linear (consisting of loss and dispersion) and nonlinear operators, respectively. Assume that linear and nonlinear effects act independently within a small distance h, the solution of equation (2.2.15) becomes

$$A(z + h, T) = \exp(hD) \exp(hN) A(z, T) \tag{2.2.18}$$

More specifically, in the first step, the nonlinear operator N acts alone to the pulse, and the outcome is computed directly in the time domain using equation (2.2.17); in the second step, only the linear operator D takes effect, and the calculation is done in the frequency domain since $\partial^k/\partial T^k$ in equation (2.2.16) can be simply replaced by $[-i(\omega-\omega_0)]^k$. Fourier transform for the pulse envelop A(z,T) needs to be applied back and forth in each small step h, and the accuracy of the split-step Fourier method is proportional to h^2.

Another approach to solve the GNLSE is to integrate the propagation equation (2.2.14) directly using ordinary differential equation integrators (ODEs). It should be noted that the numerical solution is obtained on a temporal grid of discrete points, which should be adjusted carefully so that the span of the grid covers the maximum time delay of the propagating pulse while the

density of the grid is large enough to include the maximum frequency. In order to justify the correctness of the simulation results making use of ODEs, it should be checked whether the conservation of specific quantities (e.g., number of photons) is satisfied and whether significant variance in the result is observed with stricter tolerance.

2.2.2 Optical Losses

The parameter α in the GNLSE measures the total transmission loss from all sources. If the input power of P_0 is injected into a waveguide with length L, the output power is given by $P_0e^{-\alpha L}$. Figure 2.1 shows the typical wavelength-dependent attenuation of a standard single-mode silica fiber. On the short-wavelength side, material absorption is dominated by Rayleigh scattering, inversely proportional to fourth power of the wavelength. The small peak around 1.4 μm is caused by impurities (OH^- ions). Figure 2.2 shows the loss spectrum of various glass materials extended into far-infrared region. The transparency limit on the long-wavelength side is determined by multi-phonon absorption, which results from the coupling of two or more vibration modes. With weaker chemical bonds in the material, the absorption edge can be pushed towards longer wavelengths. As a result, any glass composed of silica (such as SF57 in Figure 2.2) is not transparent beyond 5 μm due to the Si-O bonding. Besides linear loss, nonlinear loss comes into play when the photon energy exceeds half of the band gap, leading to two-photon absorption (TPA). In this case, loss is related to the light intensity, and it can significantly limit propagation of high-intensity light and slow down nonlinear processes. For silica glass with large band gap, the TPA effect can be ignored at wavelengths around 1.55 μm.

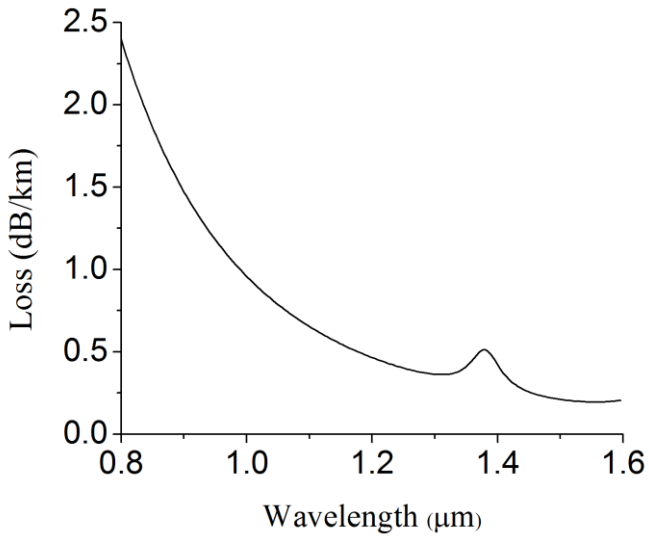

Figure 2.1 Typical Loss profile of a single-mode silica fiber.

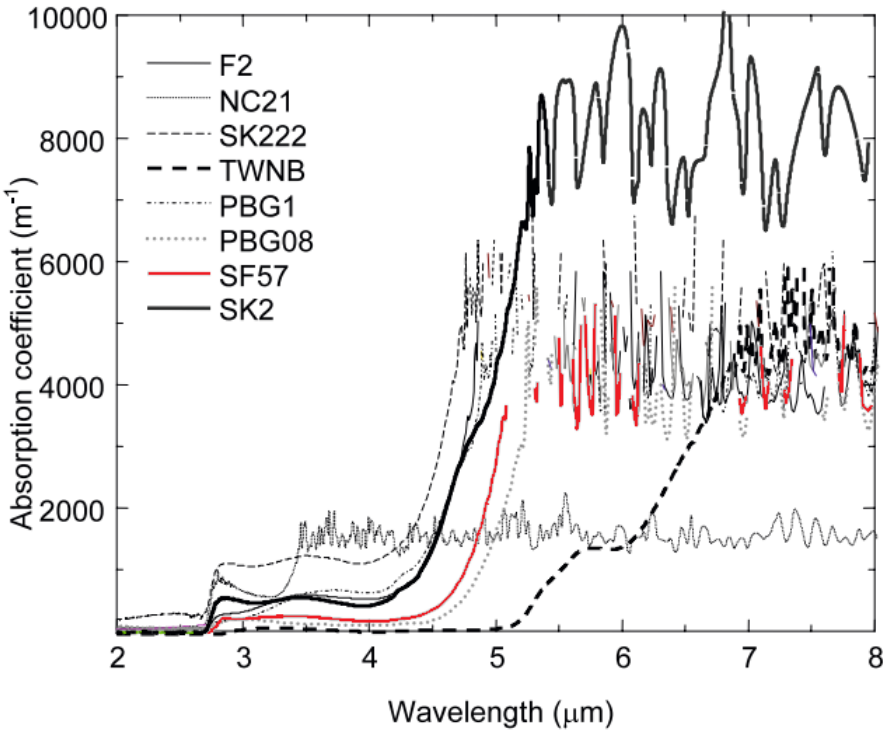

Figure 2.2 Loss profiles and multi-phonon absorption edges of different glass materials.

In addition to the intrinsic material property, the waveguide structure can also contribute to optical losses, such as bending loss and confinement loss. Confinement loss arises due to the finite area of the cladding region, so the electric field leaks out of the waveguide. Nonetheless, it can be greatly reduced by ensuring sufficiently large cladding area. Therefore, with proper waveguide design, the total loss is dominated by the material transmission window with absorption edges on the short-wavelength and long-wavelength sides.

2.2.3 Dispersion

Dispersion is a linear effect, but it has great impact on nonlinear effects. Dispersion occurs because the effective refractive index of the guided mode depends on the frequency of light. This means different frequency components of light travel at different speeds. If the propagation constant is β, the angular frequency is ω and the effective mode index is n_{eff}, then we can expand β into Taylor series around the center frequency ω_0 of the input pulse:

$$\beta(\omega) = n_{\text{eff}}(\omega)\frac{\omega}{c} = \sum_{k>=0}\frac{1}{k!}\beta_k\left(\omega-\omega_0\right)^k \tag{2.2.19}$$

$$\beta_k = \left(\frac{d^m\beta}{d\omega^m}\right)_{\omega=\omega_0} \tag{2.2.20}$$

β_1 is related to the group velocity v_g and group index n_g by $\beta_1=1/v_g=n_g/c$ in which c is the speed of light in vacuum. The pulse envelop travels at the group velocity, and in the GNLSE we have used a retarded reference frame moving with pulse at v_g by making the transformation $T=t-z/v_g=t-\beta_1 z$. $\beta_2=d\beta_1/d\omega$ represents the group velocity dispersion (GVD):

$$\beta_2 = \frac{1}{c}\left(2\frac{dn_{eff}}{d\omega}+\omega\frac{d^2n_{eff}}{d\omega^2}\right) \tag{2.2.21}$$

Alternatively, if the wavelength is λ, the dispersion parameter D is also used to quantify GVD:

$$D = \frac{d\beta_1}{d\lambda} = -\frac{2\pi c}{\lambda^2}\beta_2 = -\frac{\lambda}{c}\frac{d^2 n_{eff}}{d\lambda^2} \tag{2.2.22}$$

Figure 2.3 shows the group velocity dispersion of a standard single-mode silica fiber as a function of wavelength. As can be seen in the figure, the total dispersion depends on both the material property and the waveguide design. In fact, sufficiently strong waveguiding can overcome the material dispersion to significantly modify the total dispersion behavior. The wavelength at which GVD is zero is called the zero dispersion wavelength (ZDW). As shown in Figure 2.3, ZDW is approximately 1.3 μm for standard single-mode fibers. In the region where $D<0$ ($\beta_2>0$), the waveguide exhibits normal dispersion, which infers that higher frequencies move slower than lower frequencies. On the contrary, when $D>0$ ($\beta_2<0$), the waveguide exhibits anomalous dispersion, and higher frequencies move faster than lower frequencies. High order terms of β_k controls the dispersion profile. For example, β_3 results in the wavelength dependence of GVD, and β_4 results in the formation of more than one ZDWs.

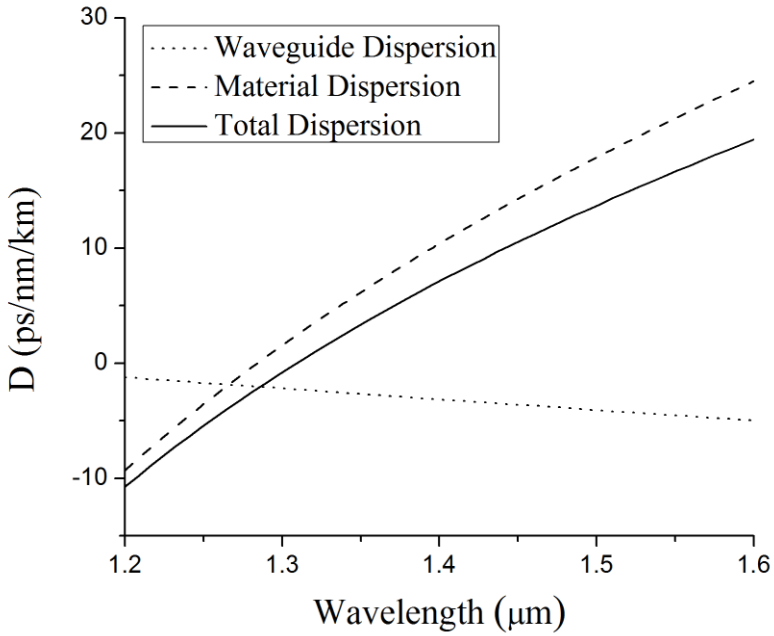

Figure 2.3 Group velocity dispersion of standard single-mode silica fiber with the contribution of material and waveguide.

GVD effect is responsible for chirp and pulse broadening. The chirp of an optical pulse is the change in the instantaneous frequency with time. For normal dispersion, the components of pulse with smaller frequencies travel faster and arrive earlier at the output of the waveguide. As a result, an increase in the frequency can be observed at the output, and the dispersion is said to impose positive chirp on the pulse. On the other hand, anomalous dispersion makes the pulse negatively chirped. Obviously, the delay in the arrival of different frequency components also leads to pulse broadening. Regardless of the sign of the dispersion parameter D, an initially unchirped pulse will be temporally broadened with the spectrum unchanged.

In the above discussion, we have only considered chromatic dispersion. Due to birefringence, the effective mode index n_{eff} changes with different polarization directions, which is defined as polarization-mode dispersion. The effective mode index also varies for higher-order transverse modes, which is referred to as "intermodal dispersion".

2.2.4 Self-Phase and Cross-Phase Modulation

Self-phase modulation (SPM) and cross-phase modulation (XPM) are nonlinear optical phenomena originated from Kerr effect, which describes the response of the material refractive index to the applied electric field as:

$$n(I) = n_0 + n_2 I \tag{2.2.23}$$

where n_0 is the linear refractive index, I is the intensity of the field, and the parameter n_2 is defined as the nonlinear refractive index. Since the total phase of the field is equal to $\omega_0 t - nkL$, in which $k=2\pi/\lambda$ is the wave number, the nonlinear part of the refractive index introduces extra nonlinear phase shift as:

$$\phi_{nl} = n_2 IkL = \frac{2\pi n_2 IL}{\lambda} \tag{2.2.24}$$

As a consequence, a shift in the instantaneous frequency is produced, which can be obtained by:

$$\Delta\omega = -\frac{d\phi_{nl}}{dt} = -\frac{2\pi n_2 L}{\lambda}\frac{dI}{dt} \tag{2.2.25}$$

Consider the case of an incident Gaussian pulse such that the intensity is proportional to $\exp(-t^2/\tau^2)$. Figure 2.4 depicts the pulse profile and frequency shift. At the leading edge of the pulse, the frequency is down-shifted, whereas at the trailing edge, the frequency is up-shifted. This draws a conclusion that nonlinear refraction brings both time dependent phase delay and chirp to the pulse. For an initially unchirped pulse, the temporal pulse envelop will remain the same while the spectrum is broadened. Across the center of the pulse, the chirp is positive and approximately linear. Such effect is referred to as self-phase modulation (SPM). If a co-propagating pulse is affected by nonlinear refraction in the same way, the phenomenon is referred to as cross-phase modulation (XPM).

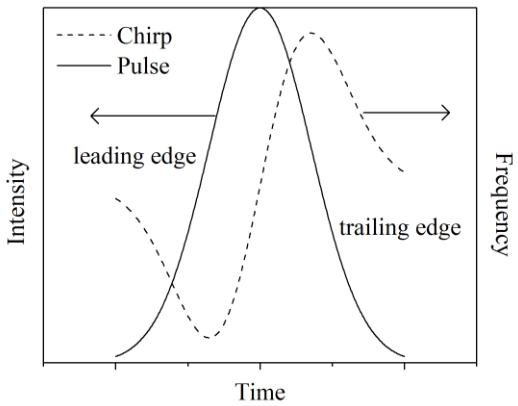

Figure 2.4 Gaussian pulse profile and frequency shift due to nonlinear refraction.

Given the nonlinear refractive index n_2, the nonlinear parameter γ in the GNLSE is written as:

$$\gamma = \frac{n_2 \omega_0}{c A_{eff}} \tag{2.2.26}$$

where A_{eff} is the guided mode area. The nonlinear parameter is a measure of the strength of nonlinearity. Note that if A_{eff} is smaller, the pulse intensity will be higher to enhance nonlinear effects.

In reality, dispersion will simultaneously act on the pulse. In the normal dispersion regime, since the chirps produced by SPM and dispersion are both positive, the pulse gets broadened temporally. This can also be understood by the fact that the leading edge is red-shifted and travels faster than the blue-shifted trailing edge. In the anomalous dispersion regime, dispersion and SPM act in the opposite way, and they may eventually balance with each other to form optical solitons.

2.2.5 Optical Solitons

In the anomalous dispersion regime of an optical waveguide, the interplay of dispersion and SPM can reach an equilibrium state, and the resulting pulse becomes an optical soliton. The order of the soliton is determined by:

$$N = \sqrt{\frac{L_D}{L_{NL}}} = \sqrt{\frac{\gamma P \tau^2}{|\beta_2|}} \tag{2.2.27}$$

$$L_D = \frac{\tau^2}{|\beta_2|} \tag{2.2.28}$$

$$L_{NL} = \frac{1}{\gamma P} \tag{2.2.29}$$

Here, P is the pulse peak power and τ is the pulse width. L_D and L_{NL} are the dispersion length and

nonlinear length characterizing the distance over which dispersion and nonlinearity play a significant role for pulse propagation, respectively. For example, if the propagation distance $L \gg L_D$ but $L \sim L_{NL}$, pulse evolution is dominated by SPM; whereas if $L \gg L_{NL}$ but $L \sim L_D$, pulse evolution is dominated by GVD. For fundamental solitons, $N = 1$ ($L_{NL} = L_D$), and the effect of GVD cancels that of SPM. In this case, the solution of the GNLSE (if only GVD and SPM are involved) is a hyperbolic-secant pulse with unchanged temporal and spectral profiles during propagation.

When $N \geq 2$, the input pulse will form a high-order soliton. The temporal and spectral profiles will change during propagation, but follow a periodic behavior so that the pulse recovers to its original shape at multiples of a specific length known as the soliton period. It should be noted that $L_{NL} < L_D$ in this case, hence SPM dominates the pulse propagation at the first stage, and GVD will catch up afterwards. Therefore, at the initial phase the high-order soliton always experiences spectral broadening and temporal compression, which has been used in applications such as pulse compression and supercontinuum. However, a high-order soliton is essentially an unstable bound state of N fundamental solitons with the same group velocities. With the perturbation of high-order dispersion or Raman scattering, the pulse can break up into a series of N fundamental solitons. This is called the soliton fission process and it occurs when the original high-order soliton reaches its maximum bandwidth at the distance of $L_{fiss} \sim L_D/N$. The fundamental solitons are ejected one by one, the first one with highest peak power and shortest pulse width. But again, due to the perturbation of high-order dispersion and Raman scattering, such ideal soliton fission process does not occur in practice, especially when the solitons are close to the zero dispersion wavelength; instead, some of the soliton power will be transferred

across the ZDW to the normal dispersion regime to generate dispersive waves (DWs). The DWs are narrow-band, and it is necessary for the DW frequency ω_{DW} to satisfy the phase-matching condition:

$$\frac{\gamma P_{\text{sol}}}{2} = \sum_{k\geq 2} \frac{\beta_k(\omega_{sol})}{k!}\left(\omega_{DW} - \omega_{sol}\right)^k \tag{2.2.30}$$

where ω_{sol} and P_{sol} are the frequency and peak power of the emitted solitons respectively. The left side of equation (2.2.30) is actually the wave number of solitons, and the right side is the wave number of DW. If we only keep GVD and third-order dispersion, the phase-matching condition becomes:

$$\frac{\gamma P_{\text{sol}}}{2} = \frac{\beta_2(\omega_{sol})}{2}\left(\omega_{DW} - \omega_{sol}\right)^2 + \frac{\beta_3(\omega_{sol})}{6}\left(\omega_{DW} - \omega_{sol}\right)^3 \tag{2.2.31}$$

Obviously, the left side of the equation is positive, and the first term on the right is negative since solitons are only formed in anomalous dispersion regime so that $\beta_2(\omega_{\text{sol}})$ is a negative value. This implies that dispersive wave emission can never take place without the involvement of higher-order dispersion. If $\beta_3(\omega_{\text{sol}}) < 0$, dispersive waves are emitted at smaller frequencies (longer wavelengths), whereas if $\beta_3(\omega_{\text{sol}}) > 0$, dispersive waves are emitted at greater frequencies (shorter wavelengths), as shown in Figure 2.5. It turns out that if the wavelength of the soliton gets closer to the ZDW, the phase-matched DW is also closer to the ZDW, and its intensity increases exponentially.

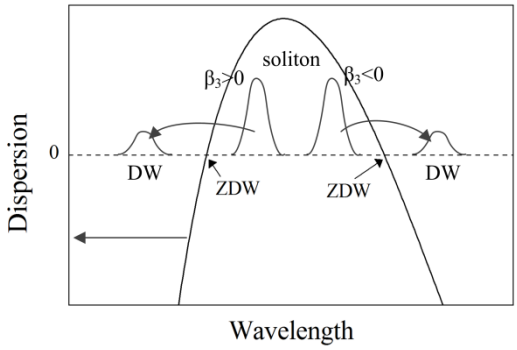

Figure 2.5 Dispersive waves emitted in the normal dispersion regime by solitons in the anomalous dispersion regime. Two conditions are considered: $\beta_3(\omega_{sol}) < 0$ and $\beta_3(\omega_{sol}) > 0$.

2.2.6 Stimulated Raman Scattering

Besides nonlinear refraction, stimulated Raman scattering (SRS) is another class of nonlinear effects. SRS is a result of the interaction between photons and phonons (atomic or molecular vibration modes). During the process, a photon of the input field is annihilated and its energy is transferred to the nonlinear medium to excite a phonon. At the same time, a photon with lower frequency is created to ensure the conservation of both energy and momentum.

The nonlinear response function R(T) in the GNLSE is written as:

$$R(T) = (1 - f_R)\delta(T) + f_R h_R(T) \tag{2.2.32}$$

The delta function represents the instantaneous electronic response (Kerr effect), while $h_R(T)$ represents the delayed ionic response (Raman scattering). f_R denotes the fraction of the Raman contribution to nonlinearity. Substitute equation (2.2.32) into the integral in the GNLSE (2.2.1), we have:

$$\begin{aligned}
&\int_{-\infty}^{+\infty} R(T')\left|A(z,T-T')\right|^2 dT' \\
&= \int_{-\infty}^{+\infty}\left[(1-f_R)\delta(T')\left|A(z,T-T')\right|^2 + f_R h_R(T')\left|A(z,T-T')\right|^2\right]dT' \\
&= (1-f_R)\left|A(z,T)\right|^2 + f_R\int_{-\infty}^{+\infty} h_R(T')\left|A(z,T-T')\right|^2 dT'
\end{aligned} \tag{2.2.33}$$

Experimental measurements show that for lots of materials $h_R(T)$ can be fit using a damped oscillation model:

$$h_R(T) = \frac{\tau_1^2 + \tau_2^2}{\tau_1 \tau_2^2} \exp(-\frac{T}{\tau_2}) \sin(\frac{T}{\tau_1}) \tag{2.2.34}$$

For silica fibers, τ_1=12.2 fs, τ_2=32 fs, and f_R is about 0.18.

SRS is responsible for soliton self-frequency shift (SSFS). If the bandwidth of a soliton is broad enough to overlap the Raman gain spectrum, the frequency of the soliton will be down-shifted, thus the soliton will move towards longer wavelengths. This phenomenon is also known as the intrapulse Raman scattering. The rate of SSFS can be reduced and eventually halted when loss and dispersion come into play. Assuming a dispersion profile with two ZDWs similar to the one shown in Figure 2.5, a red-shifted soliton is either moving away from the first ZDW with $\beta_3 > 0$ or approaching the second ZDW with $\beta_3 < 0$. In the former case, the increased dispersion will tend to broaden the pulse temporally, so it does not have sufficient bandwidth to cover the Raman gain spectrum; in the latter case, SSFS can be canceled by soliton recoil, which is due to saturation of the exponential amplification of dispersive waves. The influence of propagation loss is to decrease the soliton's intensity, and the reduction in nonlinearity will cause the pulse to broaden temporally and limit Raman self-frequency shift.

2.2.7 Four-Wave Mixing and Modulation Instability

Four-wave mixing (FWM) is a nonlinear effect originated from third-order susceptibility. When propagating in a nonlinear medium, two pump waves with frequencies ω_1 and ω_2 will be converted into a pair of sidebands at $\omega_3=2\omega_1-\omega_2$ and $\omega_4=2\omega_2-\omega_1$ under the influence of FWM. In particular, degenerate four-wave mixing occurs if a single pump wave is launched so that $\omega_1=\omega_2$.

The generation of new frequency components leads to strong spectral broadening, which is advantageous for applications such as supercontinuum generation. In fact, FWM plays a major role in supercontinuum mechanisms when the input pulse width is large and the soliton order is high ($N \gg 10$).

In the time domain, FWM results in the fluctuation of the electric field, with the modulation period corresponding to the frequency separation between the pump and the sidebands. Moreover, a high-order soliton or even a continuous wave can split into fundamental soliton pulses by the amplification of background noise at the sidebands, and the duration of the subpulses is comparable to the modulation period. This is referred to as modulation instability (MI). It can be seen that although FWM and MI are discussed in different domains (frequency and time), they actually have the same underlying physics. Note that the pulse breakup effect of FWM/MI is similar to that of soliton fission, but since FWM/MI is a noise-driven process, the generated new frequency components are expected to be incoherent, so the spectrum possesses poor stability performance when MI dominates over soliton fission during pulse evolution.

2.3 Design of Dispersion-Tailored Lead-Silicate Fiber Taper

In this section we will design a microstructured fiber taper for broadband supercontinuum generation. In recent years, the development of microstructured optical fibers has made it possible to achieve novel optical properties, such as engineered dispersion and high nonlinearity. Microstructured fibers are generally separated into two classes: holey fibers and photonic bandgap fibers. Unlike traditional optical fibers, photonic bandgap fibers make use of the photonic bandgap effect to achieve light confinement in hollow core[10]. We will focus our

attention upon the other category of microstructured fibers, holey fibers, in which light is guided by a modified form of total internal reflection. Holey fibers are fabricated with a solid core surrounded by an array of air holes, which effectively reduces the cladding refractive index, as illustrated in Figure 2.6. The incorporation of air not only eliminates the need for dopants to modify the refractive index, but also achieves much higher index contrast between core and cladding. As shown in Figure 2.6, the air holes with a diameter of d are spaced by a distance of Λ, leading to a core size of 2Λ-d. The properties of the holey fibers are determined by the parameter d/Λ. If d/Λ is large, the index contrast between the core and cladding is high, which results in strong waveguide dispersion and modal confinement. Therefore, the material dispersion can be greatly compensated, and the zero GVD wavelength is shifted towards shorter wavelengths. Furthermore, according to equation (2.2.26), tight modal confinement gives rise to reduction in the effective mode area A_{eff} and thus enhancement of nonlinearity. One can notice that when the air-filling fraction reaches unity, $d/\Lambda=1$, and the microstructured fiber is essentially a solid core completely surrounded by air cladding.

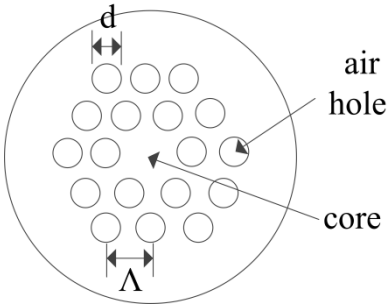

Figure 2.6 Structure of a holey fiber. The core area is surrounded by air holes, with hole size d and hole spacing Λ.

The optical properties of microstructured fibers can further be controlled by utilizing fiber

tapering technique. The transverse dimension of a tapered fiber varies along the length with a high degree of accuracy, and both dispersion and nonlinearity depend on the propagation distance. Sometimes tapered fiber also refers to nanowire, which is fabricated by stretching the original fiber to make it thinner. But the dimension is still constant along the length, and we are not interested in such nanowires in the context. Interestingly, it turns out that if the transition of the transverse dimension is sufficiently slow, the guided mode can be adiabatically transformed during light transmission. Tapered fibers are often used for mode matching between different optical waveguides, for example, light from a conventional single-mode fiber can be coupled into a nanowire through a fiber taper. In recent years, tapers fibers have also shown remarkable prospect in supercontinuum generation.

We propose a tapered SF57 fiber structure as illustrated in Figure 2.7. Scott SF57 is a commercially available lead-silicate soft glass material primarily composed of SiO_2 and PbO, with a Pb cationic content of 40-50% [11]. The linear refractive index of SF57 is 1.80 at 1.55 μm, compared to 1.44 of silica [12]. The nonlinear refractive index measured at 1.06 μm is 4.1×10^{-19} m^2/W, much higher than that of pure silica fibers [13]. As shown in Figure 2.2, the infrared absorption edge is located at ~5 μm. In addition, compared to heavy metal oxide and chalcogenide glasses, SF57 offers higher thermal and crystallization stability and a less steep viscosity curve, while exhibiting low softening temperature[14]. For this reason, SF57 glass has drawn much attention and been widely used to fabricate microstructured fibers.

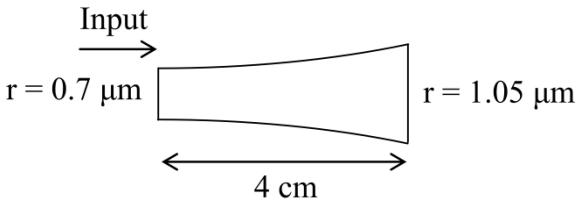

Figure 2.7 The schematic of SF57 fiber taper, with the core radii of 0.7 μm and 1.05 μm at the input and output respectively.

The tapered SF57 glass fiber is 4-cm long, and its core size continuously increases along the propagation length z with the relationship given by:

$$r(z) = r_0(1+\frac{z}{z_0})^3 \tag{2.3.1}$$

where r_0=0.7 μm and z_0=27.6 cm. The radius of the core area changes from 0.7 μm at the input to 1.05 μm at the output. The effective mode area at the input turns out to be ~3.5 μm^2 at the wavelength of 1.55 μm.

We have calculated the total dispersion of SF57 fiber as a function of wavelength for the fundamental HE11 mode using the step-index waveguide model, as shown in Figure 2.8 and 2.9. The material dispersion is plotted for comparison, with the ZDW at ~1.97 μm. As discussed before, the total chromatic dispersion is the combination of material and waveguide dispersion. This is illustrated in Figure 2.8, where we provide two examples corresponding to radii of 1.2 μm and 0.85 μm, respectively. Figure 2.9 depicts the total dispersion profiles for several distinct core sizes from 1.4 μm to 0.7 μm. It can be seen that the waveguide dispersion is significantly affected by modifying the transverse dimension, which compensates the material dispersion and allows for control of the total spectral dispersion property. Specifically, with smaller core size, the ZDW is shifted towards shorter wavelengths, and when the radius shrinks to less than 1μm, a

second zero dispersion point is formed at long wavelength side, which is also shifted to shorter wavelengths with reduced core dimension.

Hyperbolic secant pulses at telecommunications wavelength of 1.55 μm are injected into the fiber taper to generate broadband supercontinuum. In order to simulate the pulse evolution, we numerically solve the generalized nonlinear Schrödinger equation given by (2.2.1), and take into account the dependence of dispersion and nonlinear variables on propagation distance. The parameters used to characterize the input pulse are peak power and full width at half maximum (FWHM). Experimentally, a mode-locked erbium-doped fiber laser can act as the pump source. It should be noted that the input wavelength of 1.55 μm is in the anomalous dispersion regime of the fiber, so soliton dynamics is expected to play an essential role in the supercontinuum mechanism.

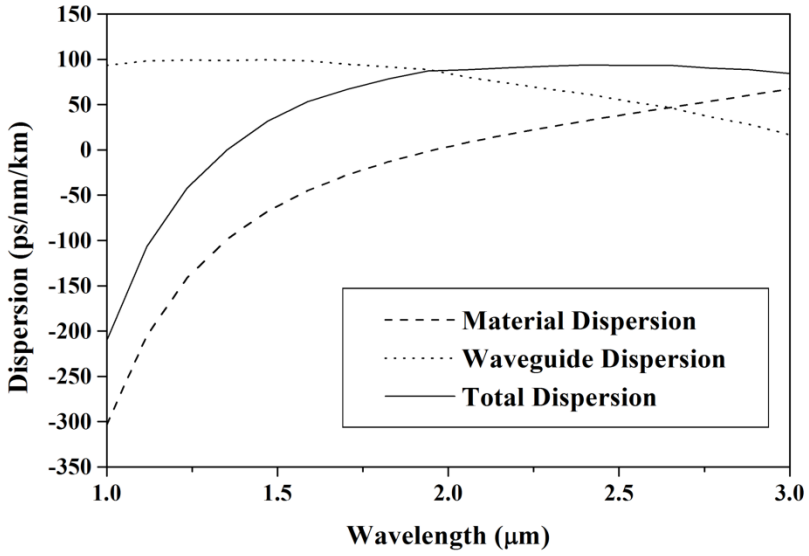

(a)

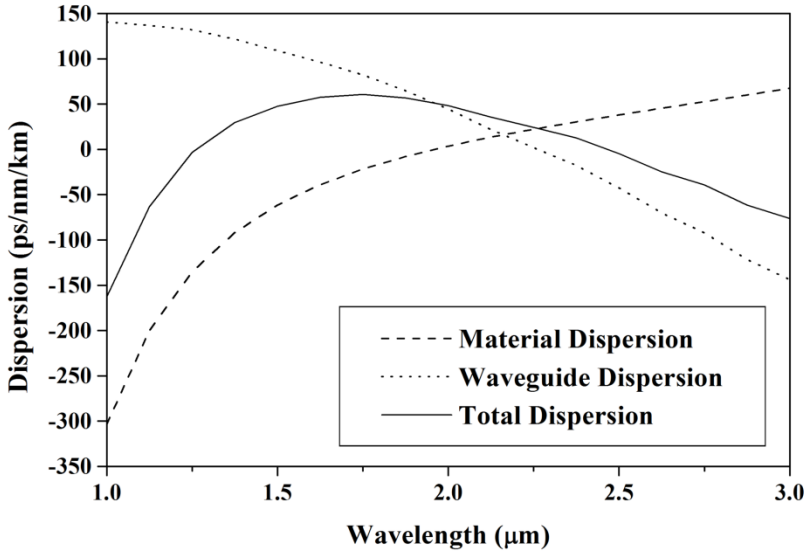

(b)

Figure 2.8 Dispersion curves for SF57 fiber with core radii of (a) 1.2 μm, and (b) 0.85 μm. The total dispersion is a combination of both material and waveguide dispersion.

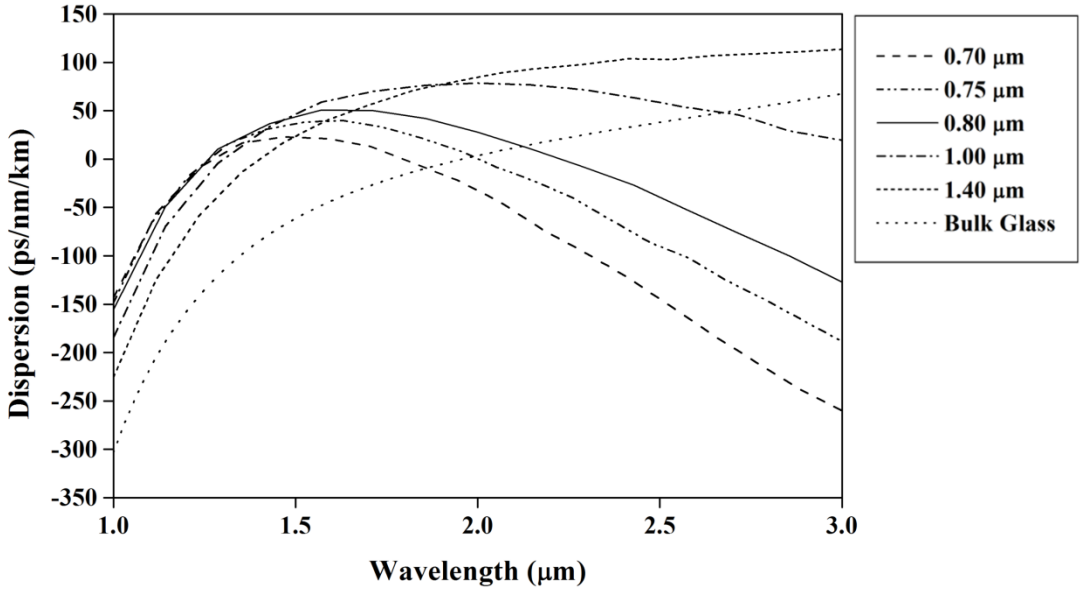

Figure 2.9 Total dispersion profiles of SF57 fibers with various core radii.

2.4 Simulation Results and Discussions

We start with the evolution of pulses in uniform fibers, with small input soliton orders. In the following, two different cases are taken as examples: core radius r=1.2 μm and r=0.75 μm. The relevant parameters in simulations are computed and given in Table 2.1. To analyze the generation of new frequency components, it is useful to introduce the frequency-resolved optical gating (FROG) technique by calculating the spectrogram, a function displaying the field in time and frequency domains simultaneously. With the field E(t) to be analyzed, the spectrogram is defined by[]:

$$S(\omega, \tau)=\left|\int_{-\infty}^{+\infty} E(t)g(t-\tau)e^{-i\omega t}dt\right|^2 \quad (2.4.1)$$

where g(t-τ) is a variable-delay gate function. In our simulation, the gate function is simply the femtosecond input pulse.

Figure 2.10 shows the temporal and spectral pulse evolution along the length in an SF57 fiber with core radius of 1.2 μm. The peak power and duration of the injected pulse are 1kW and 50 fs respectively, yielding a soliton order of 3.9. As shown in Figure 2.8 (a), the fiber exhibits a single ZDW at 1.35 μm, which is close to the pump wavelength (1.55 μm). As can be observed in the graph, a high-order soliton always experiences spectral broadening and temporal compression at the initial stage due to self-phase modulation and anomalous GVD. However, the high-order soliton is an unstable bound state of distinct fundamental solitons travelling at the same group velocity, and the perturbation of high-order dispersion and Raman nonlinearity leads to soliton fission at length ~L_D/N. The soliton components proceed with the SSFS effect, and part of their energy is shed via the generation of dispersive waves in the normal GVD region below 1.35 μm. Note that DW is generated when the solitons are spectrally overlapped with the DW wavelength

determined by phase-matching condition. According to the solution of equation (2.2.31), a soliton at 1.55 μm will emit a dispersive wave at 1.27 μm, which agrees well with the simulation result. It should also be noted that the solitons will slow down while moving towards longer wavelengths due to the reduction in the group velocity. This explains the parabola soliton trajectory in the (T,z)-plane in Figure 2.10. Figure 2.11 – Figure 2.15 illustrate the spectrograms along with the projected pulse profiles and spectra at various propagation distances, in which we can easily distinguish between red-shifted solitons (regularly shaped structures) and dispersive waves. The strong oscillation structure such as the one shown in Figure 2.15 (b) arises from the interaction between solitons and DWs when they are temporally overlapped.

Figure 2.16 shows the pulse propagation along the length of a uniform SF57 fiber with core radius of 0.75 μm, and Figure 2.17–Figure 2.21 illustrate the spectrograms, pulse profiles and spectra at some specific positions. The input soliton order is set to 3.7. Unlike the above case, the fiber has two ZDWs located at 1.25 μm and 2.11 μm. As a result, dispersive waves are also emitted across the second ZDW at the long wavelength side, as shown in Figure 2.16 and 2.19 (a). By solving the phase matching condition (2.2.31), the dispersive waves emitted by solitons at 1.55 μm turn out to appear at 1.0 μm and 3.1 μm, perfectly matching the simulation results. Interestingly, it is visualized that large detuning of the soliton with respect to the ZDW leads to a large gap between the phase-matched DW and the ZDW, as well as an exponential decay in the DW's intensity.

Core Radius	Parameters	Values
1.2 μm	Input Peak Power	1000 W
	Input FWHM	50 fs
	Disperson Length L_D	2.78 cm
	Nonlinear Length L_N	0.18 cm
	Soliton Order N	3.9
	Soliton Fission Length L_{fiss} (~L_D/N)	0.71 cm
0.75 μm	Input Peak Power	2000 W
	Input FWHM	50 fs
	Dispersion Length L_D	2.09 cm
	Nonlinear Length L_N	0.16 cm
	Soliton Order N	3.7
	Soliton Fission Length L_{fiss} (~L_D/N)	0.57 cm

Table 2.1 Values of parameters in simulations

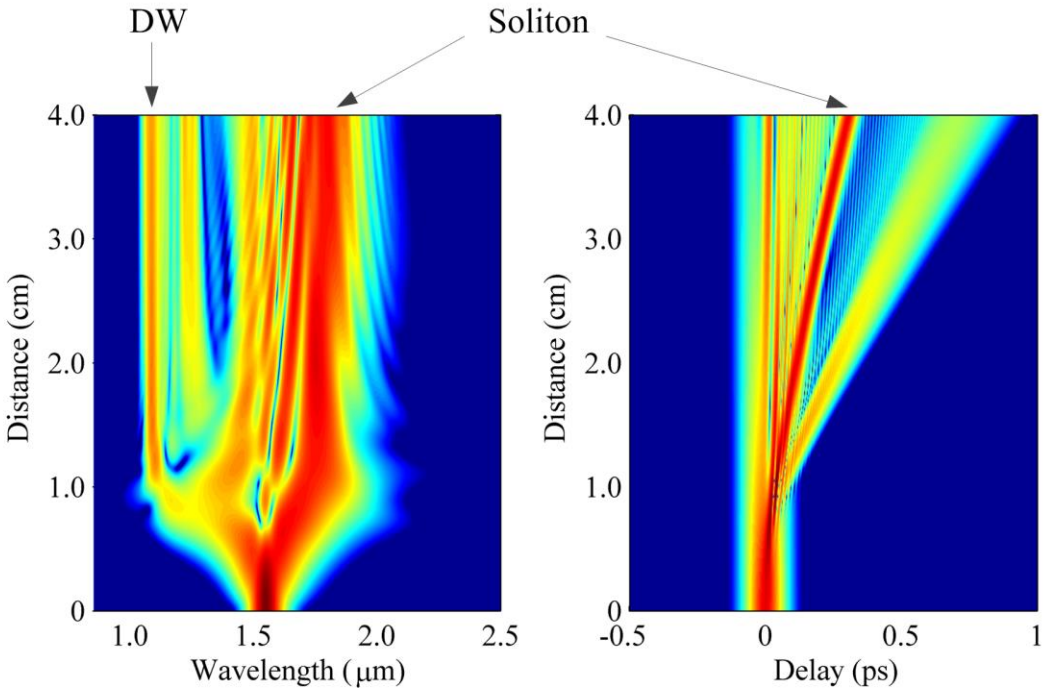

Figure 2.10 Temporal and spectral pulse evolution in SF57 fiber with radius of 1.2 μm.

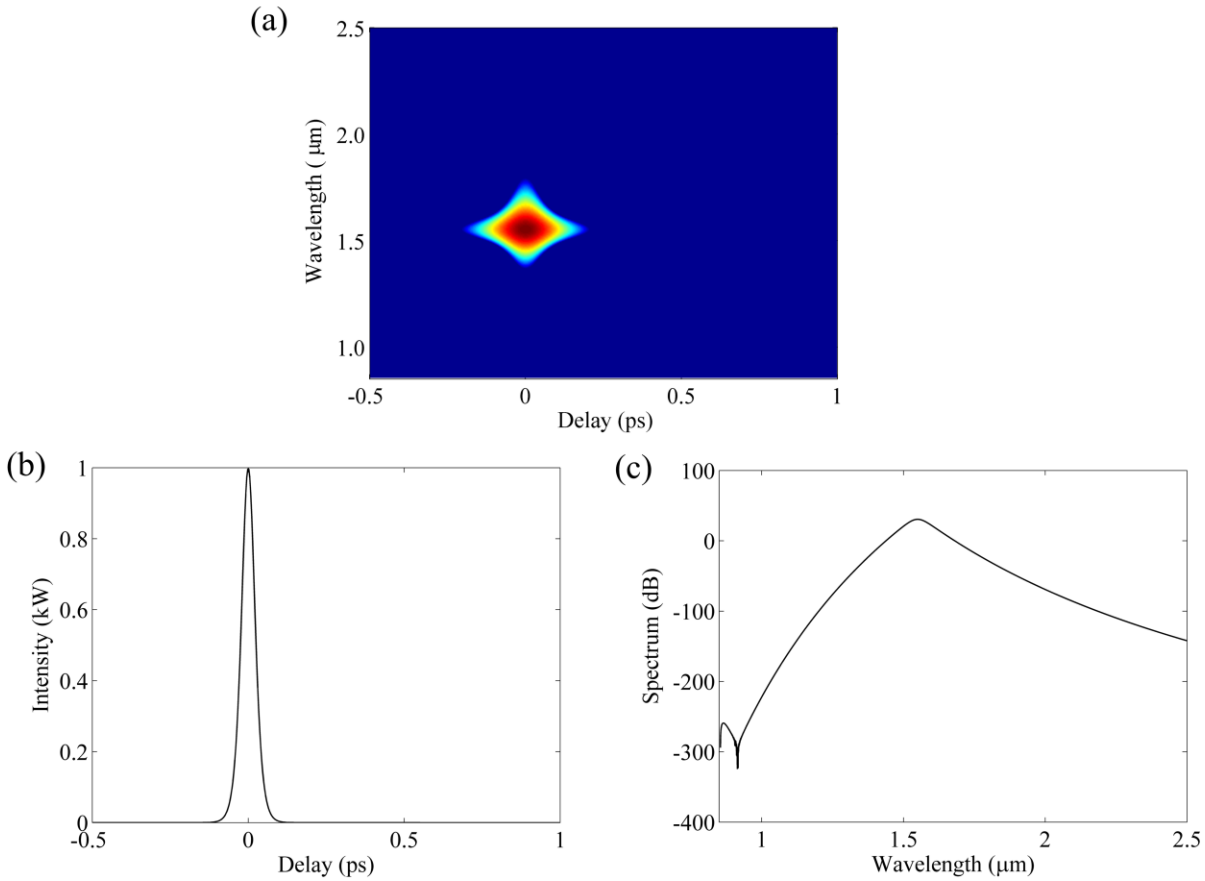

Figure 2.11 (a) Spectrogram, (b) pulse shape and (c) spectrum at propagation distance z=0 cm of SF57 fiber with radius r=1.2 μm.

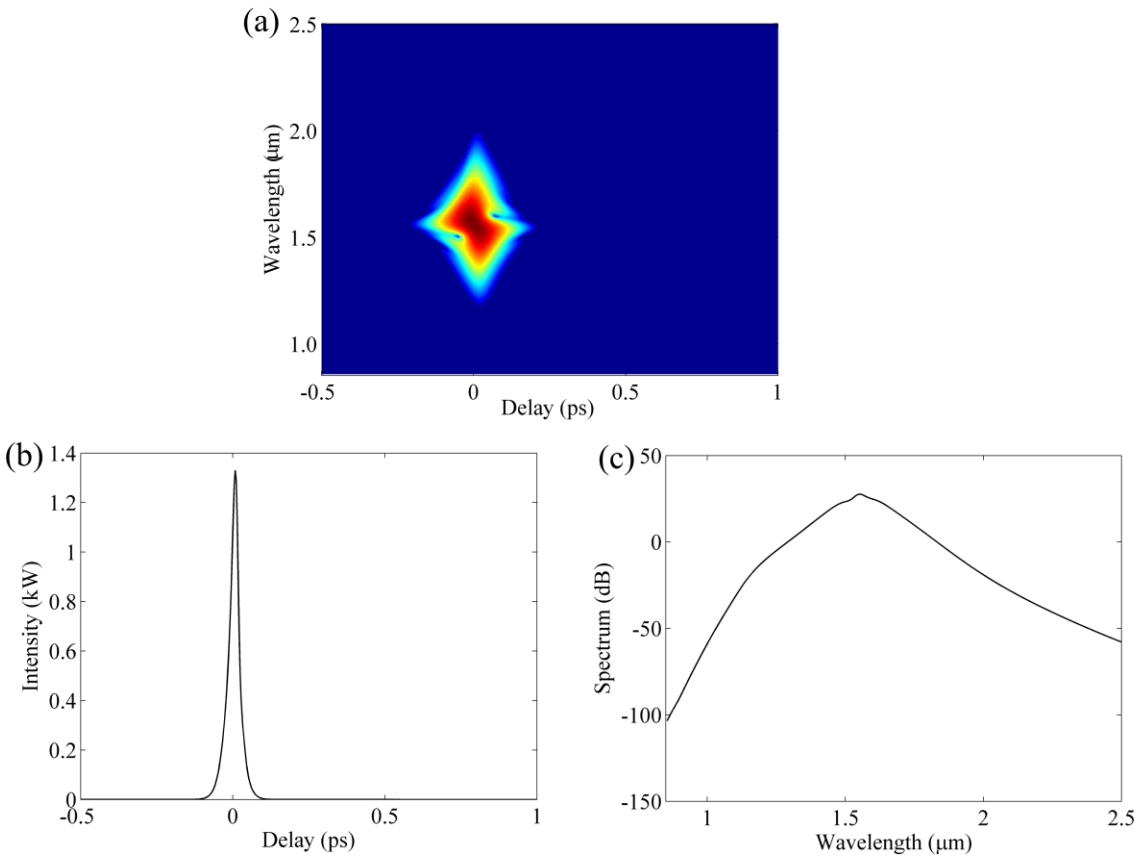

Figure 2.12 (a) Spectrogram, (b) pulse shape and (c) spectrum at propagation distance z=0.4 cm of SF57 fiber with radius r=1.2 μm.

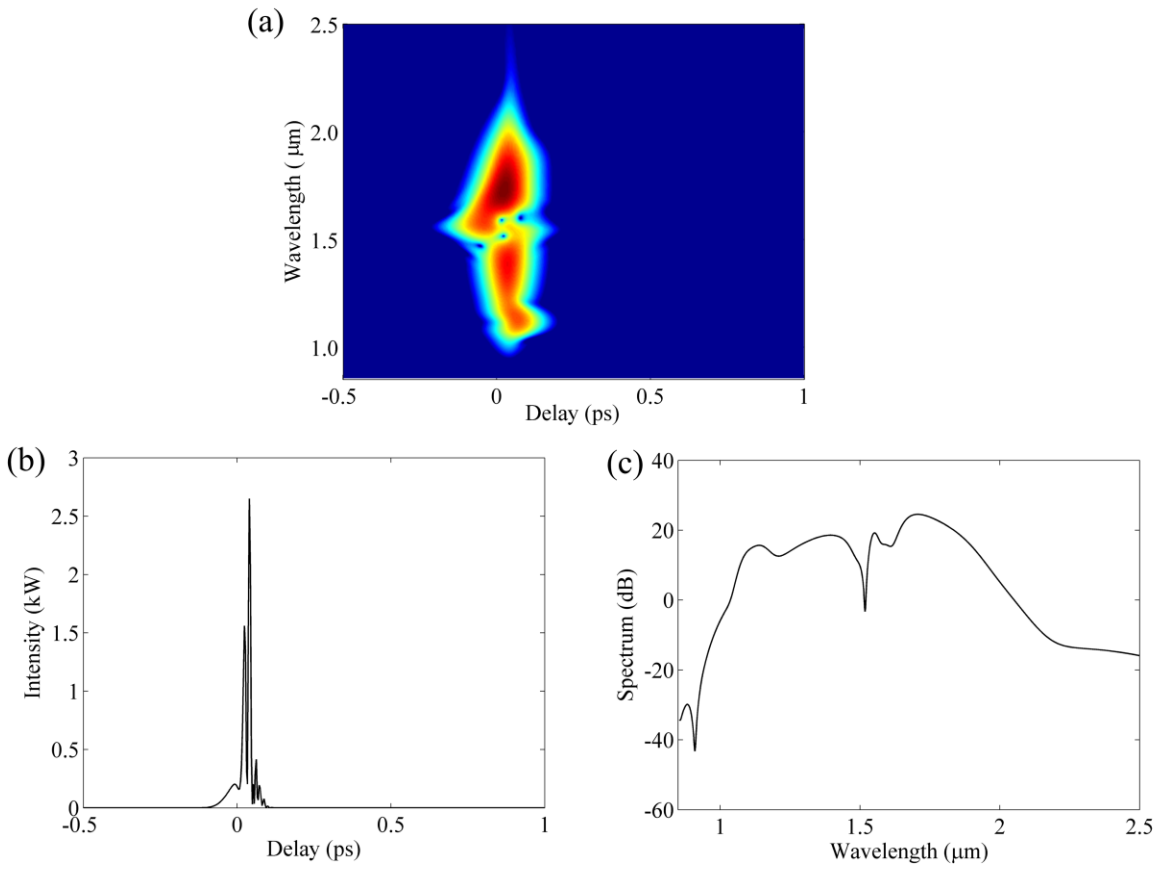

Figure 2.13 (a) Spectrogram, (b) pulse shape and (c) spectrum at propagation distance z=1 cm of SF57 fiber with radius r=1.2 μm.

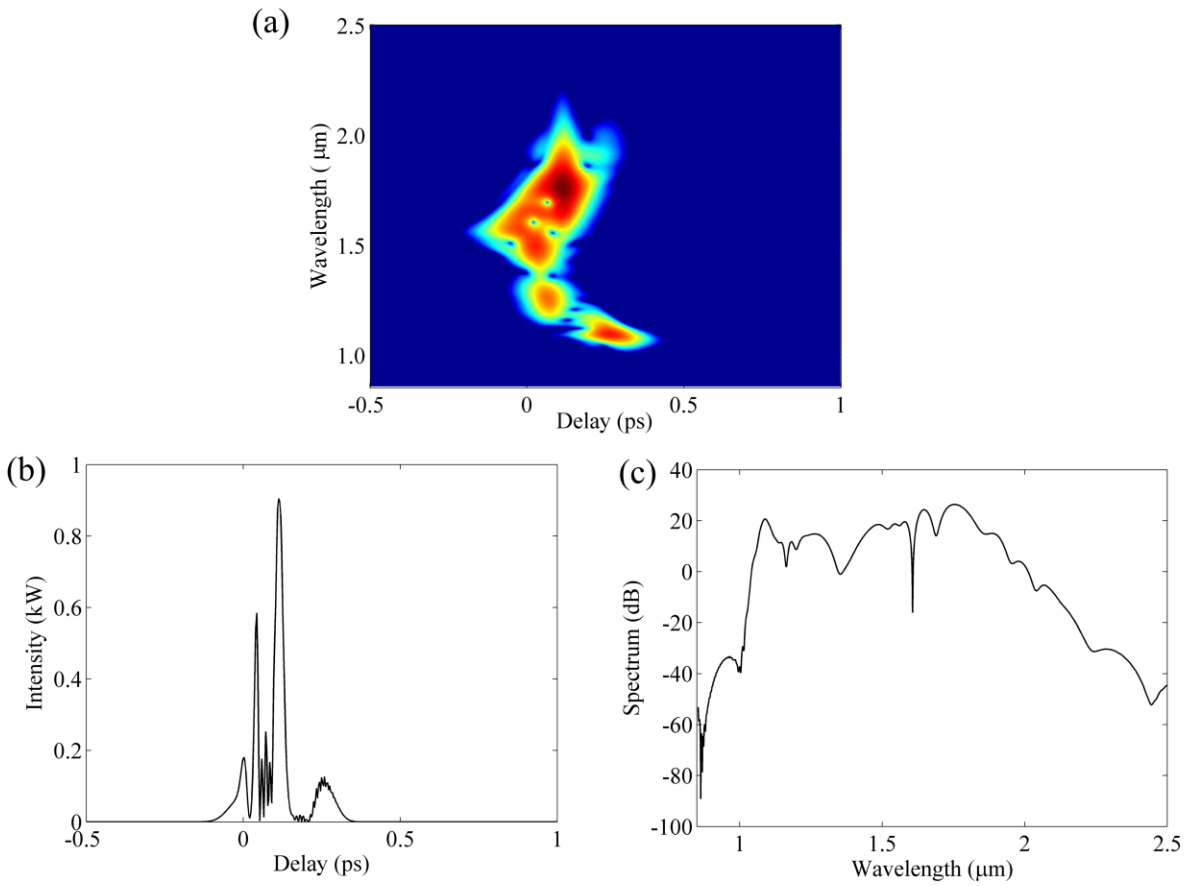

Figure 2.14 (a) Spectrogram, (b) pulse shape and (c) spectrum at propagation distance z=2 cm of SF57 fiber with radius r=1.2 μm.

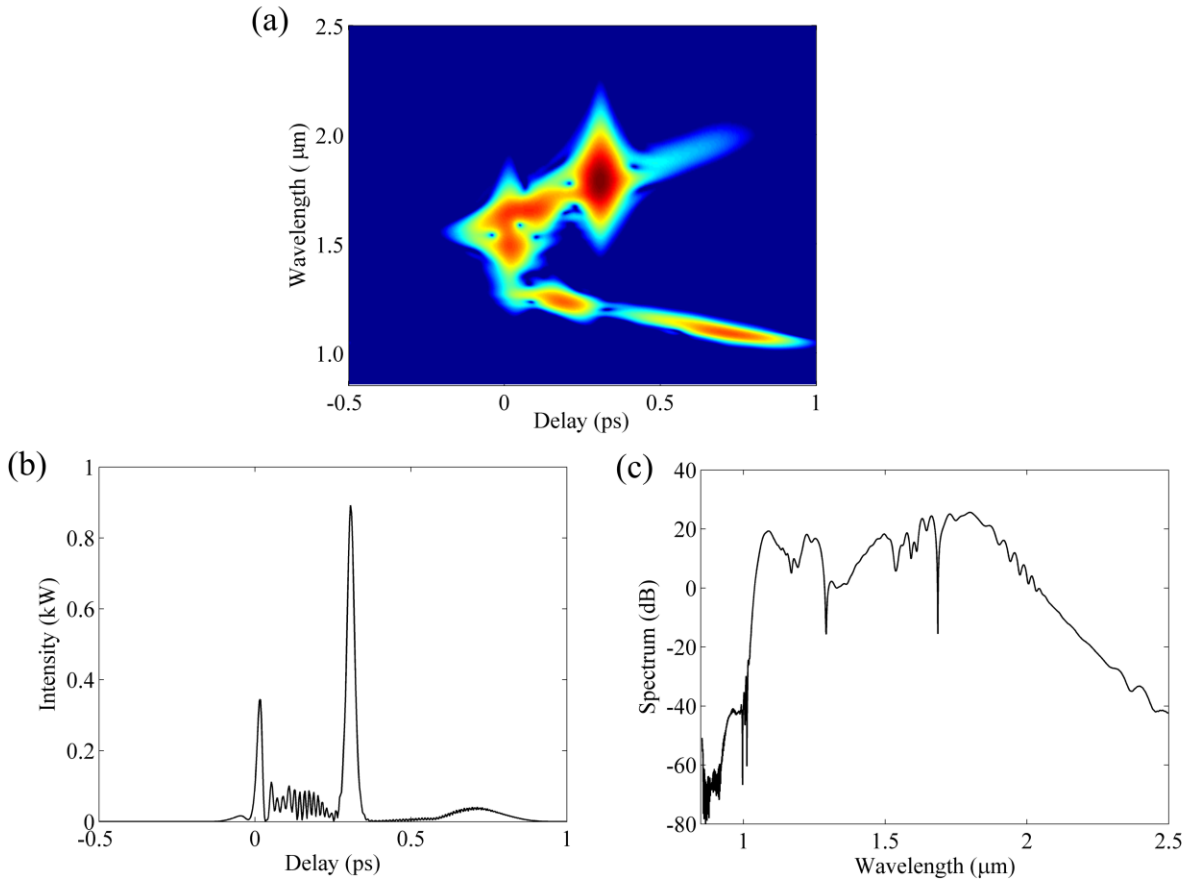

Figure 2.15 (a) Spectrogram, (b) pulse shape and (c) spectrum at propagation distance z=4 cm of SF57 fiber with radius r=1.2 μm.

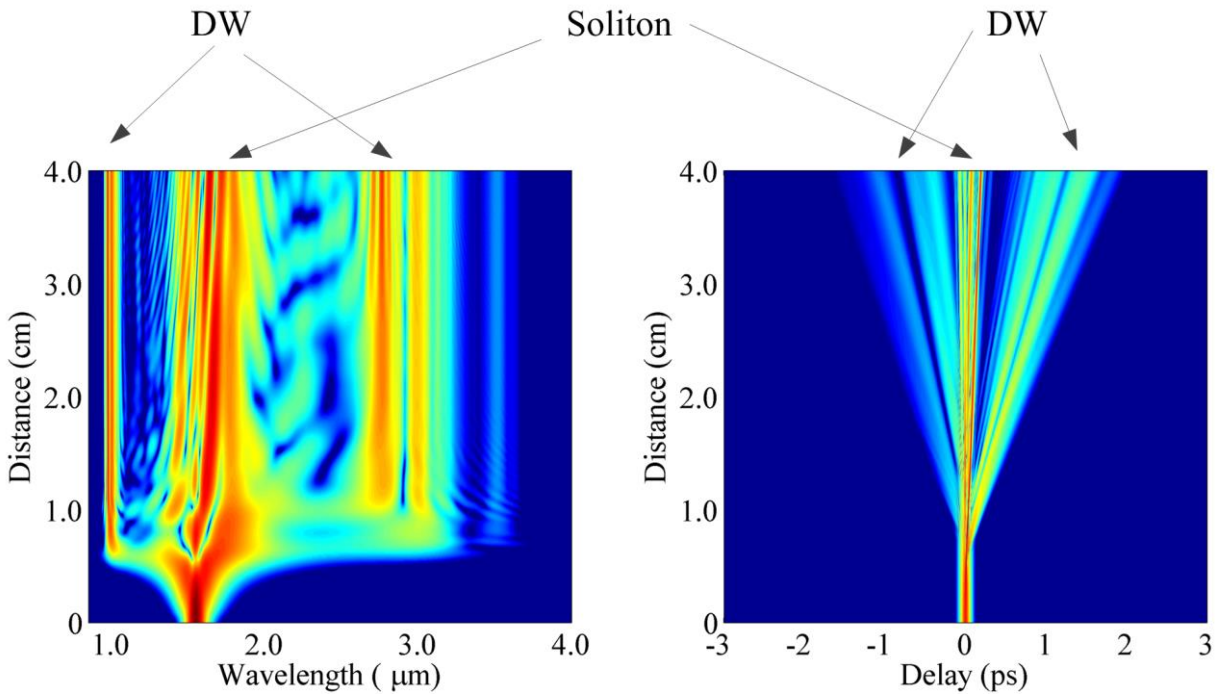

Figure 2.16 Temporal and spectral pulse evolution in SF57 fiber with radius of 0.75 μm.

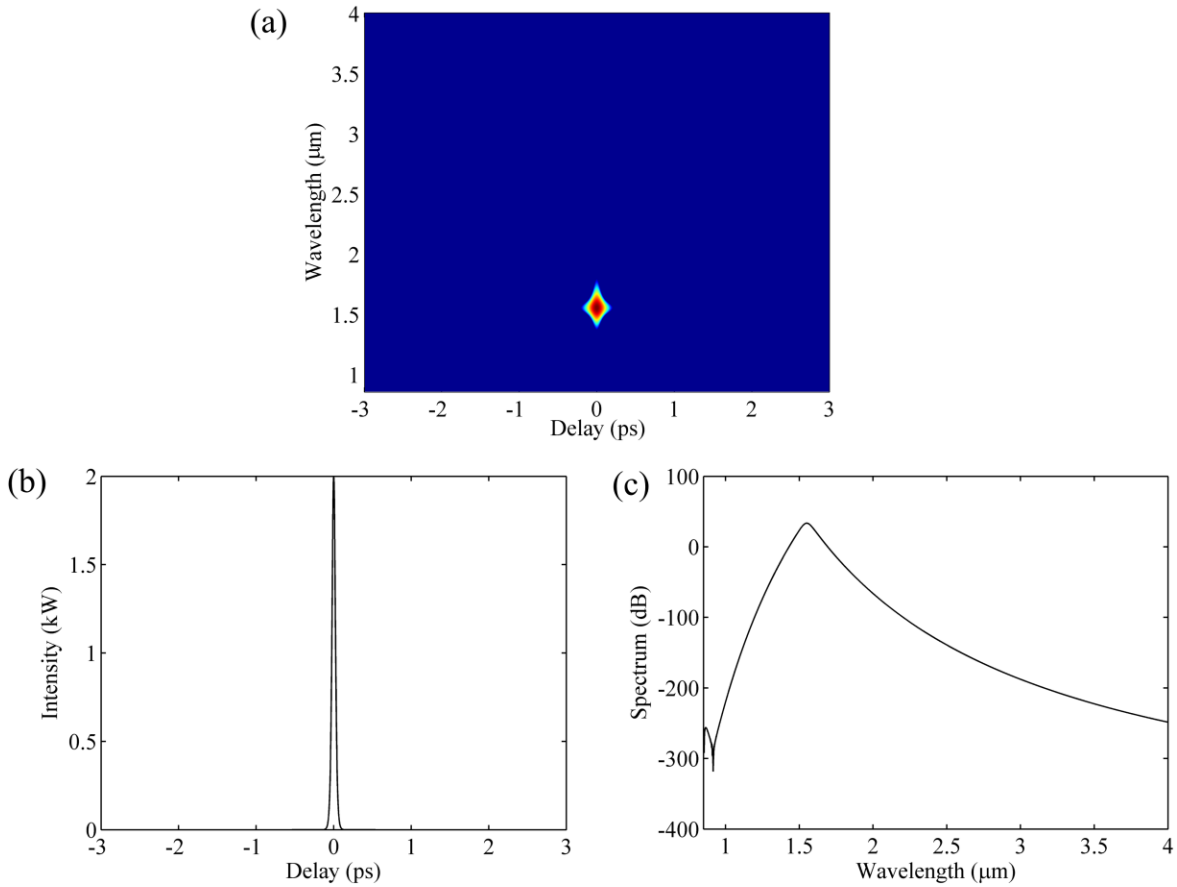

Figure 2.17 (a) Spectrogram, (b) pulse shape and (c) spectrum at propagation distance z=0 cm of SF57 fiber with radius r=0.75 μm.

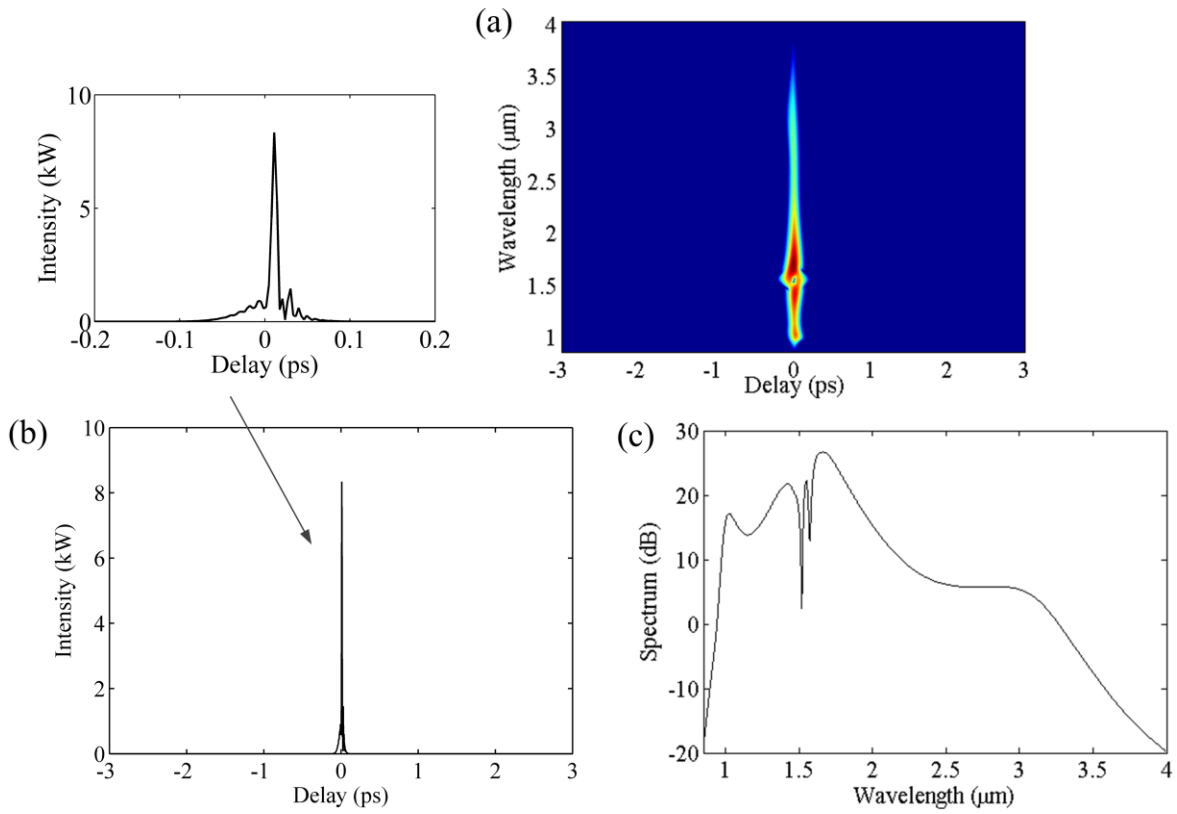

Figure 2.18 (a) Spectrogram, (b) pulse shape and (c) spectrum at propagation distance z=0.6 cm of SF57 fiber with radius r=0.75 μm.

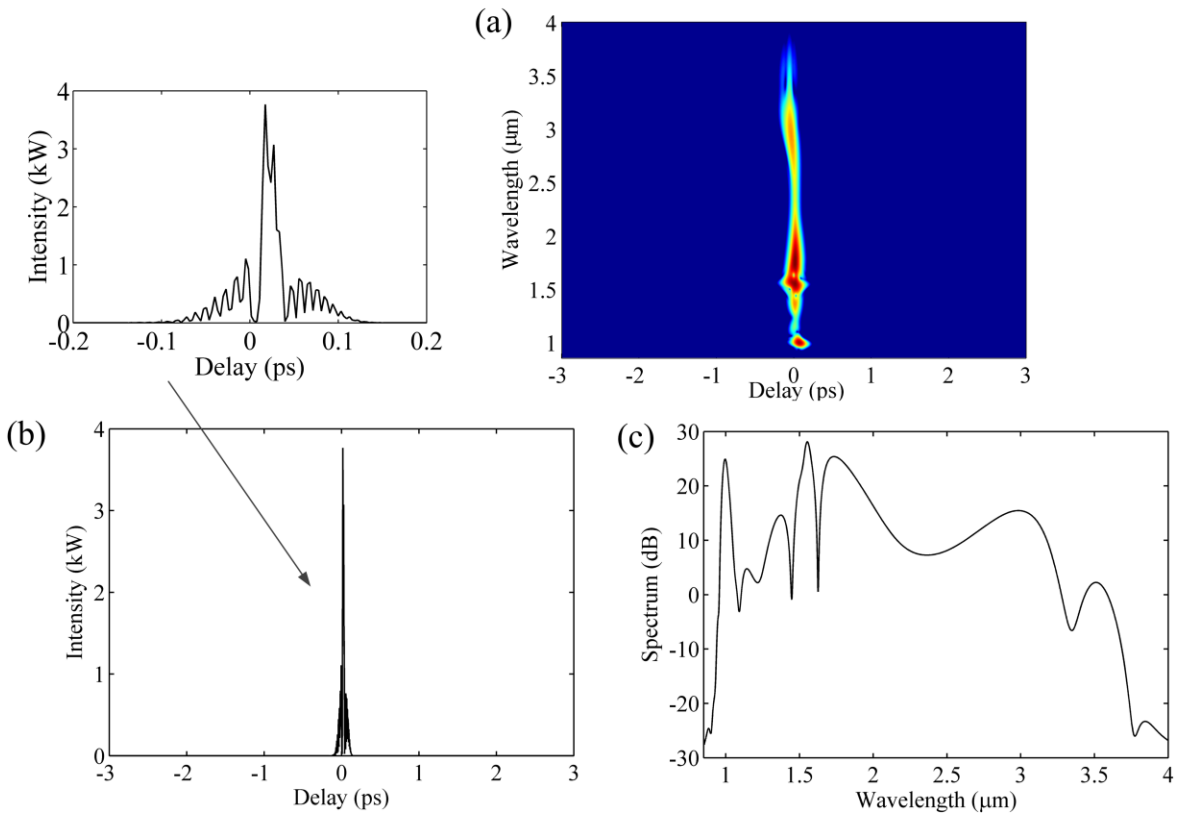

Figure 2.19 (a) Spectrogram, (b) pulse shape and (c) spectrum at propagation distance z=0.8 cm of SF57 fiber with radius r=0.75 μm.

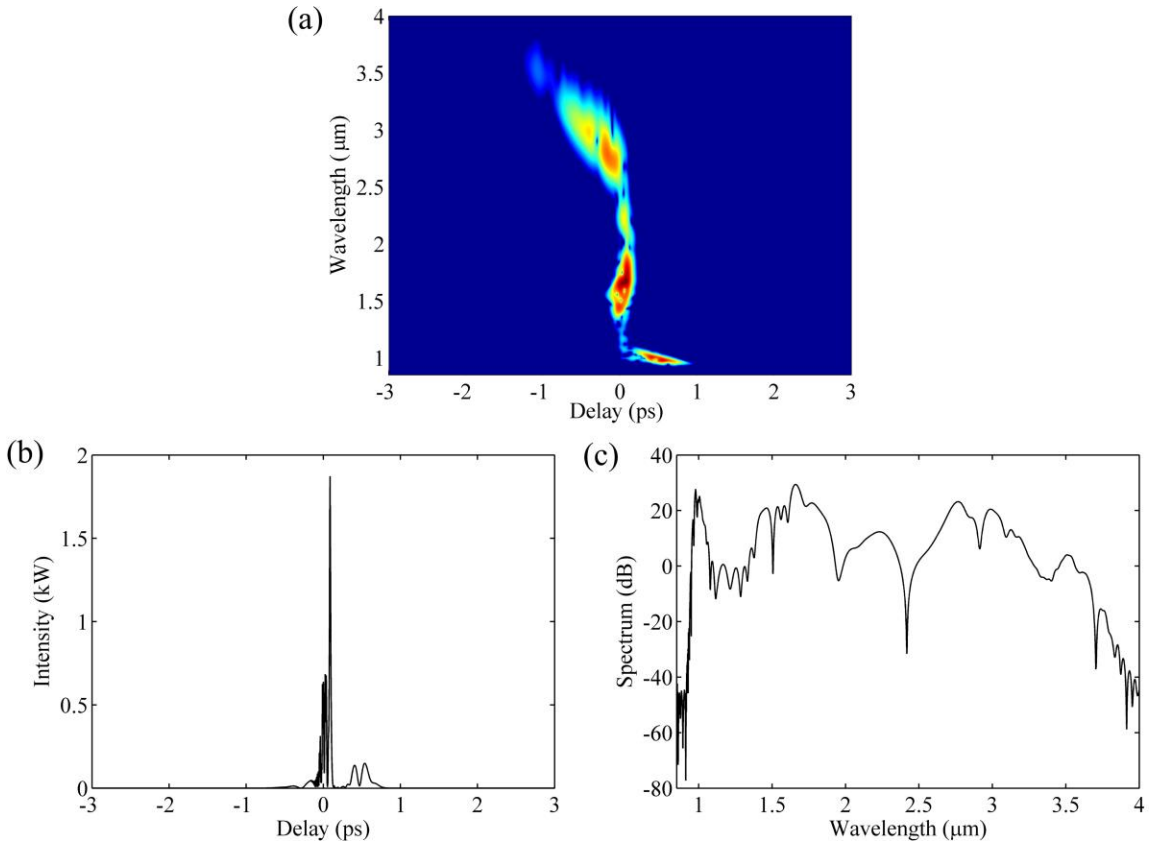

Figure 2.20 (a) Spectrogram, (b) pulse shape and (c) spectrum at propagation distance z=2 cm of SF57 fiber with radius r=0.75 μm.

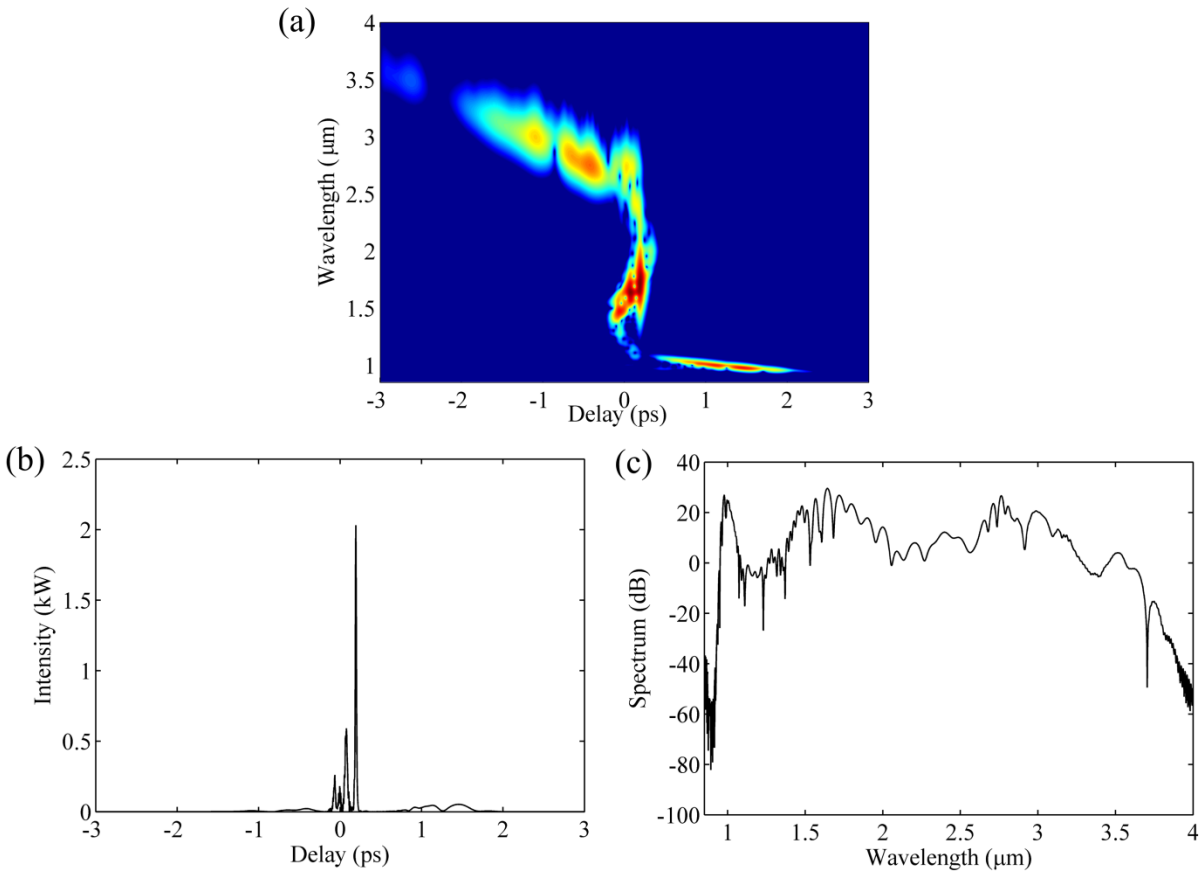

Figure 2.21 (a) Spectrogram, (b) pulse shape and (c) spectrum at propagation distance z=4 cm of SF57 fiber with radius r=0.75 μm.

As stated before, we have designed a 4-cm long tapered fiber structure shown in Figure 2.7 to generate broadband supercontinuum. Figure 2.22 and Figure 2.23 show the simulated SCG, with the spectrum extending to ~4.8 μm (within the transmission window of SF57 glass) at the output. The peak power and FWHM of the pump pulse are 6 kW and 100 fs, respectively. In this case, the second ZDW is red-shifted with the propagation length, leading to a continuous modification of the phase-matching condition for dispersive wave emission. Consequently, DWs are produced gradually towards longer wavelengths, which makes it possible to significantly broaden the output spectrum. In addition, the soliton self-frequency shift is also enhanced since the spectral recoil effect that cancels SSFS is decreased. It can be seen that the spectrum is less dense beyond 2 μm, because energy is transferred from solitons to dispersive waves, spreading out over a large spectrum region to form a broad and relatively uniform supercontinuum. The increased soliton order in conjunction with the interaction between solitons and DWs through XPM and FWM contributes to the flatness of the spectrum as well.

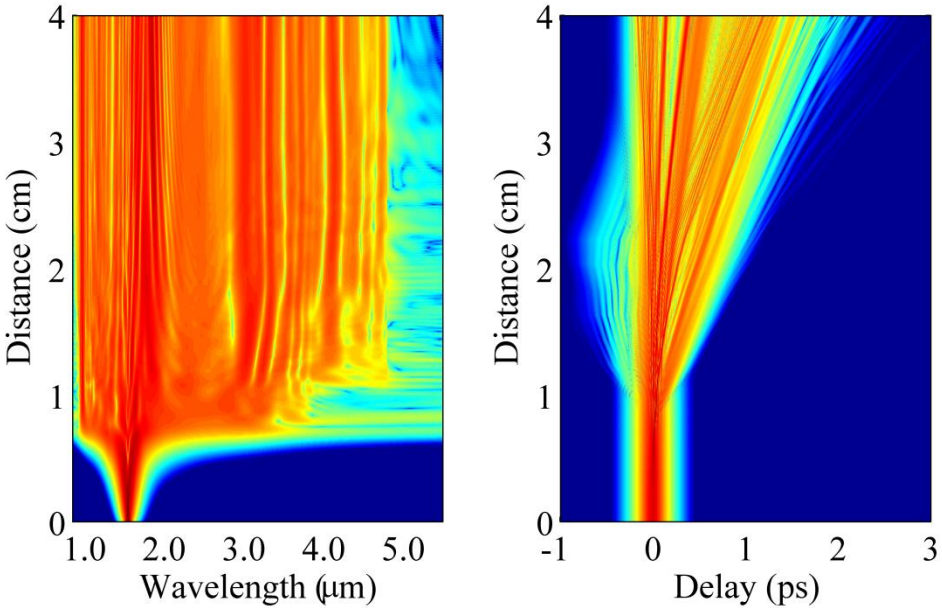

Figure 2.22 Pulse evolution and generation of supercontinuum in the proposed microstructured fiber taper. The peak power and FWHM of the pump source are 6 kW and 100 fs.

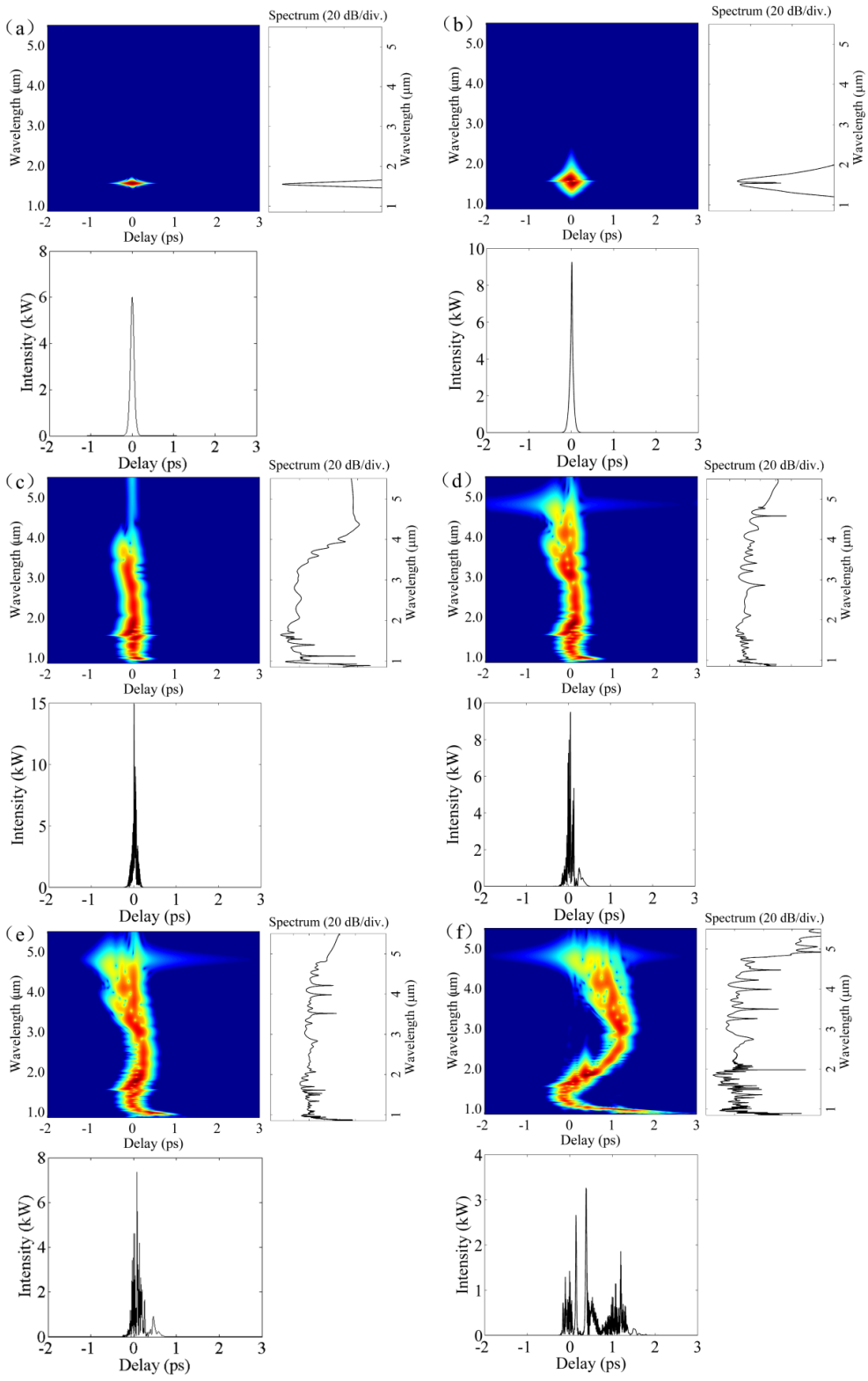

Figure 2.23 Spectrograms projected onto temporal intensity (bottom) and spectrum (right) at different propagation distances of (a) 0 cm, (b) 0.5 cm, (c) 1.0 cm, (d) 1.5 cm, (e) 2.0 cm, and (f) 4.0 cm.

2.5 Conclusion

In this chapter I have analyzed optical pulse evolution and supercontinuum generation in a lead silicate microstructured fiber taper. The fiber is 4-cm long, with the core size increasing gradually along the length. The mechanism of SCG is a combination of linear and nonlinear effects including loss, dispersion, self-phase modulation, cross-phase modulation, soliton dynamics, dispersive wave emission, stimulated Raman scattering and four-wave mixing. The fiber is pumped by a pulse with center wavelength of 1.55 μm, peak power of 6 kW and FWHM of 100 fs. Simulation is conducted by numerically solving the generalized nonlinear Schrödinger equation, which demonstrates that the broadband output extending to 4.8 μm is caused by the continuous modification of the phase matching condition and the emission of dispersive waves towards longer wavelengths.

Chapter 3 On-Chip Broadband Supercontinuum Generation

3.1 Introduction

As stated in the last chapter, supercontinuum generation (SCG) is the broadening of spectrum due to various linear and nonlinear optical processes including self-phase modulation (SPM), cross-phase modulation (XPM), stimulated Raman scattering (SRS), four-wave mixing (FWM), soliton fission and dispersive wave (DW) radiation. So far, many theoretical and experimental investigations have been conducted for fiber-based supercontinuum (SC) [1-6]. Specifically, the advent of microstructured fibers and photonic crystal fibers (PCFs) has led to significant progress in ultra-broadband SCG [7-9]. Moreover, a variety of glass with high nonlinearity, such as lead silicate [10-12], fluoride [13] and chalcogenide [14-18], has been introduced as the core material. In [10], Leong et al. designed and fabricated PCFs for SCG using lead silicate SF57 glass and obtained the highest nonlinear parameter ever reported (1860 $W^{-1}km^{-1}$ at 1550 nm).

The guidance properties of microstructured fibers have made it possible to engineer the dispersion characteristic, which plays a crucial role in efficient supercontinuum generation. By changing the dimension of the solid core and the air holes, the zero-dispersion position (ZDP) is modified, and multiple ZDPs can be formed. In particular, PCFs with two zero dispersion wavelengths (ZDWs) have been demonstrated to enhance SCG [19, 20]. Moreover, non-uniformly tapered fibers have been designed to further increase the spectral bandwidth, which is caused by the continuous shift of the dispersion profile along the propagation distance [11, 13]. We have given one example in Chapter 2.

Compared with fibers, rectangular waveguides are more applied in integrated optical devices

with low cost. For this reason, supercontinuum generation in planar waveguides has gained much interest recently [21-23]. Note that by proper design of the waveguide geometry, it is possible to fabricate planar waveguides with more than one ZDW, similar to PCFs. However, the modification of the dispersion profile is quantitatively less significant than in PCFs [21]. Then the question arises whether we can apply the dispersion-managing technique in rectangular waveguides to enhance spectral broadening.

In this chapter, I report a new design of a 2-cm-long tapered rib waveguide to manage the dispersion property for SCG. The Air-SF57-SiO_2 rib waveguide continuously increases the etch depth along the propagation distance, which shifts the second ZDW towards longer wavelengths. Hyperbolic secant input pulses at 1550 nm are launched into this waveguide, and numerical simulations demonstrate that the output continuum extends from ~1000 nm to ~4600 nm at -30 dB level, which covers nearly the whole transmission window of SF57. The results show the potential for on-chip supercontinuum generation in integrated optical systems.

3.2 Waveguide Design and Theoretical Model

We design an Air-SF57 glass-SiO_2 rib waveguide for supercontinuum generation as illustrated in Figure 3.1, with adjustable parameters including the rib width W, outer slab thickness d and etch depth h. Scott SF57 is a commercially available lead-silicate glass mainly composed of SiO_2 and PbO, with a Pb cationic content of 40-50% [24]. The linear refractive index of SF57 at 1550 nm is n = 1.8 [25], which results in an index contrast of 17.6% to the SiO_2 substrate, allowing for tight modal confinement. The nonlinear refractive index of SF57 measured at 1.06 μm is $n_2 = 4.1\times10^{-19}$ m^2/W, much higher than that of pure silica glass [26]. In our simulation, it is assumed

that n_2 remains constant over the considered wavelength range, although obtaining accurate n_2 values relies on experimental measurements. The material loss of SF57 glass is 1.6 dB/m at 1550 nm [27]. Since the OH impurities in oxide glasses can lead to high absorption in the mid-infrared region, we suggest dehydration techniques should be applied during the fabrication process to greatly reduce the loss (< 50 dB/m) [28]. The transmission window of SF57 glass is limited by the multiphonon absorption edge, which is shown in Figure 3.2 [29]. It can be seen that SF57 is not transparent beyond the wavelength of 5 μm because of the strong Si-O bonding. Due to the short propagation distance of our designed waveguide (2 cm), the absorptive property of SF57 glass within the transmission window has a minor impact on the generated SC spectrum.

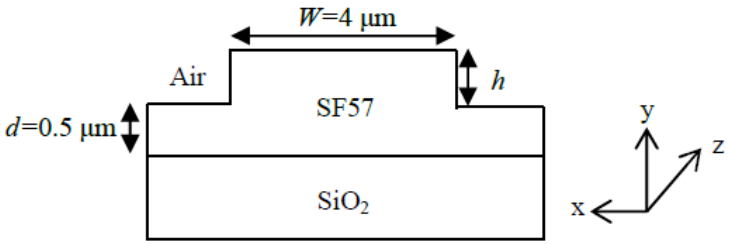

Figure 3.1 Cross section of the Air-SF57-SiO_2 planar rib waveguide with the rib width W, outer slab thickness d and etch depth h, respectively.

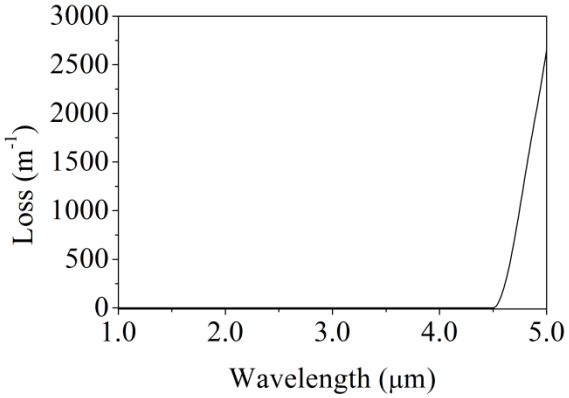

Figure 3.2 Multiphonon absorption edge of SF57 glass.

The dispersion characteristic has been demonstrated to be crucial for SCG. The wavelength-dependent dispersion profile of the rib waveguide for various h values is shown in Figure 3.3. W and d are set to be 4 μm and 0.5 μm, respectively. The calculation is done by a full-vector finite difference mode solver for the fundamental TM mode [30]. It can be seen that the waveguide dispersion depends strongly on the geometrical design, which provides an efficient method to control the total chromatic dispersion. Note that for small h (< 0.83 μm), a second ZDW exists, and it shifts to shorter wavelengths while h is decreasing. For comparison, the material dispersion of SF57 bulk glass is also plotted, with a single ZDW at 1970 nm.

Based on the dispersion property, I design a tapered waveguide structure illustrated in Figure 3.4. The waveguide is 2 cm long, with W = 4 μm and d = 0.5 μm. The etch depth h continuously increases from 0.6 μm to 0.9 μm along the propagation distance z by the following relationship:

$$h = h_0[1+(\frac{z}{z_0})^{\frac{1}{3}}] \tag{3.2.1}$$

where h_0 = 0.6 μm and z_0 = 16 cm. Note that planar waveguides with a tapered height have been fabricated for different applications [31-33].

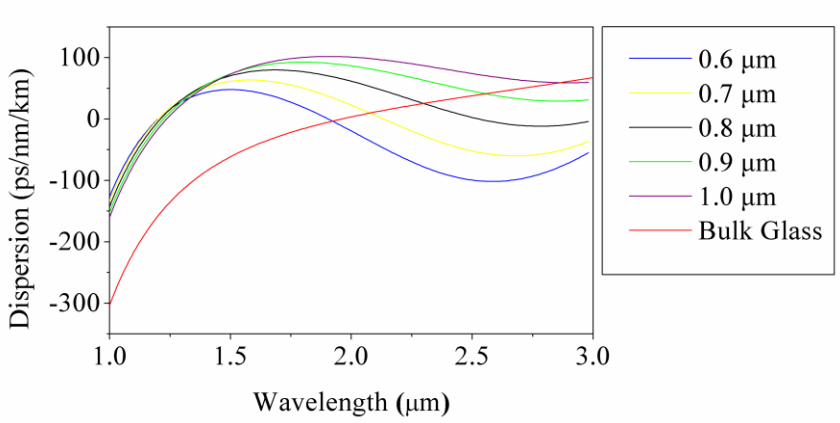

Figure 3.3 Dispersion profile of SF57 rib waveguide with varying etch depths h. The rib width W and outer slab thickness d are 4 μm and 0.5 μm, respectively.

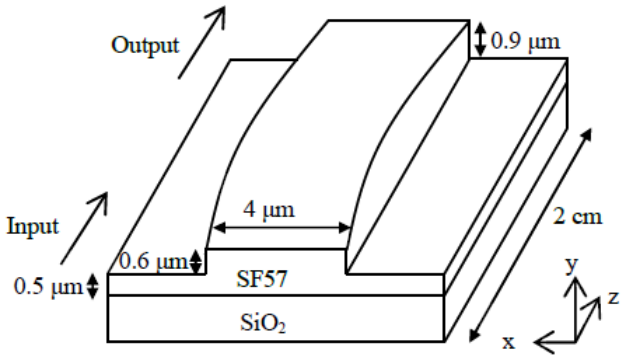

Figure 3.4 Schematic of the tapered SF57 rib waveguide.

Consider hyperbolic secant input pulses centered at 1550 nm. The optical field of the input pulse takes the form $P^{1/2}\mathrm{sech}(T/T_0)$, where P = 5 kW denotes the peak power and the full width at half maximum (FWHM) is $1.763T_0$ = 100 fs. The pulse evolution in the tapered rib waveguide is numerically simulated by the generalized nonlinear Schrödinger equation (GNLSE):

$$\frac{\partial A}{\partial z}+\frac{\alpha}{2}A+\sum_{k>=2}\frac{i^{k-1}}{k!}\beta_k\frac{\partial^k A}{\partial T^k}=i\gamma\left(1+\frac{i}{\omega_0}\frac{\partial}{\partial T}\right)\left(A\int_{-\infty}^{+\infty}R(T')\left|A(z,T-T')\right|^2dT'\right) \tag{3.2.2}$$

here, $A(z,t)$ is the pulse envelope evolving slowly along the planar waveguide, for which a retarded frame of reference moving at the group velocity v_g of the input pulse is introduced such that T = t - z/v_g. α is the linear propagation loss and β_k denote the Taylor-series expansion coefficients of the propagation constant β(ω) around the center frequency ω_0. γ is the nonlinear parameter defined as $\gamma(\omega_0) = n_2(\omega_0)\omega_0/(cA_{eff})$, where n_2 is the nonlinear refractive index, c is the speed of light and $A_{eff} = (\iint|E|^2dxdy)^2/(\iint|E|^4dxdy)$ is the effective mode area, respectively. The nonlinear response function $R(T) = (1-f_R)\delta(T)+f_Rh_R(T)$ includes both the instantaneous electronic response indicated by the delta function, and the delayed Raman contribution represented by $h_R(T)$. For SF57 glass, f_R = 0.1 and the Raman response function can be expressed as [34]:

$$h_R(t)=\frac{\tau_1^2+\tau_2^2}{\tau_1\tau_2^2}\exp(-\frac{t}{\tau_2})\sin(\frac{t}{\tau_1}) \tag{3.2.3}$$

in which τ_1 = 5.5 fs and τ_2 = 32 fs. The left side of equation (3.2.2) models the linear propagation effects, while the right side models the nonlinear effects. The GNLSE is numerically solved by the split-step Fourier method (SSFM) [35].

3.3 Simulation Results

We first consider uniform waveguide structure with a constant height and a single ZDW. Figure 3.5 shows the output spectrum of the waveguide with h = 1 μm after 2-cm propagation. The

ZDW locates at 1230 nm, and the center wavelength of the incident light (1550 nm) is in the anomalous dispersion regime and close to the ZDW. This has been demonstrated to be the optimum condition for the input wavelength to generate supercontinuum efficiently by enabling soliton dynamics. It is shown that the output SC spans from 900 nm out to 2500 nm at -30 dB level. In this situation, the spectral components on the long-wavelength side are mainly formed by soliton-self-frequency shift (SSFS), while the emission of dispersive waves (DWs) is responsible for the short-wavelength components only.

Next consider uniform waveguides with a second ZDW. The seed wavelength lies between the first and second ZDWs in the anomalous dispersion regime. The pump parameters remain the same, i.e., P = 5 kW and FWHM = 100 fs. Figure 3.6 and Figure 3.7 illustrate the simulated output spectra when h is set at 0.65 μm and 0.7 μm, respectively. Note that for h = 0.65 μm, the first and second ZDWs are 1200 nm and 1980 nm; for h = 0.7 μm, the first and second ZDWs are 1200 nm and 2130 nm. Both results exhibit supercontinuum extending to over 3000 nm, wider than that in Figure 3.5. Here the SCG originates from a two-stage mechanism. Due to abnormal dispersion, high–order solitons are injected into the waveguide, with the order expressed by:

$$N = \sqrt{\frac{L_D}{L_{NL}}} = \sqrt{\frac{\gamma P T_0^2}{|\beta_2|}} \tag{3.2.4}$$

in which $L_D = T_0^2/|\beta_2|$ is the dispersion length and $L_{NL} = 1/\gamma P$ is the nonlinear length. N turns out to be 12 for h = 0.65 μm and 10 for h = 0.7 μm. The input pulses undergo soliton fission and the pulse envelope breaks up into fundamental solitons, which approach the 2nd ZDW due to the Raman shift effect. In the second stage, when the spectrum extends across the second ZDW, dispersive waves are emitted (peak at 3100 nm for h = 0.65 μm and 3500 nm for h = 0.7 μm) towards the normal dispersion regime if the phase matching condition is satisfied. During this

process, the solitons transfer the energy to the DWs, providing an effective way to generate broadband spectrum.

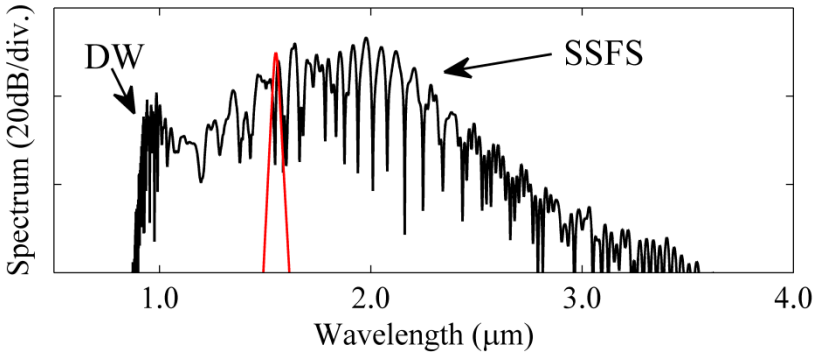

Figure 3.5 Output spectrum for SF57 rib waveguide with h = 1 μm. The red solid line near 1550 nm represents the input pulse spectrum.

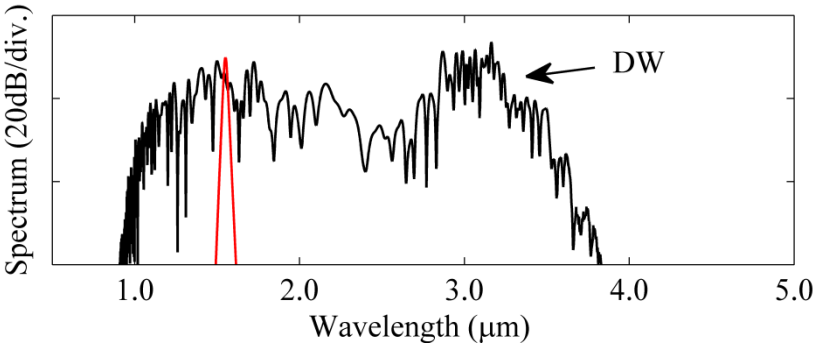

Figure 3.6 Output spectrum for uniform SF57 rib waveguides with h = 0.65 μm. The red solid line near 1550 nm represents the input pulse spectrum.

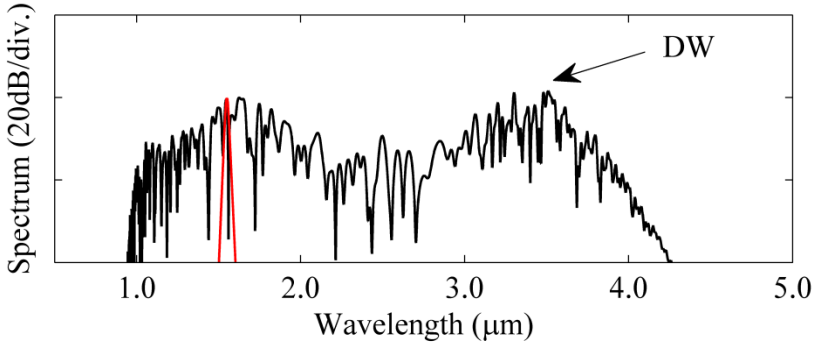

Figure 3.7 Output spectrum for uniform SF57 rib waveguides with h = 0.7 μm. The red solid line near 1550 nm represents the input pulse spectrum.

As stated before, I have studied SCG in a tapered SF57 rib waveguide with the structure specified by equation (3.2.1). Figure 3.8 shows the simulated spectrum evolution of the incident pulse (P = 5 kW, FWHM = 100 fs) traveling in the waveguide if optical loss is ignored in the simulation. The effective mode area A_{eff} at the input is equal to 3.2 μm^2, yielding a nonlinear parameter γ of 0.52/W/m at 1550 nm, roughly 500 times that of a conventional single-mode fiber. The generated spectrum has a 30 dB bandwidth from ~1000 nm to ~6000 nm. Since the continuum extends over the multiphonon absorption edge, the loss should be considered, which is shown in Figure 3.9. It can be seen that the output spectrum reaches ~4600 nm, still greater than that of uniform waveguides.

To understand the simulation results, note that the dimension of the waveguide at the input is carefully designed so that a second ZDW exists and the incident light is within anomalous dispersion regime. Therefore, the input pulses undergo soliton fission and DW emission across the upper ZDW, as described before. However, for the tapered waveguide with an increasing height, the 2nd ZDW is shifted along the propagation distance, leading to a continuous modification of the phase-matched wavelength for DW emission. This allows the DW to be produced towards longer wavelengths and thus significantly broadens the output supercontinuum. Clearly, different taper structures other than that described by equation (3.2.1) may be used, but the tapering rate should be optimized to ensure that the energy transfer from solitons to DWs is the most efficient. Figure 3.10 compares the output spectra for various tapering rates, with $h = h_0[1+ z/z_0)^k]$ in which $h_0 = 0.6$ μm and k is set to be 1 (linear form), 1/3 and 1/6, respectively. The parameter z_0 is adjusted so that h remains 0.9 μm at the exit. It can be seen that the waveguide taper described by equation (3.2.1) gives the broadest supercontinuum.

This is because if the ZDW varies too rapidly, there may be no spectral overlap of solitons and DWs, hence the solitons cannot transfer their power to the DWs across the ZDW, and the spectrum cannot spread out; on the other hand, if the ZDW shifts too slowly, the solitons may lose most of the energy before the DWs with longer wavelengths are emitted. Note that our result is comparable with that presented in [11], where a 4-cm SF57 fiber taper was proposed to produce supercontinuum reaching ~4.8 μm. We have predicted output spectrum with similar bandwidth from a shorter planar waveguide structure. In [21], a TAFD5 rib waveguide with two ZDWs was predicted to generate supercontinuum from 750 nm to 2400 nm due to non-solitonic radiation. However, the Raman response was negligible, which limited the soliton frequency shift and dispersive wave emission, thus the tapering technique may not be applicable for that waveguide. In [23], SC was produced by a dispersion engineered chalcogenide planar waveguide. The spectral broadening was mainly caused by four-wave mixing rather than soliton fission.

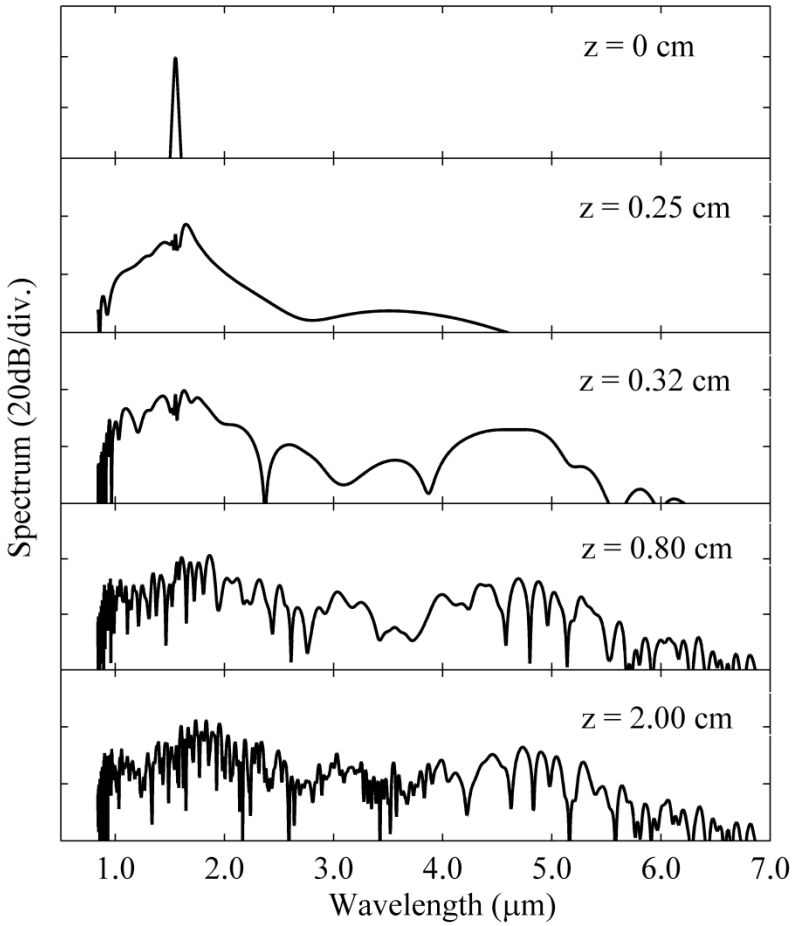

Figure 3.8 Spectrum evolution along the propagation distance for the proposed tapered SF57 rib waveguide if loss is ignored in the simulation.

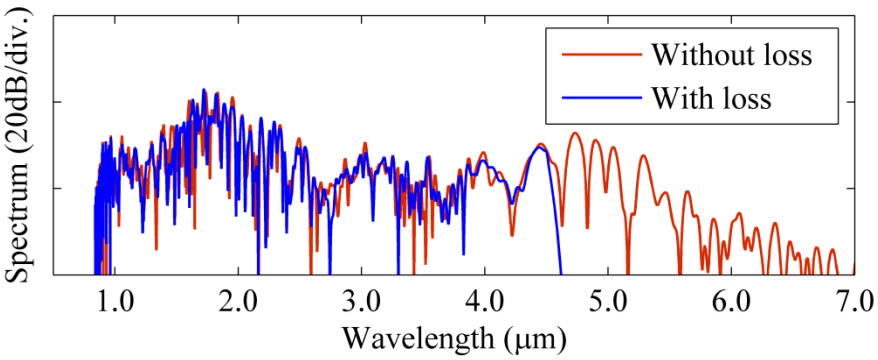

Figure 3.9 Effect of loss on the output continuum.

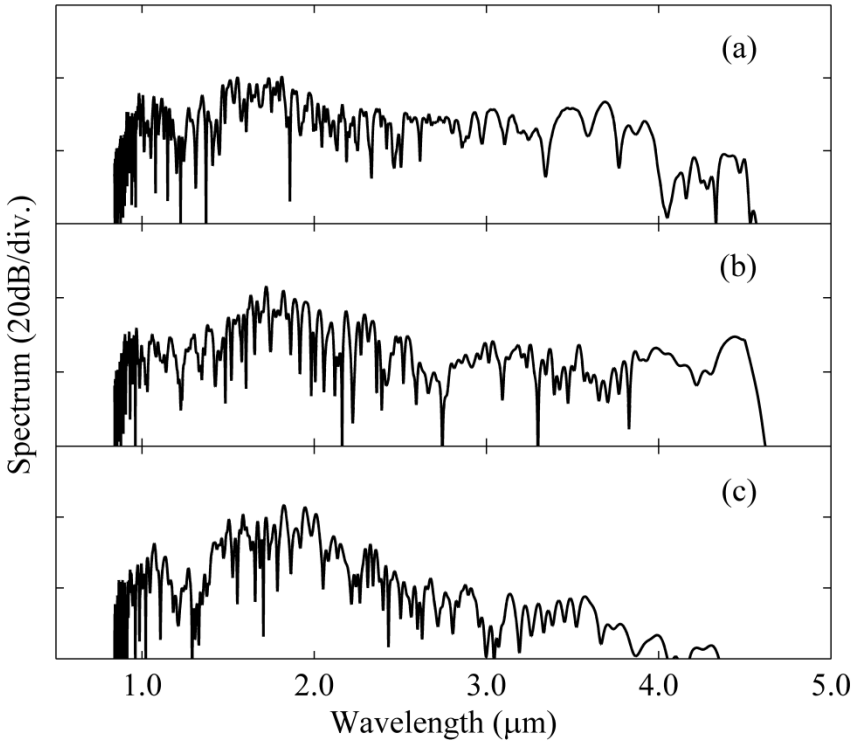

Figure 3.10 Output spectra for different tapering rates: $h = h_0[1+(z/z_0)^k]$, where (a) k = 1 (linear form), (b) k = 1/3, and (c) k = 1/6.

3.4 Conclusion

In this chapter, I have designed a tapered Air-SF57 glass-SiO_2 rib waveguide for supercontinuum generation. The 2-cm long waveguide has a gradually increasing etch depth along the propagation distance given by $h = h_0[1+(z/z_0)^{1/3}]$ (h_0 = 0.6 μm and z_0 = 16 cm), which shifts the second ZDW towards longer wavelengths. By launching into hyperbolic secant pulses with center wavelength of 1550 nm, peak power of 5 kW and full width at half maximum of 100 fs, the output spectrum is broad spanning from ~1000 nm to ~4600 nm at -30 dB. If the transmission window of the SF57 glass material is wider, even broader spectrum (~1000 nm to ~6000 nm) is expected. This waveguide design may be important for on-chip broadband SC sources.

Chapter 4 Coherence Properties of Supercontinuum Generated in Dispersion-Tailored Optical Waveguides

4.1 Introduction

As stated before, supercontinuum generation (SCG) is the broadening of optical pulse spectrum due to various linear and nonlinear optical phenomena. Besides the spectral bandwidth, the coherence property of supercontinuum is also an important feature, which indicates the instability of output due to input pulse noise [1]. From a practical point of view, the SC light source is required to be highly stable and insensitive to noise in some special scenarios. For example, coherent broadband light source is demanded in optical coherence tomography (OCT) technology to obtain high resolutions [2]. In DWDM optical communication systems, the stability of the spectrum is also a critical parameter because of the close spacing between adjacent channels. Therefore, different methods for characterizing the SC coherence properties have been developed [3, 4], and a lot of researches have been conducted both theoretically and experimentally to produce supercontinuum with excellent coherence [5-14]. In [3], a convenient way to quantify the degree of supercontinuum coherence was described, which was then used to theoretically study the SC spectra generated in optical fibers. The results showed strong dependence on the duration and center wavelength of the input pulse. Genty et al. [4] introduced a new approach which allowed for complete characterization of supercontinuum coherence. Their results demonstrated that supercontinuum light could be separated into quasi-coherent and quasi-stationary parts based on the pump pulse parameters. In [14], a ZBLAN non-uniform fiber taper was designed. It was numerically demonstrated to generate supercontinuum extending from ~1.5 μm to ~3 μm, with nearly perfect coherence degree over the entire spectral range.

In this Chapter, I numerically simulate the coherence properties of the supercontinuum generated in dispersion-tailored lead-silicate optical waveguides presented in Chapter 2 and Chapter 3. As stated before, the SF57 tapered fiber and tapered planar waveguide were geometrically designed to engineer the total chromatic dispersion, which was demonstrated to be an efficient method to extend the spectrum towards longer wavelengths (~5 μm). Investigation of the coherence property indicates that perfectly coherent spectrum can be obtained by properly adjusting the pump pulse parameters such as peak power and pulse width.

4.2 Theoretical Model

The inclusion of noise effect in the input pulse leads to both intensity and phase instability of the output continuum. Here we consider only the quantum-limited shot noise in the light source, and ignore the spontaneous Raman fluctuations along the waveguide length [1]. The phase stability property can be modeled quantitatively by calculating the modulus of the complex degree of first-order coherence function introduced by Dudley and Coen [3]:

$$|g_{12}(\lambda)| = \left| \frac{\left\langle E_1^*(\lambda) E_2(\lambda) \right\rangle}{\left[\left\langle |E_1(\lambda)|^2 \right\rangle \left\langle |E_2(\lambda)|^2 \right\rangle \right]^{1/2}} \right| \tag{4.2.1}$$

here E(λ) is the SC electric field and the angle brackets represent averaging over the independently generated SC pairs [$E_1(\lambda)$, $E_2(\lambda)$]. Experimentally, it can be measured by conducting a modified Young's two-source experiment. Mathematically, it has been proved that equation (4.2.1) can be approximated by [4]:

$$|g_{12}(\lambda)| = \frac{1}{N^2 - N} \frac{N^2 \left| \langle E(\lambda) \rangle \right|^2 - N \left\langle |E(\lambda)|^2 \right\rangle}{\left\langle |E(\lambda)|^2 \right\rangle} \tag{4.2.2}$$

in which N is the total number of SC realizations. It is also useful to define the overall degree of coherence across the entire spectrum as:

$$\left\langle \left| g_{12} \right| \right\rangle = \frac{\int \left| g_{12}(\lambda) \right| \left| E(\lambda) \right|^2 d\lambda}{\int \left| E(\lambda) \right|^2 d\lambda} \tag{4.2.3}$$

both $|g_{12}(\lambda)|$ and $<|g_{12}|>$ are bounded in the interval [0, 1], with 0 indicating incoherence and 1 indicating full coherence.

On the other hand, the intensity stability can be characterized using relative intensity noise (RIN), which is defined by the power noise normalized to the average power level. Nonetheless, it should be noted that RIN and $|g_{12}(\lambda)|$ are strongly correlated to each other, and the dependence of them on input pulse parameters is expected to follow similar trends. Therefore, we only calculate phase stability $|g_{12}(\lambda)|$ as a function of wavelength to analyze the supercontinuum coherence property.

The degree of coherence is computed by adding different quantum noise seeds in the input field, and numerically solving the GNLSE to produce independent SC realizations. The random noise in every temporal discrete bin of the input field is modeled as a stochastic variation with the standard deviation equal to the square root of the number of photons in that bin.

4.3 Simulation Results and Discussions

We have calculated the modulus of the degree of coherence function $|g_{12}(\lambda)|$ under different pump conditions by simulating an ensemble of 100 SC output spectra with random quantum noise. It turns out that the coherence degree is quite sensitive to the width and peak power of the

input pulse.

4.3.1 Coherence Properties of Supercontinuum Generated in Dispersion-Tailored Lead-Silicate Fiber Taper

A microstructured fiber taper has been designed in Chapter 2 to generate broadband supercontinuum extending to ~4.8 μm wavelength. In Figure 4.1 we plot the mean spectra and degree of coherence for various input pulse widths (FWHM), with the peak power fixed at 6 kW. It can be seen that although the spectra span from ~1 μm to ~5 μm in all the cases, the supercontinuum is more coherent for shorter input pulse duration. For example, with 200-fs-wide input pulses, $|g_{12}|$is close to one from ~2.5 μm to ~5 μm in the output SC spectrum, which drops nearly to zero across the same wavelength region for 350-fs pump pulse duration.

Figure 4.2 shows the dependence of the coherence degree on the pump peak power, with 200 fs FWHM. The results demonstrate that as the peak power increases, the spectral components of the generated SC become less coherent, while the spanning of spectrum is comparable. Specifically, for 5-kW pulses, $|g_{12}|$ is nearly 1 across the entire spectrum (1 μm~5 μm) and the supercontinuum is fully coherent. We also notice that due to fluctuation in the output spectrum, the spectral fine structure can be washed out and the mean spectrum appears artificially smooth when the coherence is low. This can be experimentally observed when using an optical spectrum analyzer with a long integration time.

Figure 4.3 shows the overall degree of coherence $\langle|g_{12}|\rangle$ calculated with diverse input pulse parameters, which confirms the relationship between the coherence property of the generated SC

and the pumping conditions. The results above imply that coherence can be improved by appropriately decreasing the peak power and width of the input pulses launched into the SF57 fiber taper. Note that the power level should still be high enough to invoke nonlinear optical effects.

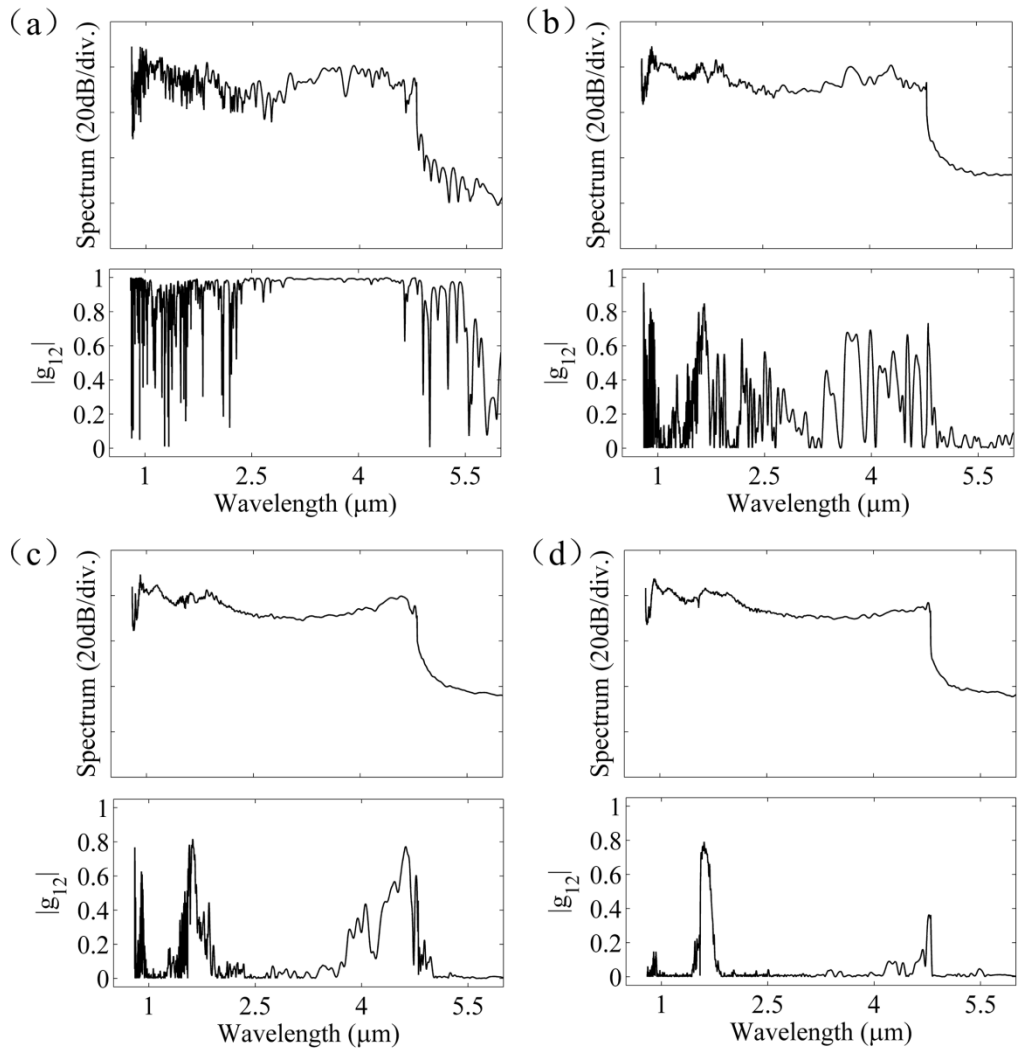

Figure 4.1 Mean spectra and coherence degree $|g_{12}(\lambda)|$ for input pulses with peak power of 6 kW and FWHM of (a) 200 fs, (b) 250 fs, (c) 300 fs, and (d) 350 fs.

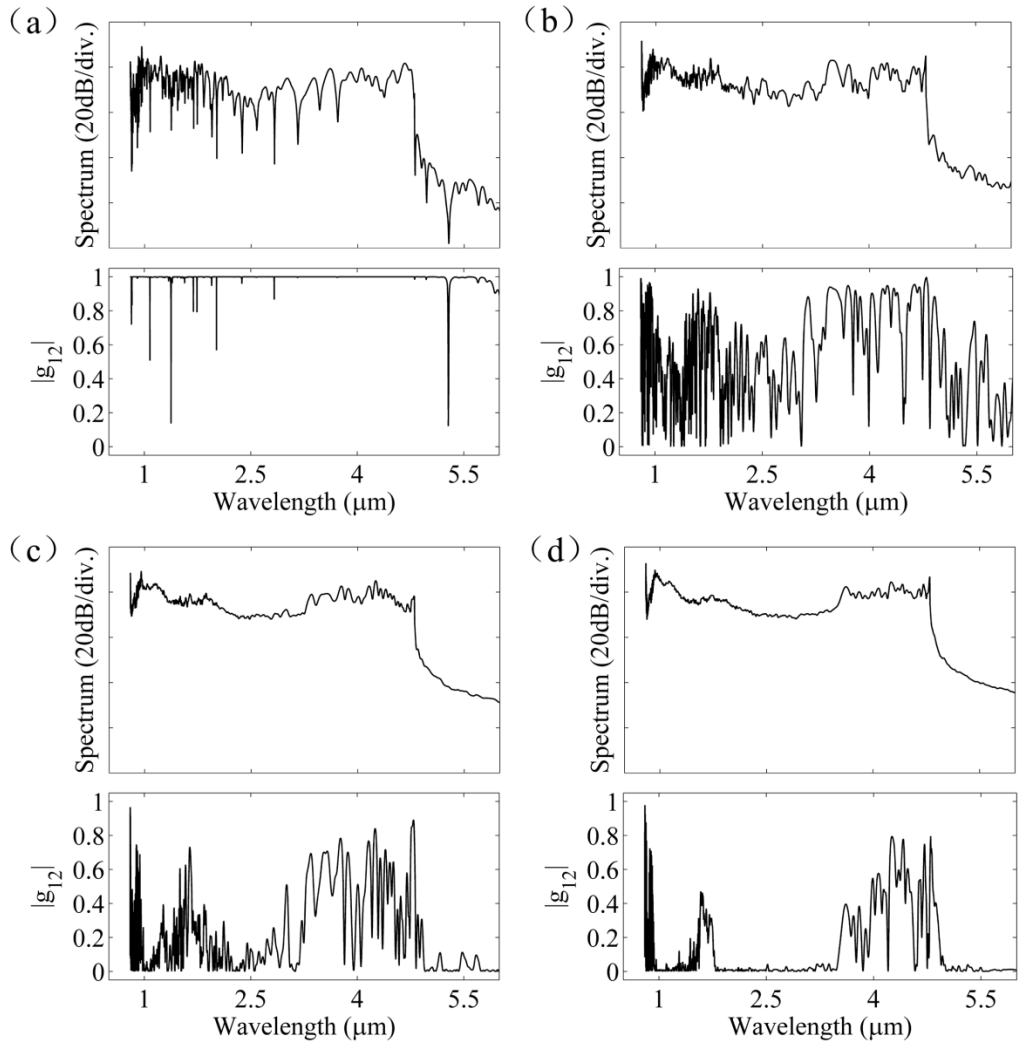

Figure 4.2 Mean spectra and coherence degree $|g_{12}(\lambda)|$ for input pulses with FWHM of 200 fs and peak power of (a) 5 kW, (b) 7 kW, (c) 9 kW, and (d) 13 kW.

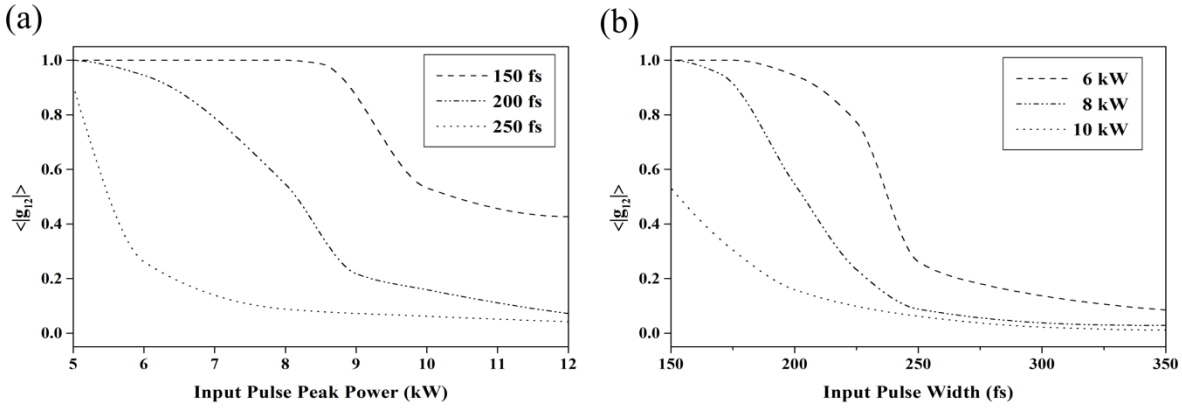

Figure 4.3 Overall coherence degree $<|g_{12}|>$ versus (a) input pulse peak power (with pulse width shown), and (b) input pulse width (with peak power shown).

4.3.2 Coherence Properties of Supercontinuum Generated in Dispersion-Engineered Tapered Planar Waveguide

Figure 4.4 plots the coherence degree of the output spectrum from the tapered planar waveguide designed in Chapter 3. The generated SC possesses excellent coherence with $|g_{12}(\lambda)|$ equal to 1 over the entire spectral range. We also study the coherence property for different pump pulse parameters as shown in Figure 4.5 and Figure 4.6. Although the SC spectra span from ~1 μm to ~ 4.6 μm in all cases, the degree of coherence is higher for shorter durations and lower power. The shot-to-shot variation in the temporal intensities is also shown in the graphs which will be used for further discussion below. In Figure 4.7, we depict the overall coherence degree $\langle|g_{12}|\rangle$ for different pumping conditions. Similar to those obtained from tapered fibers, the results confirm that it is possible to generate ultrawide and fully coherent supercontinuum from the tapered planar rib waveguide with appropriate choice of the pumping conditions.

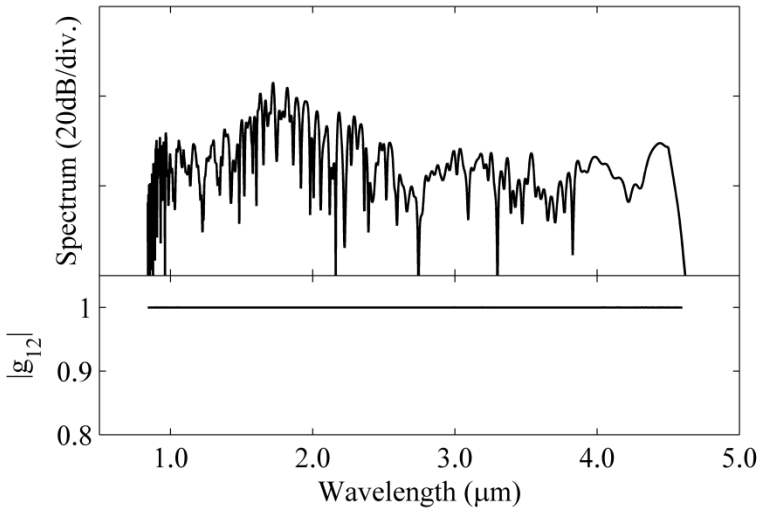

Figure 4.4 Coherence degree $|g_{12}(\lambda)|$ of the output spectrum generated from the designed tapered planar waveguide.

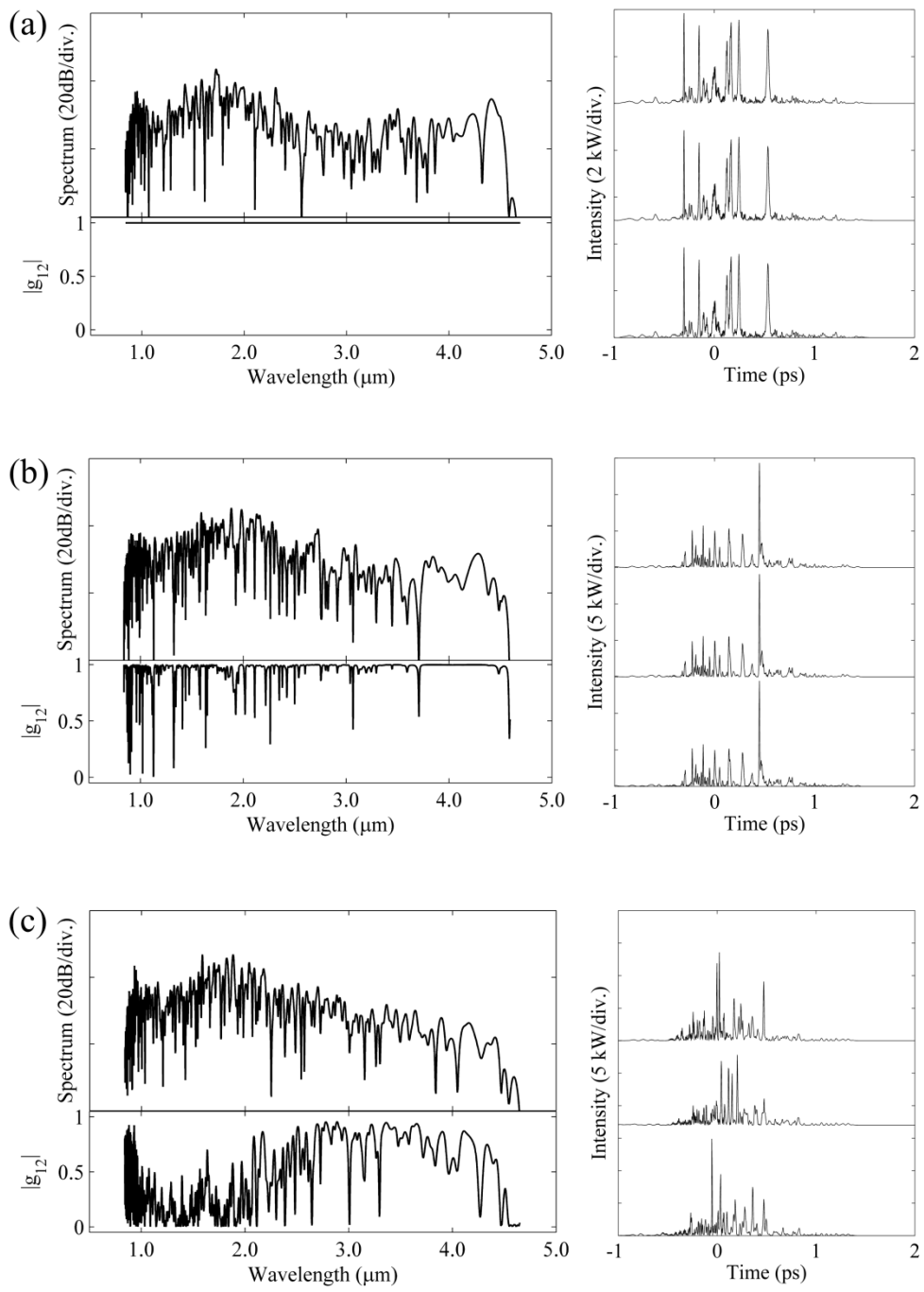

Figure 4.5. Spectra and coherence degree $|g_{12}(\lambda)|$ for input pulses with peak power of 7 kW and FWHM of (a) 100 fs, (b) 200 fs, and (c) 250 fs. The temporal intensities for three simulations with random noise are shown on the right.

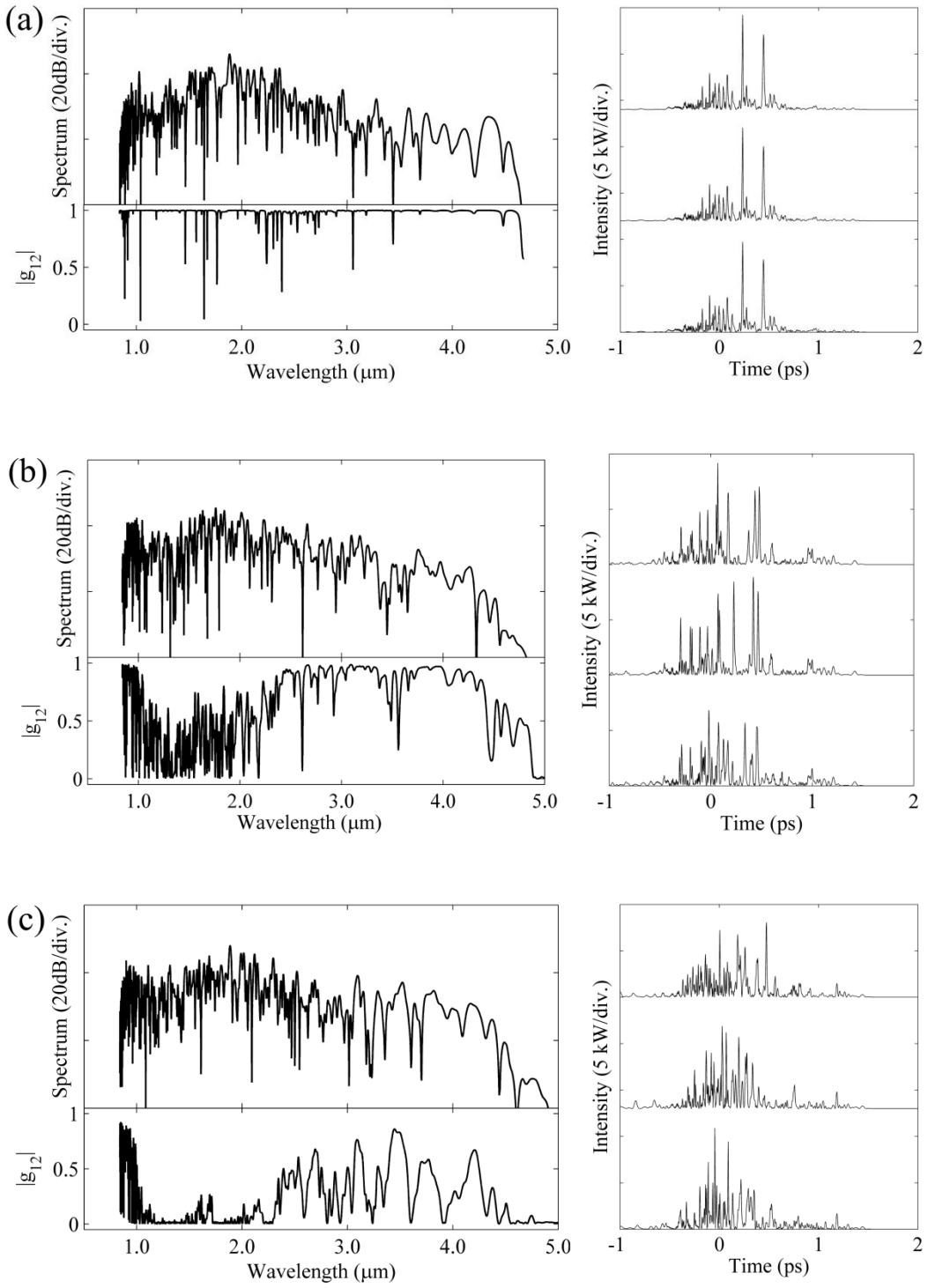

Figure 4.6. Spectra and coherence degree $|g_{12}(\lambda)|$ for input pulses with FWHM of 200 fs and peak power of (a) 6 kW, (b) 9 kW, and (c) 11 kW. The temporal intensities for three simulations with random noise are shown on the right.

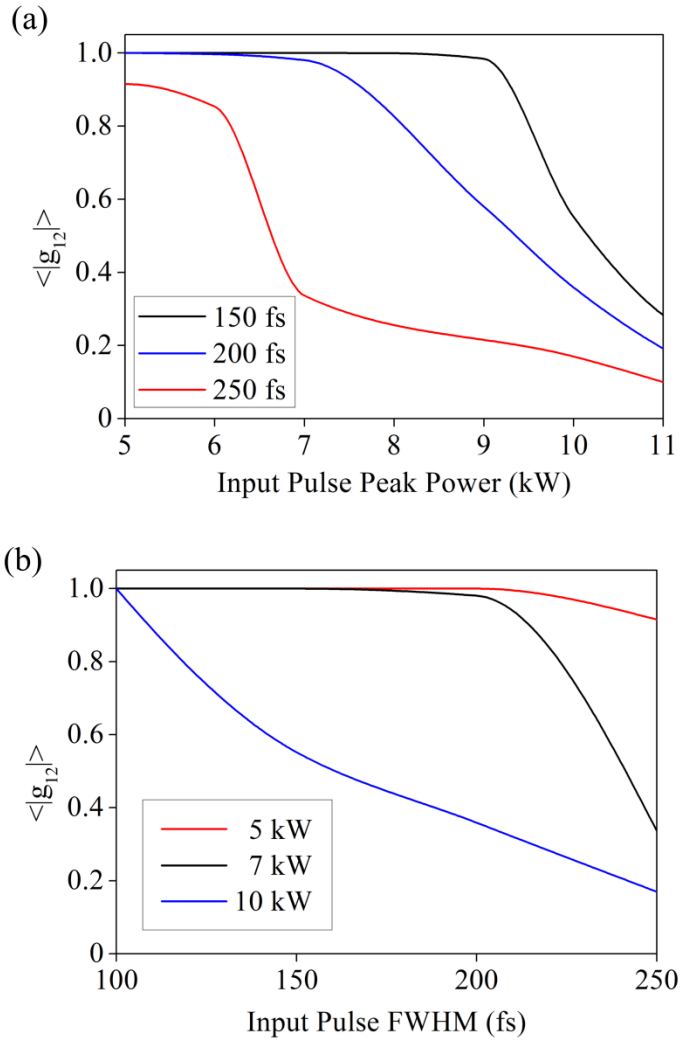

Figure 4.7 Overall degree of coherence $<|g_{12}|>$ versus: (a) input pulse peak power (with different pulse FWHM shown) and (b) input pulse width (with different peak power shown).

4.3.3 Physical Mechanisms of Coherence Degradation

The mechanism of the coherence degradation can be understood as the competition between soliton-fission process and modulation instability (MI). MI is the splitting of wave into pulse-like structures based on the amplification of noise fluctuations. In soliton-fission process, the phase relationship of the pulse is maintained, and the generated spectral components are fully coherent. However, as is shown in Equation (3.2.4), the soliton number N increases for a pump pulse with longer duration or larger power. In this case, MI rather than soliton fission starts to dominate the breakup of the input pulse envelope in the early stage of spectrum broadening. The noise-seeded feature of MI leads to the fluctuation of the spectral phase and amplitude, and the induced frequency components become completely incoherent. This can be seen in Figures 4.5 and 4.6, where the temporal intensities for three simulations with random quantum noise are plotted. With low pulse width and peak power, the noise has a small impact on the pulse propagation, and the output temporal profile is stable. As the soliton number becomes larger, the temporal intensity exhibits the build-up of fast oscillations with random phase and amplitude, which indicates the occurrence of MI. Therefore, it is necessary to launch pulses with sufficiently short width and low power to achieve coherent SCG. It should be also noted that the coherence degree remains at a relatively high level around the pump center wavelength, as shown in Figure 4.1 and Figure 4.2. The reason is this small spectral region is mainly affected by self-phase modulation process and is not seriously perturbed by MI.

4.4 Conclusion

In this chapter, I have theoretically studied the coherence properties and noise sensitivities of the supercontinuum generated in dispersion-tailored lead-silicate optical waveguides including

microstructured fiber taper and tapered rib waveguide. The results indicate that the degree of coherence strongly depends on the parameters of the input pulse. For higher peak power or longer pulse width, significant coherence degradation can be observed, resulting from the competition between soliton-fission process and noise-seeded modulation instability. This work shows that it is possible to obtain a highly coherent and broadband supercontinuum with appropriate pumping conditions.

Chapter 5 On-Chip Flat Octave-Spanning Supercontinuum Generation

5.1 Introduction

Supercontinuum generation can be utilized in frequency metrology, optical coherence tomography, pulse compression, phase stabilization and many other applications. In particular, spectral uniformity or ripple over a wide wavelength range is a practically crucial parameter in some scenarios such as dense wavelength division multiplexing (DWDM) technology, which has been widely used in optical communications industry [1, 2]. It is well known that dispersion, nonlinearity and loss are the key factors in supercontinuum evolution [3-6]. When pumping in the normal dispersion regime, self-phase modulation and Raman effects dominate the spectral broadening [7, 8]; by contrast, in the anomalous dispersion regime, supercontinuum is dominated by soliton dynamics and modulation instability [9, 10]. Beyond the wavelength of ~2 μm, the onset of loss in conventional silica fibers motivates the use of soft glasses with wider transmission window such as fluoride [11], lead silicate [12-14], tellurite [15] and chalcogenide [16, 17]. Furthermore, the high intrinsic nonlinearities of non-silica materials also reduce the pump power requirement for SCG.

Recent progress of waveguide tapering technique has provided great opportunities for broadband supercontinuum. For example, a pressure-assisted melt-filling technique was applied to fabricate a chalcogenide-silica double-nanospike waveguide for mid-infrared (mid-IR) SCG [18]. In [19], octave-spanning supercontinuum was generated in *in situ* tapered chalcogenide fiber. It is shown that the spectral dispersion profile can be controlled by changing the structure and dimension of the tapered fibers. Based on this principle, non-uniformly tapered fibers with longitudinally-varying dispersion have been devised to generate continuum more efficiently [11-12, 20]. In [20],

Mori et al. presented the generation of flat and broadened spectrum in fibers with dispersion-decreasing convex profile. Chen et al. [11] described a method for mid-IR one-octave SCG in which the core size of a fluoride fiber was exponentially decreased to shift the zero dispersion wavelength (ZDW). In [12], numerical simulation predicted SC extending to ~ 4.8 μm in a lead silicate microstructured fiber with increasing core radius.

Compared to fiber-based nonlinear devices, planar waveguides are usually shorter and more applied in integrated optical systems with low cost. For this reason, supercontinuum generation in planar waveguides has gained much attention recently [21-27]. In [23], a dispersion-engineered highly nonlinear chalcogenide planar waveguide was experimentally demonstrated to acquire SC with a -60 dB bandwidth of over an octave. Zhang et al. [24] obtained an octave-spanning continuum from a silicon chip which achieved small and flat dispersion over wide bandwidth. Yu et al. [25] produced SC in a chalcogenide rib waveguide with ultrawide spectral width up to two octaves. Besides, supercontinuum has also been studied in several semiconductor planar waveguides such as hydrogenated amorphous silicon [26] and silicon nitride [27], with the advantage over silicon of lower nonlinear absorption.

These results indicate the possibility of dispersion management by modifying the planar waveguide geometry, similar to fibers. Then this raises the question of whether tapered rectangular waveguides can also enhance the efficiency of SCG processes to obtain a broadband and flat spectrum with low pump power and short waveguide length, which has been rarely addressed. Previously we reported the theoretical result of two-octave spanning SC in a dispersion-engineered tapered rib waveguide [28, 29]; however, the pump energy was relatively

high (~1 nJ) and the unevenness of the output spectrum could be detrimental in specific applications.

In this chapter, I report the design of a short tapered planar waveguide with varying dispersion along the propagation distance for supercontinuum generation. I discuss the specific dynamics and characteristics of pulse evolution in this waveguide structure, and prove the improvement in energy transfer towards mid-IR wavelengths. By launching into hyperbolic secant pulses with 45-pJ energy (0.8-kW peak power and 50-fs FWHM) at 1.55 μm, the generation of near-octave continuum with simultaneous wide bandwidth and outstanding flatness is achieved. The results show the potential of on-chip flat supercontinuum in particular applications.

5.2 Waveguide Design and Modelling

We consider a rib waveguide of SF57 glass on silica with rib width W = 4 μm, outer slab thickness d = 0.5 μm and etch depth h, as depicted in Figure 5.1. The upper cladding is air. Scott SF57 is a commercially available lead-silicate glass primarily composed of SiO_2 and PbO, with a Pb cationic content of 40-50% [30]. Compared to other compound glasses such as chalcogenide and heavy metal oxide glasses, SF57 exhibits higher thermal and crystallization stability and less steep viscosity curve with low softening temperature [31, 32]. The linear refractive index at the wavelength of 1.55 μm is 1.8 [33], which leads to an index contrast of 17.6% to the silica substrate for tight modal confinement. The nonlinear index is $n_2 = 4.1\times10^{-19}$ m^2/W at 1.06 μm, much higher than that of pure silica glass (2.7×10^{-20} m^2/W at 1.06 μm) [34]. The material intrinsic loss measured at 1.55 μm is 1.6 dB/m [32]. Multiphonon absorption determines the transmission limit at long wavelengths, and SF57 glass turns out to lose transparency beyond 5

μm due to strong Si-O bonding [35]. Because of the short length of our designed waveguide (1.8 cm), the absorptive property within the transmission window has a minor impact on supercontinuum propagation.

Figure 5.2 shows the wavelength-dependent dispersion profiles of the rib waveguides with different etch depths for the fundamental TM mode (vertically polarized). The material dispersion of SF57 bulk glass is also plotted for comparison. It can be seen from these curves the waveguide dispersion is strong enough to overcome the normal material dispersion at short wavelengths. Specifically, as the etch depth is increased from 0.55 μm to 0.70 μm, the second zero dispersion position is shifted towards longer wavelengths from 1.69 μm to 2.14 μm. On the contrary, it is worth noting that the dispersion profile does not change significantly by varying the rib width, as illustrated in Figure 5.3. In particular, for a waveguide with h = 0.6 μm and d = 0.5 μm, the ZDWs almost remain the same if W is altered from 3.5 μm to 4.5 μm. Therefore, the dispersion can only be controlled effectively by varying the etch depth. Since the waveguide is not fully etched and the rib height is much smaller than the width, the horizontally polarized TE mode experiences less waveguide dispersion than TM mode. Figure 5.4 shows the effective mode area as a function of wavelength for different etch depths and Figure 5.5 gives examples of the mode fields at 1.55 μm with h = 0.55 μm and h = 0.70 μm where the effective mode areas are 3.17 μm^2 and 3.33 μm^2, respectively, demonstrating tight modal confinement.

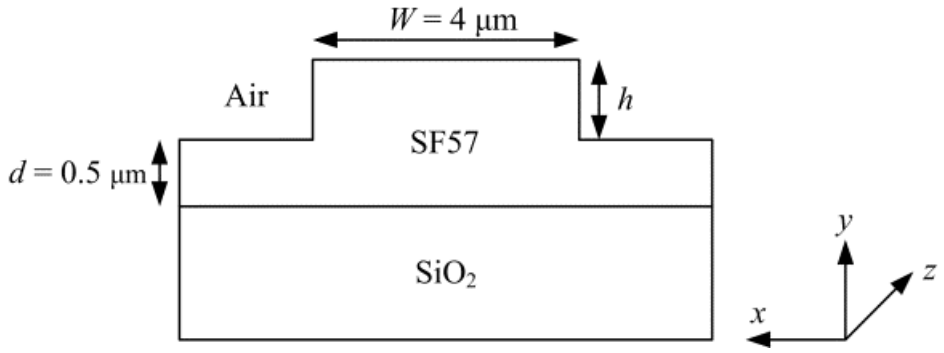

Figure 5.1 Cross section and parameters of the Air-SF57-SiO_2 planar rib waveguide.

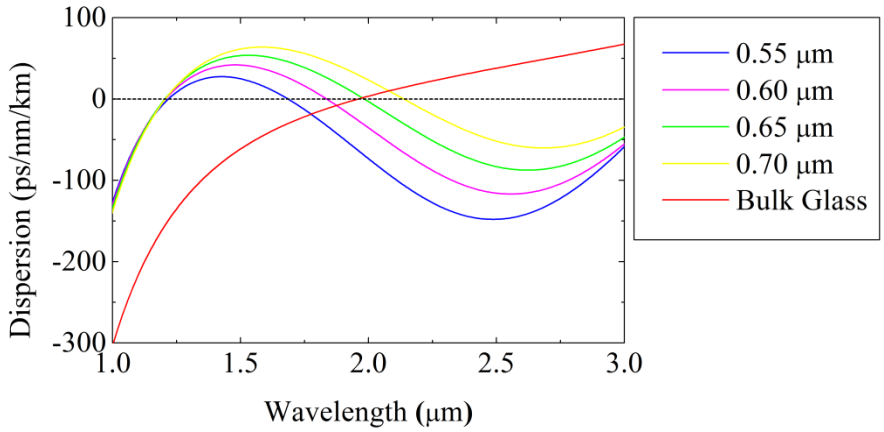

Figure 5.2 Spectral dispersion profiles of SF57 rib waveguides with different etch depths h (W = 4 μm, d = 0.5 μm).

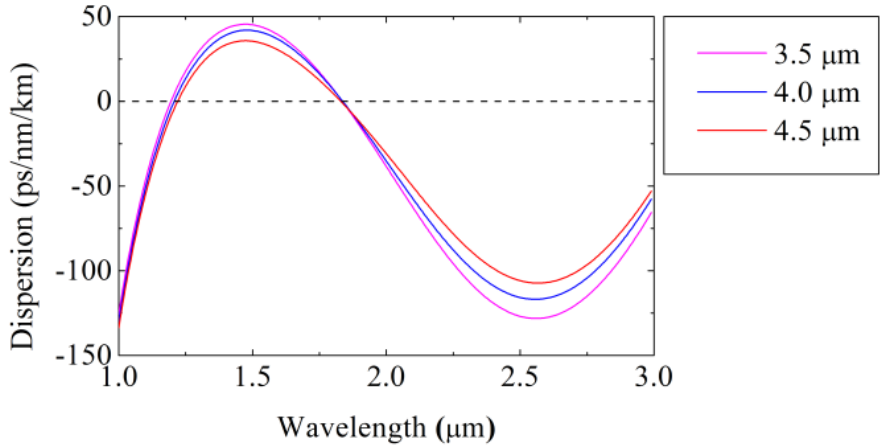

Figure 5.3 Spectral dispersion profiles of SF57 rib waveguides with different rib widths W (h = 0.6 μm, d = 0.5 μm). The ZDWs do not change significantly when W is altered.

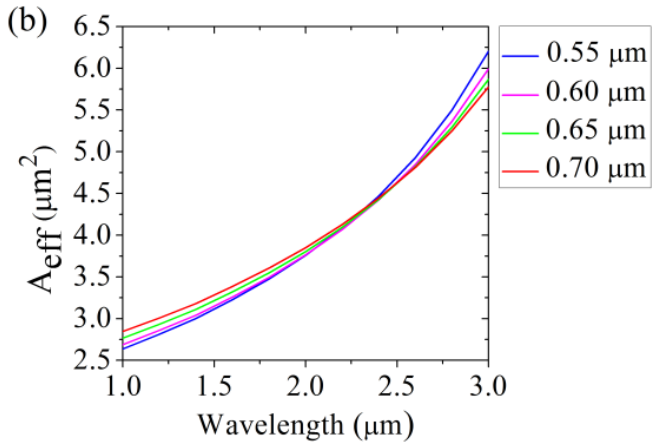

Figure 5.4 Effective mode areas of SF57 rib waveguides with different etch depths h (W = 4 μm, d = 0.5 μm).

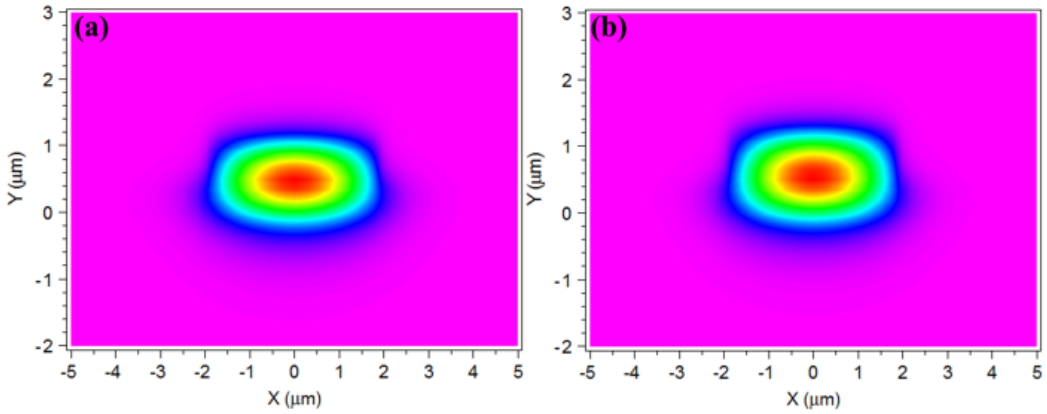

Figure 5.5 Mode fields for the fundamental TM mode at the wavelength of 1.55 μm when the etch depth is (a) 0.55 μm and (b) 0.70 μm (W = 4 μm, d = 0.5 μm). The effective mode areas are 3.17 μm^2 and 3.33 μm^2, respectively.

Based on the characteristics of the total dispersion, we have designed a vertically tapered structure for SCG as illustrated in Figure 5.6. The 1.8-cm long waveguide consists of three regions (denoted as I, II and III) with varying height along the propagation direction z. The etch depths h at the input and output are 0.55 μm and 0.70 μm, respectively. In region II, the waveguide is gradually etched from z = 1 cm to z = 1.375 cm such that h increases linearly. Note that planar waveguides with tapered height have been fabricated for different applications [36-38].

Supercontinuum propagation is simulated by launching into hyperbolic secant pulses centered at telecommunication wavelength of 1.55 μm. The peak power and full width at half maximum (FWHM) are 0.8 kW and 50 fs respectively, resulting in total pulse energy of 45 pJ. Note that the launched energy density is ~10^{-3} J/cm^2, well below the typical optical damage threshold of 1~100 J/cm^2 for optical glasses [39]. The generalized nonlinear Schrödinger equation (GNLSE) is numerically solved to model the pulse evolution.

When characterizing the evolving optical field, it is useful to introduce the frequency-resolved optical gating (FROG) technique by calculating the spectrogram, a function displaying the field in time and frequency domains simultaneously [40]. With the field E(t) to be analyzed, the spectrogram is defined by:

$$S(\omega, \tau)=\left|\int_{-\infty}^{+\infty} E(t)g(t-\tau)e^{-i\omega t}dt\right|^2 \qquad (5.2.1)$$

where g(t - τ) is a variable-delay gate function. In our simulation, the gate function used is the femtosecond input pulse.

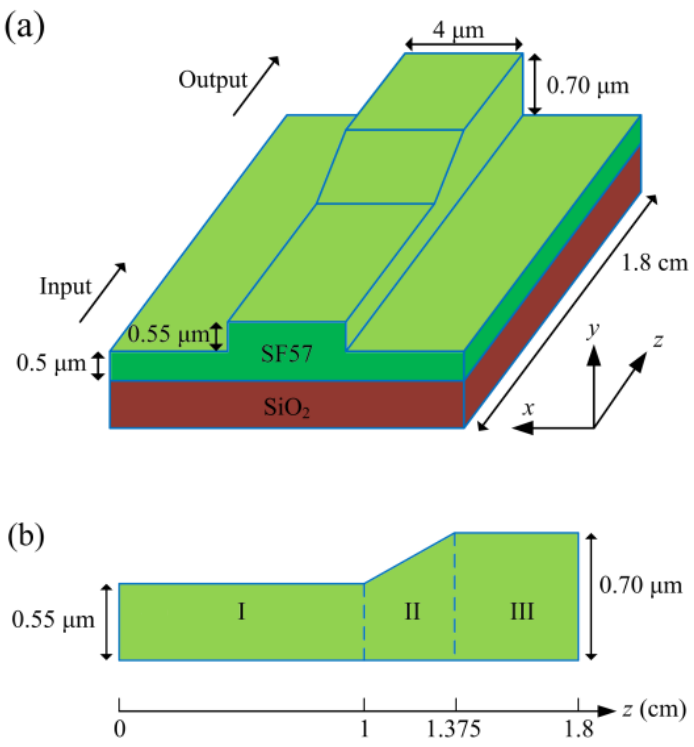

Figure 5.6 (a) Schematic of the tapered SF57 rib waveguide with longitudinally varying height. (b) Side view of the waveguide structure divided into three segments (I, II and III). The etch depth raises linearly from 0.55 µm to 0.70 µm in region II (z = 1-1.375 cm).

5.3 Simulation Results and Discussions

5.3.1 Soliton Fission and Dispersive Wave Generation in Uniform Planar Waveguides

We start with pulse propagation through uniform waveguide structures with various dispersion profiles. Figure 5.7 and Figure 5.8 illustrate the pulse evolution along z and output spectrograms at z = 1.8 cm when the etch depths are 0.60 μm and 0.70 μm, respectively. It should be noted the pump wavelength of 1.55 μm is in the anomalous dispersion regime, and SCG in this case is dominated by soliton dynamics. With a sech^2 input pulse, the injected soliton order is expressed as:

$$N = \sqrt{\frac{L_D}{L_{NL}}} = \sqrt{\frac{\gamma P T_0^2}{|\beta_2|}} \tag{5.3.1}$$

where P is the peak power, T_0 is the pulse width (FWHM = $1.763T_0$), $L_D = T_0^2/|\beta_2|$ is the dispersion length and $L_{NL} = 1/\gamma P$ is the nonlinear length. During the initial stage, the soliton undergoes temporal compression and spectral broadening. However, when the bandwidth reaches its maximum, the evolution begins to deviate from the ideal periodic behavior of a high-order soliton due to the perturbations of high-order dispersion and Raman effects. Instead, the pulse envelope breaks up into a train of N fundamental solitons, which is known as the soliton fission process. Generally, fission occurs at the distance of $L_{fiss} \sim L_D/N$. The pulse and waveguide parameters give N = 2.6 and $L_{fiss} \sim 0.62$ cm for h = 0.60 μm, while N = 2.0 and $L_{fiss} \sim 0.50$ cm for h = 0.70 μm. As a result of Raman scattering, the center wavelengths of the ejected solitons are continuously red-shifted.

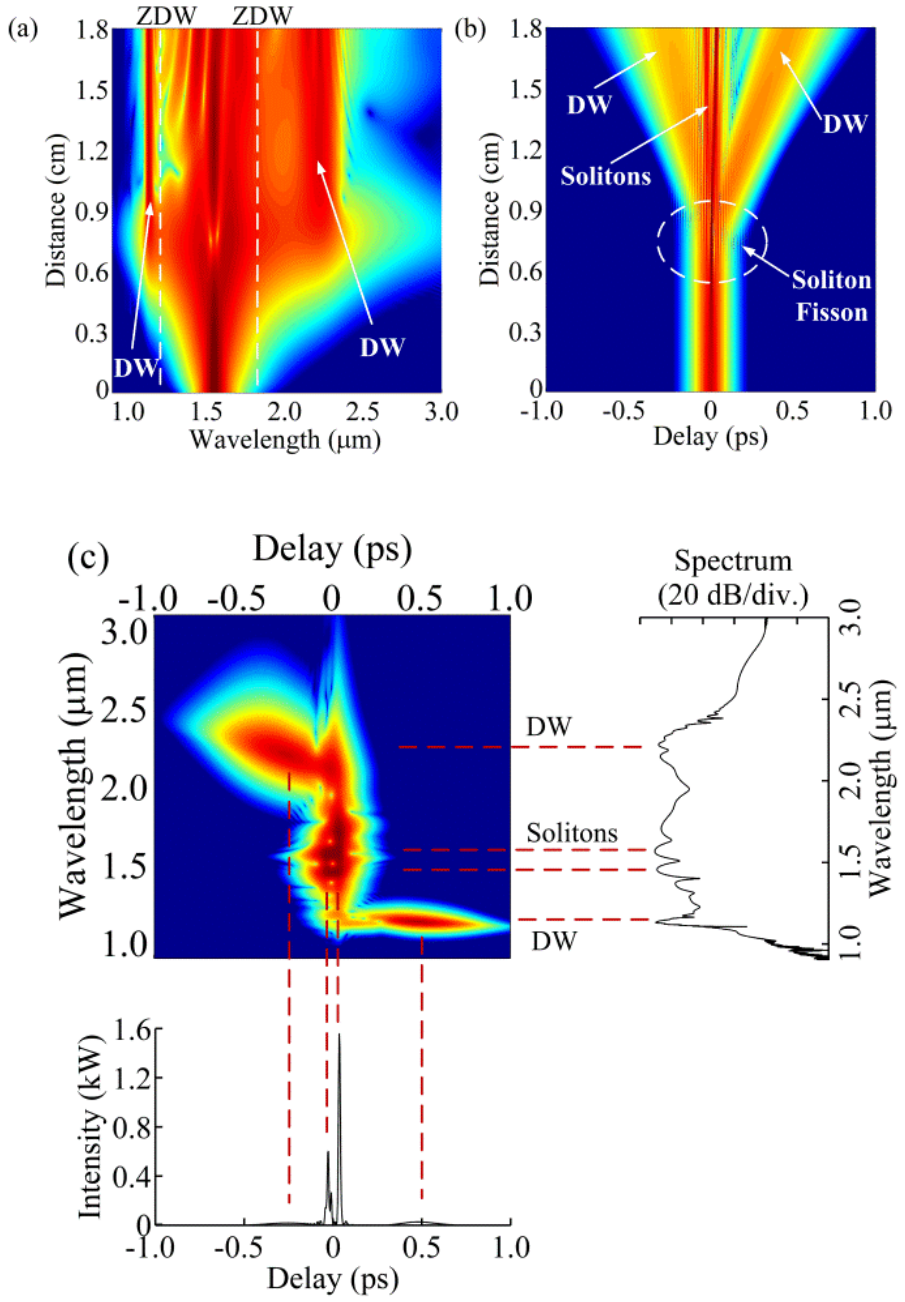

Figure 5.7 Pulse evolution (a) in the wavelength domain and (b) in the time domain, for a waveguide with h = 0.60 μm. Soliton fission length is L_{fiss} ~ 0.62 cm. (c) Output spectrogram projected onto temporal intensity (bottom) and spectrum (right).

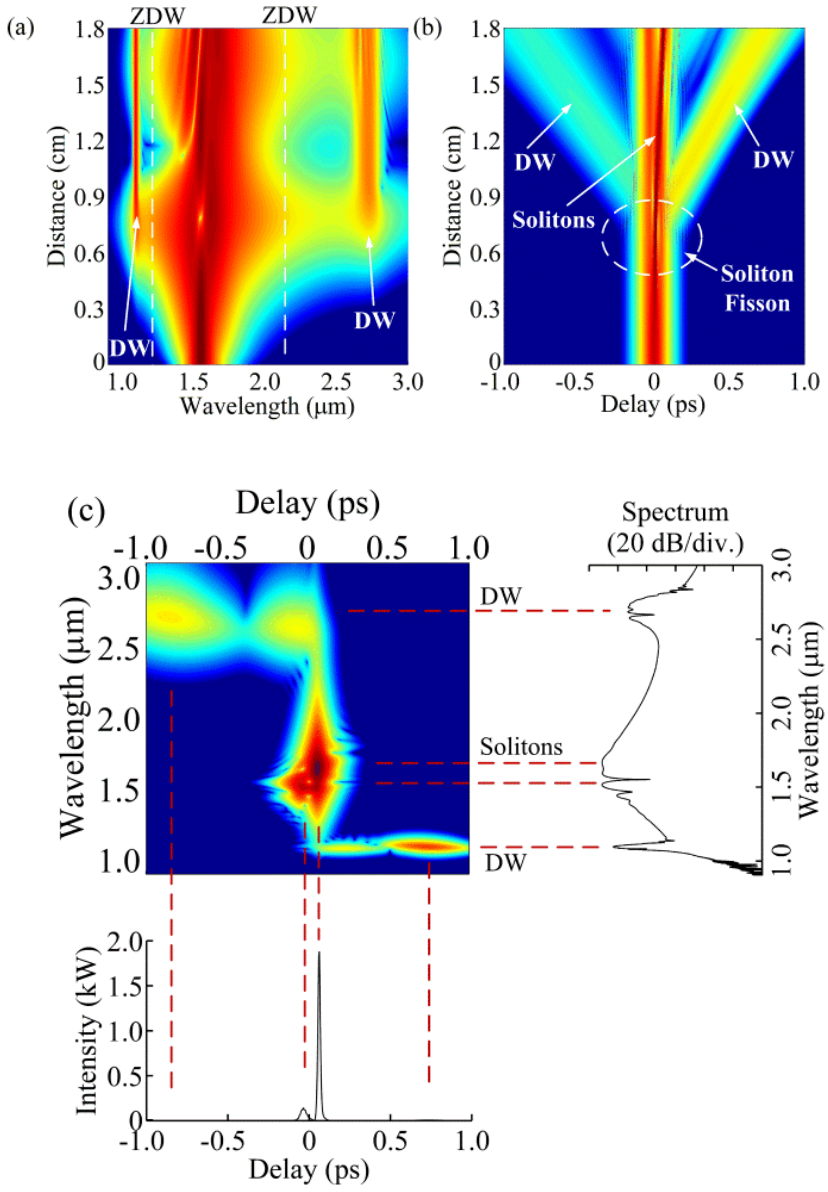

Figure 5.8 Pulse evolution (a) in the wavelength domain and (b) in the time domain, for a waveguide with h = 0.70 μm. Soliton fission length is L_{fiss} ~ 0.50 cm. (c) Output spectrogram projected onto temporal intensity (bottom) and spectrum (right).

The presence of high-order dispersion also causes the emission of dispersive waves (DWs) by the fundamental solitons. As can be seen in Figure 5.7 and Figure 5.8, the energy is transferred from solitons to the generated dispersive waves in the normal dispersion regime on short-wavelength side of the first ZDW as well as long-wavelength side of the second ZDW. It is necessary to satisfy the phase matching condition for DW radiation at the angular frequency ω_{DW}. If P_{sol} is the peak power of the soliton at ω_{sol}, the condition can be written as:

$$\frac{\gamma P_{\mathrm{sol}}}{2} = \sum_{k \geq 2} \frac{\beta_k(\omega_{sol})}{k!} \left(\omega_{DW} - \omega_{sol}\right)^k \tag{5.3.2}$$

Essentially equation (5.3.2) indicates the match between the wavenumbers of solitons (left side) and DWs (right side). Based on the specified pulse parameters, Figure 5.9 shows the calculated phase matched DW wavelengths across the 2nd ZDW in the mid-IR region, corresponding to waveguides with different heights. As the rib height is increased and the second ZDW is red-shifted, DWs are emitted towards longer wavelengths, leading to an increasing frequency detuning ($\delta = \omega_{sol} - \omega_{DW}$) between solitons and DWs. However, the amplitude of the radiation exponentially decreases with larger δ [41], and since the DW resonance is narrow-band, the spectral broadening is significantly mitigated by a gap between the pump and DW components. This is shown evidently in Figure 5.8 (c), where most of the energy is concentrated on the solitons rather than the dispersive waves. Therefore, SCG in a uniform SF57 planar waveguide is not sufficiently efficient to obtain a spectrum with excellent bandwidth and flatness simultaneously. Quantitatively, we find that the output spectra from the waveguides with h = 0.60 μm and h = 0.70 μm both decrease from the maximum by 20 dB at the wavelength of 1.9 μm, and by 40 dB at 2.4 μm.

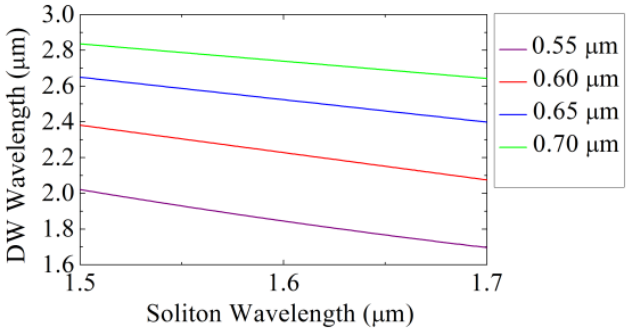

Figure 5.9 Phase matched dispersive wave wavelengths across the second ZDW for different waveguide etch depths.

5.3.2 Supercontinuum Generation in the Dispersion-Varying Planar Waveguide

The simulated propagation of a pulse with 0.8 kW peak power and 50 fs FWHM in the short tapered waveguide proposed in Section 5.2 is shown in Figure 5.10 and Figure 5.11. The output spectrum at z = 1.8 cm is broad and flat in the mid-IR range, with 20-dB bandwidth spanning nearly one octave from 1.31 μm to 2.53 μm, and 40-dB bandwidth from 1.07 μm to 2.58 μm, as shown in Figure 5.12. The effective mode area A_{eff} at the input is 3.17 μm^2, yielding a nonlinear parameter γ of 0.52 /W/m at 1.55 μm, roughly 500 times that of a conventional single-mode fiber. In region I (z = 0-1 cm) where the etch depth is 0.55 μm as depicted in Figure 5.6, the pulse experiences the initial phase of temporal compression and spectral broadening. Soliton fission and dispersive wave emission take place near the end of this region, since the fission length L_{fiss} when h = 0.55 μm is approximately 0.9 cm. In region II from z = 1 cm to z = 1.375 cm, the rib has a tapered structure with a linearly increasing height. As a result, the upper ZDW of the dispersion profile is shifted along the propagation distance, which causes a continuous modification of the phase matching condition. This allows the DWs to be produced gradually towards longer wavelengths, as illustrated in Figure 5.10 and Figure 5.11. The solitons continue to transfer energy to the dispersive wave components in region III, leading to sufficient growth of the spectral power over the entire spectrum. In this way, the spectral unevenness caused by the gap between solitons and DWs is successfully overcome, and the designed dispersion-varying planar waveguide clearly contributes to enhancing the efficiency of SCG process. In Figure 5.13, the output mode field quality for a few generated wavelengths (1.3, 1.7, 2.1 and 2.5 μm) is illustrated.

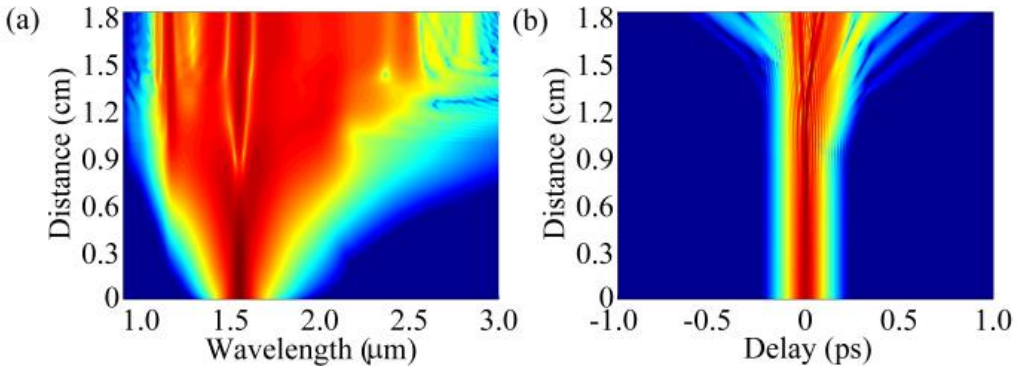

Figure 5.10 Pulse evolution through the tapered planar waveguide (a) in the wavelength domain and (b) in the time domain.

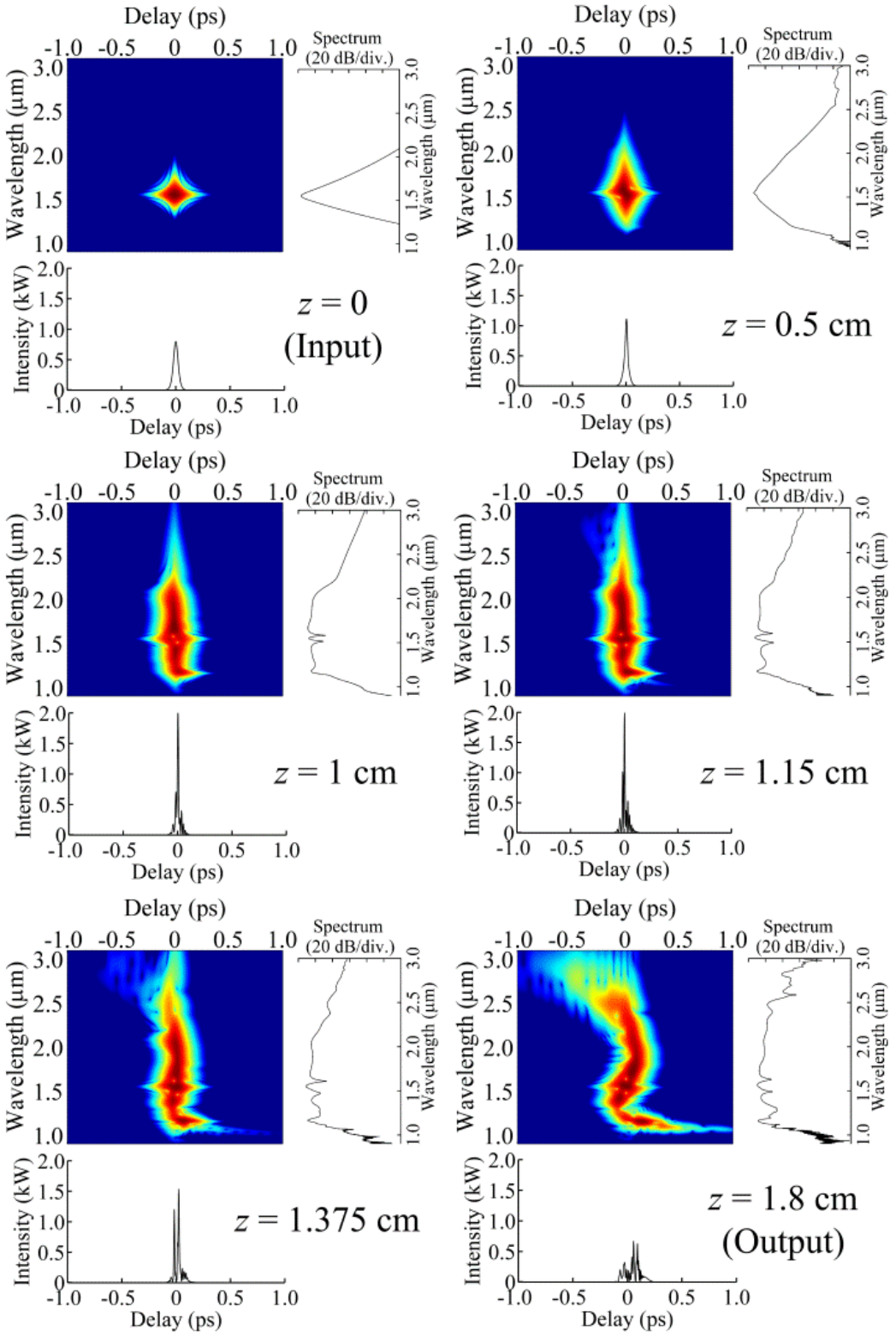

Figure 5.11 Spectrograms projected onto temporal intensity (bottom) and spectrum (right) at different propagation distance.

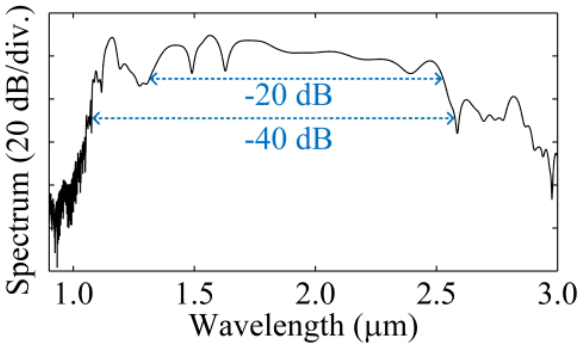

Figure 5.12 Output supercontinuum of the tapered waveguide with 20-dB and 40-dB bandwidths shown.

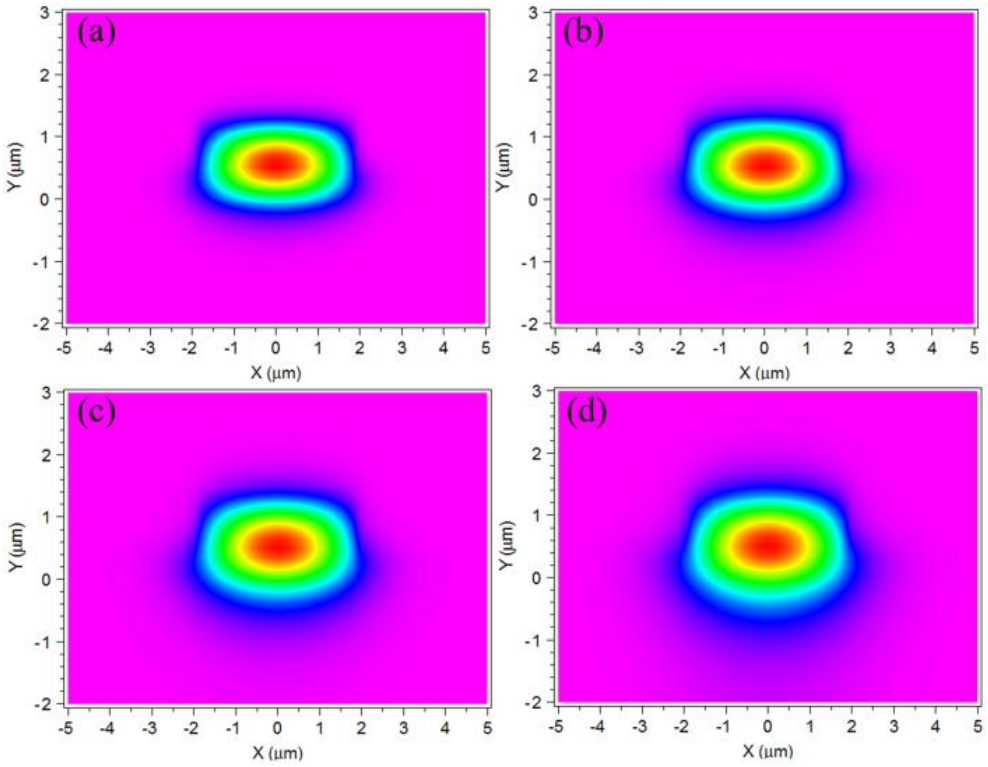

Figure 5.13 The output mode fields at several wavelengths generated through SCG: (a) 1.3 μm; (b) 1.7 μm; (c) 2.1 μm and (d) 2.5 μm.

Note that other taper structures may also be effective. Nonetheless, the shift of dispersion along the waveguide length should be optimized to ensure efficient energy transfer. If the ZDW varies too rapidly, the amplification of DW power is suppressed, and the spectrum cannot spread out; on the other hand, if the ZDW shifts too slowly, the solitons may lose most of the energy before DWs at longer wavelengths are emitted. This is shown in Figure 5.14, in which the spectrum evolution through waveguides with different tapering lengths (i.e., the lengths of region II) demonstrates the significance of optimization of the waveguide structure. With tapering lengths of 0.075 cm, 0.225 cm, 0.525 cm and 0.675 cm, the resulting mid-IR spectra at -20 dB level are 1.63~2.51 μm, 1.49~2.48 μm, 1.31~2.30 μm and 1.32~2.25 μm, respectively, narrower than the optimized waveguide geometry (tapering length of 0.375 cm). Therefore, the dispersion characteristic should be carefully tailored to achieve desired output spectrum. Meanwhile, the resulting supercontinuum is also sensitive to the pump parameters. In this work, we choose the input pulse with 0.8-kW peak power and 50-fs duration to ensure low pulse energy as well as high soliton order (N = 2~3). If pumping with pulses of longer durations such that $N \gg 10$, modulation instability rather than soliton fission will play dominant roles in SCG [10].

Our result is comparable with that presented in [11], where a 600-cm non-uniform fluoride fiber taper with blue-shifted ZDW was designed to produce one-octave continuum spanning 1.5-3 μm. It was pumped by pulses with 8.8 kW peak power and 1 nJ energy. We have predicted SCG with similar bandwidth from a planar waveguide with substantially shorter length and lower pump energy (45 pJ). In [24], flat SC extending from 1.2 μm to 2.5 μm at -33 dB level was obtained from a silicon chip. The input pulse energy was as low as 6.8 pJ and the propagation distance was 6 mm. The flatness of the output spectrum was achieved by embedding a nanoscale slot in

the rib to flatten the dispersion profile. However, it turned out SCG in silicon could seriously suffer from two-photon absorption in some cases. We have proposed a different approach that further improves the spectral uniformity (with similar bandwidth at -20 dB level).

5.4 Conclusion

In this chapter, I have proposed a tapered SF57 rib waveguide for flat mid-IR supercontinuum generation. The waveguide length is 1.8 cm, and the etch depth increases linearly from 0.55 μm to 0.70 μm in the segment of z = 1-1.375 cm. The incident pulse centered at telecommunication wavelength of 1.55 μm with 800-W peak power, 50-fs FWHM and 45-pJ energy undergoes soliton fission and dispersive wave radiation giving rise to spectral broadening. Due to the gradual modification of dispersion profile and phase matching condition for DW emission, the tapered waveguide overcomes the limitation of spectral flatness in uniform waveguide structures and improves the efficiency of energy transfer towards longer wavelengths. The resulting near-octave supercontinuum extends from 1.31 μm to 2.53 μm at -20 dB level, and from 1.07 μm to 2.58 μm at -40 dB level. This on-chip SC source may be important for particular applications in integrated optical systems.

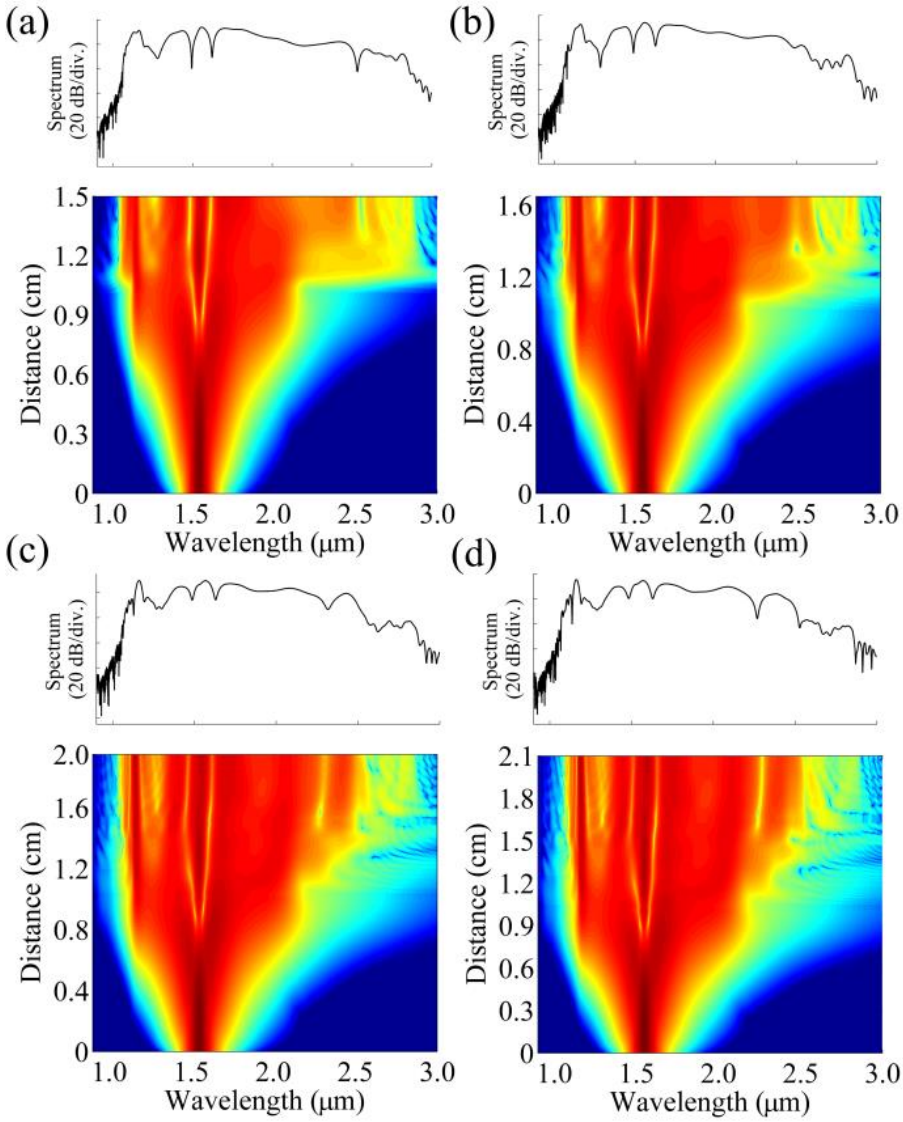

Figure 5.14 Spectrum evolution and output spectra for waveguides with tapering lengths of (a) 0.075 cm, (b) 0.225 cm, (c) 0.525 cm and (d) 0.675 cm. The etch depth at the input and output, and the lengths of segments I and III stay the same.

Chapter 6 Hybrid Mode-Locked Fiber Ring Laser Using Graphene Saturable Absorber

6.1 Introduction

Generation of high-speed optical pulse train with ultrashort pulse width has been investigated extensively in the past decades, and is still of interest to researchers due to its diverse applications in optical communication, optical frequency metrology, material processing, biomedical diagnostics, micromachining and many others [1-5]. Among various platforms, passively mode-locked fiber lasers have been successfully constructed to generate subpicosecond pulses by making use of nonlinear devices such as saturable absorbers [6-8]. Moreover, recent advances in materials have further expanded opportunities for robust and cost-effective pulse lasers [9-13]. Since the initial report by Bao *et al.* [14], mode-locked fiber lasers based on graphene saturable absorbers have attracted much attention due to their outstanding properties including ultrafast recovery time, wide range wavelength tunability, low saturation power, large modulation depth, and high damage threshold [14-22]. Despite the fact that those graphene-based lasers can produce ultrashort femtosecond pulses, the passive mode-locking scheme suffers from the drawback of low repetition rate, which is generally at MHz-level.

Active mode-locking technique has been proven to be an effective way to acquire high-repetition-rate pulses by incorporating a modulator inside the laser cavity. In particular, the implementation of rational harmonic mode-locking is able to overcome the modulator bandwidth limitation and further increase the repetition rate by detuning the modulation frequency a fraction of the cavity fundamental frequency from the harmonic frequency [23–26]. However, the pulse duration is usually larger than that from a passively mode-locked laser. A possible solution

would be to build a hybrid mode-locked system incorporating both active and passive mode lockers [27, 28]. Nonetheless, the combination of rational harmonic mode-locking and graphene saturable absorber has not been explored yet.

In this chapter, I report a novel scheme of hybrid mode-locked erbium-doped fiber ring laser using graphene as a saturable absorber. A 20-GHz optical pulse train is generated by applying rational harmonic mode-locking technique, and with the insertion of a graphene saturable absorber, the pulse width can be shortened by a compression factor of 0.53 from 5.28 ps to 2.82 ps.

6.2 Experimental Setup

In order to prepare the saturable absorber (SA), various methods have been described, such as chemical vapor deposition [14], mechanical exfoliation [15], and optical deposition [22]. A critical issue is that the properties of the SA rely on the thickness of the graphene layers, and self-aggregation of the particles would increase the absorption loss while decreasing the modulation depth [14]. We use a simple method to fabricate the graphene SA with desired features. The graphene material used in this work is purchased from Graphene Laboratories Inc. The 12-nm few-layer graphene flakes are placed on a piece of scotch tape and pressed repeatedly to adjust the thickness. Afterwards, the graphene nanopowder is directly deposited onto the previously cleaned end-face of a standard FC/APC fiber patchcord connector by pressing the ferrule to the tape. The patchcord is then tightly connected with another surface-cleaned patchcord using an FC/APC adapter.

Figure 6.1 presents the schematic diagram of the fiber ring laser. A 23-m-long erbium-doped fiber (EDF) pumped by a 980-nm laser diode serves as the gain medium. A $LiNbO_3$ Mach-Zehnder (MZ) modulator driven by ~10 GHz radio frequency (RF) signal and a graphene SA are incorporated in the ring cavity simultaneously to realize hybrid mode-locking. An isolator is employed to ensure unidirectional operation. With the aid of an intra-cavity polarization controller (PC), a stable pulse train can be generated and the laser output is extracted using a 90/10 optical coupler. All the components are connected by standard single-mode fibers (SMFs) with a total length of ~30 m.

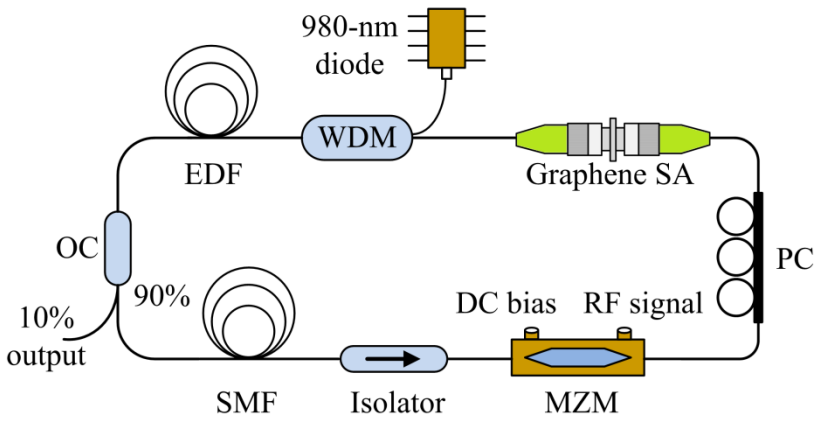

Figure 6.1 Schematic of the hybrid mode-locked fiber ring laser. EDF: Er-doped fiber, MZM: Mach-Zehnder modulaor, PC: polarization controller, SA: saturable absorber, SMF: single-mode fiber, OC: optical coupler, WDM: wavelength-division multiplexer.

6.3 Experiment Results and Discussions

6.3.1 Graphene Saturable Absorber

To characterize the prepared graphene saturable absorber, we have measured the intensity dependent absorption as illustrated in Figure 6.2. The optical transmittance of the absorber is correlated with the linear absorption α_{lin} and nonlinear absorption $\alpha_{non}(I)$ expressed as:

$$T(I) = \exp[-(\alpha_{non}(I) + \alpha_{lin})] \tag{6.3.1}$$

The saturable absorbance $\alpha_{non}(I)$ is given by:

$$\alpha_{non}(I) = \alpha_0 (1 + \frac{I}{I_{sat}})^{-1} \tag{6.3.2}$$

where I_{sat} is the saturation intensity. The fitting curve yields $\alpha_{lin} = 0.609$, $\alpha_0 = 2.14$ and $I_{sat} = 6.06$ kW/cm^2 respectively, with a modulation depth of 48.0%.

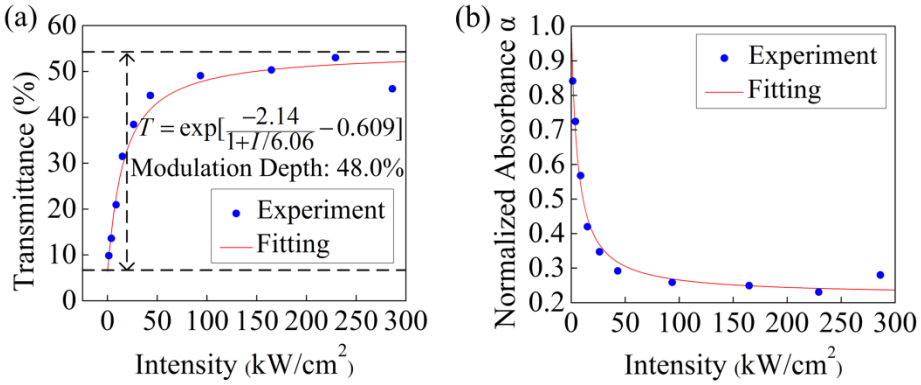

Figure 6.2 (a) Transmittance and (b) normalized absorption of the graphene SA as a function of input intensity.

6.3.2 Rational Harmonic Active Mode-Locking

A 20-GHz pulse train is firstly obtained from the ring cavity shown in Figure 6.1 with the graphene saturable absorber removed. The fiber laser with a MZ modulator incorporated is actively mode-locked by carefully tuning the frequency of the RF signal and the polarization controller. When the fundamental frequency of the cavity is f_c and the modulation frequency f_m satisfies the condition $f_m = (n+1/p)f_c$, where n and p are both integers, the laser resonator operates in the rational harmonic mode-locking (RHML) regime and pulses with a repetition rate of $(np+1)f_c$ can be produced. In our case, f_c is 4.29 MHz, and f_m is set at $(2329+1/2)f_c \approx 9.99$ GHz to realize 2nd order RHML. Figure 6.3 shows the measured characteristics of the generated pulse train. The average output power is 1.7 dBm (1.5 mW). As can be observed from the oscilloscope trace, the spacing between adjacent pulses is 50 ps, which corresponds to 20 GHz repetition rate. This is also confirmed by the recorded RF spectrum shown in Figure 6.3(b), where the peak with the largest amplitude locates at 19.98 GHz frequency. The result also shows low supermode noise with a signal-to-noise ratio of 25 dB.

Figure 6.3(c) shows the optical spectrum centered at 1561 nm, with a 3-dB bandwidth of 0.80 nm. The autocorrelation trace of the pulse is presented in Figure 6.3(d). Assuming a hyperbolic secant pulse profile, the full width at half maximum (FWHM) is measured to be 5.28 ps. It turns out the time-bandwidth product (TBP) is equal to 0.520, not close to the transform-limit value for $sech^2$ pulses (0.315). This implies that the dispersion and nonlinearity of the fibers induce chirp in the pulses, which can be compensated by guiding the output through an external dispersion-compensation scheme as previously demonstrated in [29]. Here we focus on the influence of a graphene SA inside the cavity on the generated pulse train.

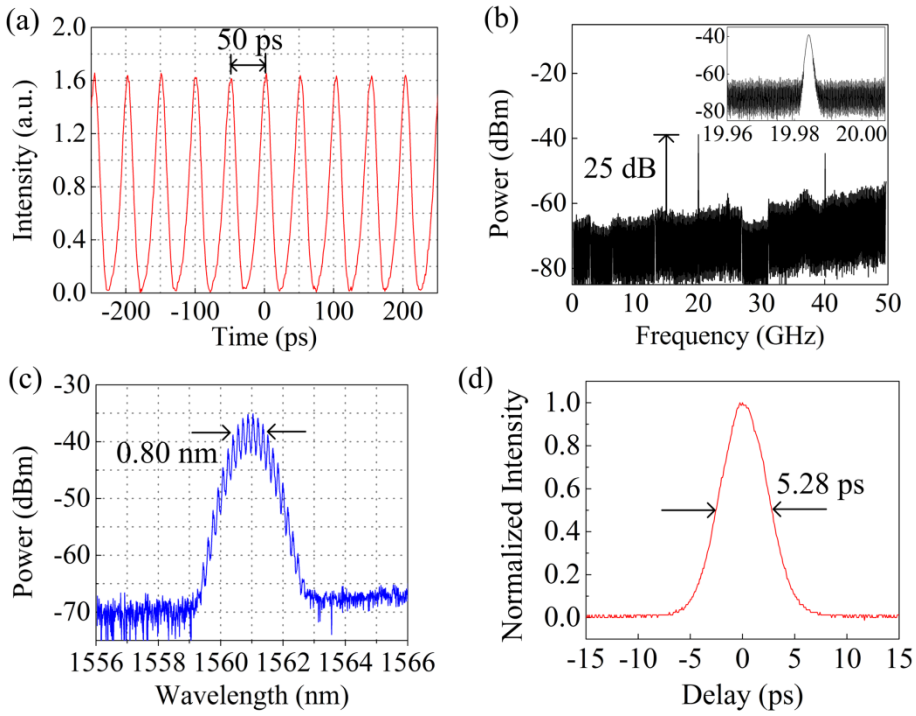

Figure 6.3 The measured (a) oscilloscope trace, (b) RF spectrum, (c) optical spectrum, and (d) autocorrelation trace of the 20-GHz pulse train from the rational harmonic mode-locked laser.

6.3.3 Hybrid Mode-Locking With a Graphene Saturable Absorber Within Laser Cavity

We demonstrate the realization of a hybrid mode-locked fiber laser by involving a graphene saturable absorber in the ring cavity as shown in Figure 6.1. The length of the SMFs is carefully adjusted to ensure the insertion of the SA does not drift the cavity's fundamental frequency significantly. As a consequence, 20-GHz pulse train can be obtained with the same experimental conditions. However, the combination of an active and passive mode locker results in the improvement of the laser performance by compressing the pulse duration, as seen in Figure 6.4. The FWHM of the pulse is shortened to 2.82 ps, indicating a compression factor of 0.53. Meanwhile, it is worth noting that the bandwidth of the optical spectrum is broadened to 1.38 nm, leading to a TBP value of 0.479. Due to the insertion loss introduced by the SA, the output power is reduced to -2.8 dBm (0.52 mW) and the signal-to-noise ratio becomes 15 dB.

In this case, the role of the active mode locker is to produce a high-speed optical pulse train. The modulator is capable of being driven at a frequency equal to a high multiple of relatively low fundamental frequency, thus the generated pulse train has a high repetition rate at the level of a few GHz. Furthermore, by applying the RHML technique, even higher repetition rate can be easily reached. However, this is rarely accomplished by passive mode lockers, especially graphene saturable absorbers. In [16], a passively harmonic mode-locked fiber laser based on a graphene saturable absorber was described. The fundamental cavity frequency (106 MHz) was relatively high by making the total cavity length short (~2 m) and the repetition rate was 2.22 GHz corresponding to the 21st harmonic. Martinez *et al*. [17] reported a passively mode-locked fiber laser using graphene as a saturable absorber, which operated at a fundamental repetition rate of 9.67 GHz by reducing the cavity length to as short as 10 mm. In our case, the fundamental

frequency is 4.29 MHz based on the total cavity length of ~50 m, and the modulation frequency corresponds to more than 2000th harmonic.

On the other hand, the passive graphene mode locker acts as a pulse compressor. This is expected since the recovery time of graphene (~ 200 fs [18]) is much shorter than the pulse width, hence the transmittance reacts to the instantaneous intensity of the injected light. As can be seen in equation (6.3.2), the central part of the pulse with higher intensity experiences less absorption than the leading and trailing edges, which gives rise to pulse narrowing. The optimal compression happens, however, within a limited range of the saturation intensity I_{sat}. If I_{sat} is much larger than the pulse intensity, no saturation will occur; whereas if I_{sat} is much weaker than the pulse intensity, the absorbance will be saturated over nearly all of the pulse. Therefore, it is crucial to make an SA with desired saturation intensity. Note that our results are comparable with that reported in [30], where a hybrid mode-locked fiber laser with single-wall carbon nanotubes as saturable absorbers was built to obtain a 4-GHz pulse train. The laser system was initially harmonically mode-locked via an electro-optical modulator, while the involvement of the absorber shortened the pulse width by a factor of 0.52. We have combined rational harmonic mode-locking with graphene saturable absorbers to achieve a similar compression factor as well as much higher repetition rate (20 GHz).

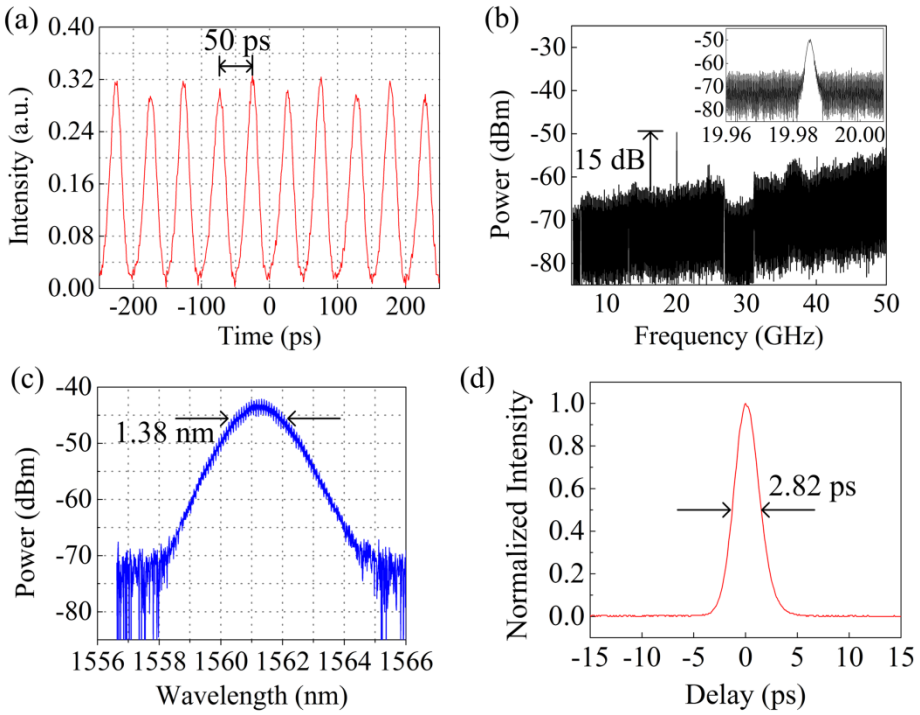

Figure 6.4. The measured (a) oscilloscope trace, (b) RF spectrum, (c) optical spectrum, and (d) autocorrelation trace of the 20-GHz pulse train generated by the hybrid mode-locked laser.

6.4 Numerical Simulation

We have also conducted simulation of the laser operation. The generalized nonlinear Schrödinger equation (GNLSE) governs light propagation along the fibers [31]:

$$\frac{\partial A(z,\tau)}{\partial z}+\frac{\alpha}{2}A(z,\tau)+\sum_{k\geq 2}\frac{i^{k-1}}{k!}\beta_k\frac{\partial^k A(z,\tau)}{\partial \tau^k}=\frac{g}{2}A(z,\tau)+\frac{g}{2\Omega_g^2}\frac{\partial^2 A(z,\tau)}{\partial \tau^2}+i\gamma A(z,\tau)\left|A(z,\tau)\right|^2 \quad (6.4.1)$$

Here A(z, τ) is the pulse envelope, z is the propagation distance, τ is the time-delay parameter, α is the fiber loss, γ is the nonlinear parameter, and β_k represent the dispersion coefficients. The gain saturation effect of the erbium-doped fiber should be taken into account by expressing the gain factor as $g = g_0/(1+E/E_{sat})$, where g_0 is the small signal gain, E is the pulse energy and E_{sat} is the gain saturation energy. Ω_g denotes the gain bandwidth. Pulse propagation in the passive SMF is simulated simply by setting g = 0.

Equation (6.3.1) models the graphene saturable absorber. The MZ modulator driven by an RF source can be described by the following single-pass transmission function [32]:

$$T=\cos^2\left(\pi\frac{V_b+V_m\sin(2\pi f_m\tau)}{V_\pi}\right) \quad (6.4.2)$$

in which V_π is the voltage required for a phase shift of π, V_b is the DC voltage bias, V_m and f_m are the amplitude and frequency of the RF signal, respectively.

The parameters of the fiber laser components used for modeling are provided in Table 6.1, in which dispersion terms up to the 3rd order are included. Simulation is initiated by launching into the system a seed pulse with small amplitude. The pulse evolution within the ring cavity is then iteratively modeled until a steady state is reached after many roundtrips. The split-step Fourier method is utilized to solve the GNLSE numerically.

Component	Parameter	Value
EDF	Length	23 m
	2nd dispersion β_2	-0.130×10^{-3} ps^2/m
	3rd dispersion β_3	0.135×10^{-3} ps^3/m
	Nonlinear parameter γ	3.69×10^{-3}/W/m
	Small signal gain g_0	1.09 dB/m
	Gain saturation energy E_{sat}	0.1 pJ
	Gain bandwidth	10 nm
SMF	Length	30 m
	2nd dispersion β_2	-21.7×10^{-3} ps^2/m
	3rd dispersion β_3	0.182×10^{-3} ps^3/m
	Nonlinear parameter γ	1.41×10^{-3}/W/m
MZM	Half-wave voltage V_π	6 V
	DC bias V_b	0 V
	Modulation amplitude V_m	6 V

Table 6.1 Fiber laser parameters used for simulation

Figure 6.5 and Figure 6.6 depict the simulated pulse development and the steady-state solutions of the output pulses, respectively. The FWHM is 5.47 ps when operated solely in the RHML regime, and narrowed by a factor of 0.52 to 2.85 ps in the hybrid mode-locking regime, in good agreement with the experimental results. It should be mentioned that the asymptotic state is independent on the seed pulse. Output pulses having the same characteristics can be obtained when pumped by white noise in the simulation as well.

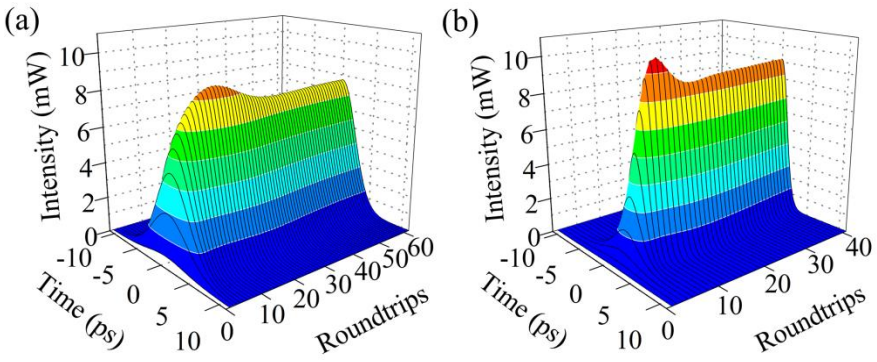

Figure 6.5 Simulated pulse generation from fiber lasers implementing (a) only rational harmonic active mode-locking and (b) hybrid mode-locking.

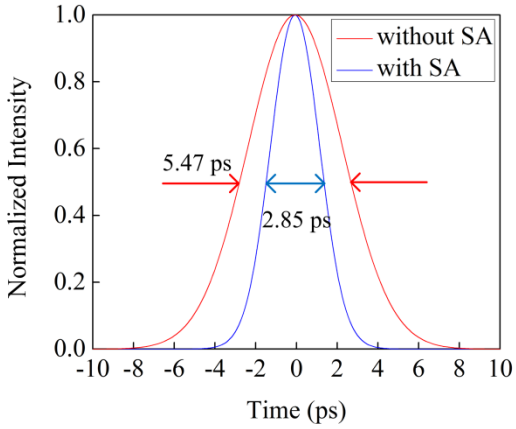

Figure 6.6 Comparison between the simulated output pulses generated from fiber lasers implementing rational harmonic active mode-locking and hybrid mode-locking.

6.5 Conclusion

In this chapter, I have designed and experimentally demonstrated a hybrid mode-locking scheme, which combines rational harmonic mode-locking technique and an easy-to-fabricate graphene mode locker, to improve the performance of an erbium-doped fiber ring laser generating an optical pulse train with high repetition rate and ultrashort pulse width. The laser is operated at 20 GHz via driving the intra-cavity $LiNbO_3$ Mach-Zehnder modulator at the frequency of ~10 GHz to achieve 2nd rational harmonic mode-locking. By inserting a graphene saturable absorber with 6.06 kW/cm^2 saturation intensity and 48.0% modulation depth in the cavity, the output pulse FWHM can be compressed by a ratio of 0.53 from 5.28 ps to 2.82 ps, accompanied by a small change in the time-bandwidth product. The average output power is 0.52 mW and the supermode suppression is 15 dB. Pulse development in the laser ring cavity has also been numerically simulated, which agrees well with the experimental results.

Appendix A Presentation and Publication

A.1 Conference Presentation and Proceedings

1. X. Zhang, **H. Hu**, W. Li, and N. K. Dutta, "Supercontinuum generation in dispersion-varying microstructured optical fibers," Proc. SPIE 9834, Laser Technology for Defense and Security XII, 98340F, 2016.
2. X. Zhang, W. Li, **H. Hu**, and N. K. Dutta, "Broadband on-chip mid-IR supercontinuum generation," Proc. SPIE 9832, Laser Radar Technology and Applications XXI, 983211, 2016.
3. **H. Hu**, X. Zhang, W. Li, and N. K. Dutta, "Hybrid mode-locked fiber ring laser using graphene and charcoal nanoparticles as saturable absorbers," Proc. SPIE 9836, Micro- and Nanotechnology Sensors, Systems, and Applications VIII, 983630, 2016.
4. X. Zhang, W. Li, **H. Hu**, and N. K. Dutta, "Two-photon absorption-based optical logic," Proc. SPIE 9467, Micro- and Nanotechnology Sensors, Systems, and Applications VII, 946731, 2015.
5. **H. Hu**, W. Li, X. Zhang, and N. K. Dutta, "Broadband Supercontinuum Generation in a Tapered-Rib Lead-Silicate Waveguide," International Journal of High Speed Electronics and Systems, vol. 24, no. 03n04, 1550009, 2015.
6. W. Li, **H. Hu**, X. Zhang, and N. K. Dutta, 2015. "High Speed All Optical Logic Gates Using Binary Phase Shift Keyed Signal Based On QD-SOA," International Journal of High Speed Electronics and Systems, vol. 24, no. 03n04, 1550005, 2015.
7. **H. Hu**, W. Li, and N. K. Dutta, "Supercontinuum generation in tapered rib waveguide," Proc. SPIE 9202, Photonics Applications for Aviation, Aerospace, Commercial, and Harsh Environments V, 92021C, 2014.

8. W. Li, **H. Hu**, and N. K. Dutta, "High speed all-optical PRBS generation using binary phase shift keyed signal based on QD-SOA," Proc. SPIE 9202, Photonics Applications for Aviation, Aerospace, Commercial, and Harsh Environments V, 92020O, 2014.
9. W. Li, **H. Hu**, and N. K. Dutta, "Optical latches using optical amplifiers," Proc. SPIE 8720, Photonic Applications for Aerospace, Commercial, and Harsh Environments IV, 87200O, 2013.
10. **H. Hu**, W. Li and N. K. Dutta, "Wide-band coherent supercontinuum generation," Proc. SPIE 8733, Laser Technology for Defense and Security IX, 87330C, 2013.
11. **H. Hu**, W. Li, S. Ma and N. K. Dutta, "Supercontinuum generation in dispersion-tailored lead-silicate fiber taper," Proc. SPIE 8647, Next-Generation Optical Communication: Components, Sub-Systems, and Systems II, 86470O, 2013.
12. S. Ma, W. Li, **H. Hu**, and N. K. Dutta, "Ultra-short pulsed fiber ring laser using photonic crystal fiber," Proc. SPIE 8381, Laser Technology for Defense and Security VIII, 838116, 2012.
13. S. Ma, W. Li, **H. Hu**, and N. K. Dutta, "Optical processors using semiconductor optical amplifiers," Proc. SPIE 8403, Modeling and Simulation for Defense Systems and Applications VII, 840303, 2012.

A.2 Journal Publications

1. X. Zhang, **H. Hu**, W. Li, and N. K. Dutta, "High-repetition-rate ultrashort pulsed fiber ring laser using hybrid mode locking," Applied Optics, vol. 55, no. 28, pp. 7885-7891, 2016.
2. X. Zhang, **H. Hu**, W. Li, and N. K. Dutta, "Mid-infrared supercontinuum generation in tapered As_2S_3 chalcogenide planar waveguide," Journal of Modern Optics, vol. 63, no. 19, pp. 1965-1971, 2016.
3. W. Li, **H. Hu**, X. Zhang, S. Zhao., K. Fu, and Niloy K. Dutta, "High-speed ultrashort pulse fiber ring laser using charcoal nanoparticles," Applied Optics, vol. 55, no. 9, pp. 2149-2154, 2016.
4. X. Zhang, W. Li, **H. Hu**, and N. K. Dutta, "High-speed all-optical encryption and decryption based on two-photon absorption in semiconductor optical amplifiers," in Optical Communications and Networking, IEEE/OSA Journal of , vol. 7, no. 4, pp. 276-285, 2015.
5. **H. Hu**, X. Zhang, W. Li, and N. K. Dutta, "Simulation of octave spanning mid-infrared supercontinuum generation in dispersion-varying planar waveguides," Applied Optics, vol. 54, no. 11, pp. 3448-3454, 2015.
6. **H. Hu**, W. Li, N. K. Dutta, "Dispersion-engineered tapered planar waveguide for coherent supercontinuum generation," Optics Communications, vol. 324, pp. 252-257, 2014.
7. **H. Hu**, W. Li, and N. K. Dutta, "Supercontinuum generation in dispersion-managed tapered-rib waveguide," Applied Optics, vol. 52, no. 30, pp. 7336-7341, 2013.
8. W. Li, **H. Hu**, and N. K. Dutta. "High speed all-optical encryption and decryption using quantum dot semiconductor optical amplifiers," Journal of Modern Optics, vol. 60, no. 20, pp. 1741-1749, 2013.
9. **H. Hu**, W. Li, S. Ma, and N. K. Dutta, "Coherence Properties of Supercontinuum Generated

in Dispersion-tailored Lead-silicate Microstructured Fiber Taper," Fiber and Integrated Optics, vol. 32, no. 3, pp. 209-221, 2013.

10. W. Li, S. Ma, **H. Hu**, and N. K. Dutta, "All optical latches using quantum-dot semiconductor optical amplifier, " Optics Communications, vol. 285, no. 24, pp. 5138-5143, 2012.
11. W. Li, S. Ma, **H. Hu**, and N. K. Dutta, "All-optical latches based on two-photon absorption in semiconductor optical amplifiers," Journal of the Optical Society of America B, vol. 29, no. 9, pp. 2603-2609, 2012.
12. S. Ma, W. Li, **H. Hu**, N. K. Dutta, "High speed ultra short pulse fiber ring laser using photonic crystal fiber nonlinear optical loop mirror," Optics Communications, vol. 285, no. 12, pp. 2832-2835, 2012.

References

Chapter 1

[1] Kao, K. C. and Hockham, G. A., "Dielectric-fibre surface waveguides for optical frequencies," Electrical Engineers, Proceedings of the Institution of 113(7), 1151-1158 (1966).

[2] Miya, T., Terunuma, Y., Hosaka, T. and Miyashita, T., "Ultimate low-loss single-mode fibre at 1.55 micron," Electron. Lett. 15, 106-108 (1979).

[3] Zhang, X., Hu, H., Li, W. and Dutta, N. K., "Two-photon absorption-based optical logic," Proc. SPIE 9467, Micro- and Nanotechnology Sensors, Systems, and Applications VII, 946731(2015).

[4] Li, W., Hu, H. and Dutta, N. K., "High speed all-optical PRBS generation using binary phase shift keyed signal based on QD-SOA," Proc. SPIE 9202, Photonics Applications for Aviation, Aerospace, Commercial, and Harsh Environments V, 92020O (2014).

[5] Li, W., Hu, H. and Dutta, N. K., "Optical latches using optical amplifiers," Proc. SPIE 8720, Photonic Applications for Aerospace, Commercial, and Harsh Environments IV, 87200O (2013).

[6] Ma, S., Li, W., Hu, H. and Dutta, N. K., "Optical processors using semiconductor optical amplifiers," Proc. SPIE 8403, Modeling and Simulation for Defense Systems and Applications VII, 840303 (2012).

[7] Zhang, X., Li, W., Hu, H. and Dutta, N. K., "High-speed all-optical encryption and decryption based on two-photon absorption in semiconductor optical amplifiers," J. Opt. Commun. Netw. 7(4), 276-285 (2015).

[8] Li, W., Hu, H. and Dutta, N. K., "High speed all-optical encryption and decryption using

quantum dot semiconductor optical amplifiers," J. Mod. Opt. 60(20), 1741-1749 (2013).

[9] Li, W., Ma, S., Hu, H. and Dutta, N. K., "All-optical latches based on two-photon absorption in semiconductor optical amplifiers," J. Opt. Soc. Am. B 29(9), 2603-2609 (2012).

[10] Li, W., Hu, H., Zhang, X. and Dutta, N. K., "High Speed All Optical Logic Gates Using Binary Phase Shift Keyed Signal Based On QD-SOA," International Journal of High Speed Electronics and Systems, 24(03n04), 1550005 (2015).

[11] Li, W., Ma, S., Hu, H. and Dutta, N. K., "All optical latches using quantum-dot semiconductor optical amplifier," Opt. Commun. 285(24), 5138-5143 (2012).

[12] Essiambre, R. and Tkach, R. W., "Capacity trends and limits of optical communication networks," Proceedings of the IEEE, 100(5), 1035-1055 (2012).

[13] Hu, H., Zhang, X., Li, W. and Dutta, N. K., "Simulation of octave spanning mid-infrared supercontinuum generation in dispersion-varying planar waveguides," Appl. Opt. 54(11), 3448-3454 (2015).

[14] Bao, Q., Zhang, H., Wang, Y., Ni, Z., Yan, Y., Shen, Z. X., Loh, K. P. and Tang, D. Y., "Atomic-Layer Graphene as a Saturable Absorber for Ultrafast Pulsed Lasers," Adv. Funct. Mater. 19(19), 3077–3083 (2009).

[15] Hu, H., Zhang, X., Li, W. and Dutta, N. K., "Hybrid mode-locked fiber ring laser using graphene and charcoal nanoparticles as saturable absorbers," Proc. SPIE 9836, Micro- and Nanotechnology Sensors, Systems, and Applications VIII, 983630 (2016).

Chapter 2

[1] Dudley, J. M., Genty, G. and Coen, S., "Supercontinuum generation in photonic crystal fiber," Rev. Mod. Phys. 78(4), 1135-1184 (2006).

[2] Dudley, J. M. and Talor, J. R., [Supercontinuum Generation in Optical Fibers], Cambridge University Press, New York (2010).

[3] Husakou, A. V. and Herrmann, J., "Supercontinuum generation in photonic crystal fibers made from highly nonlinear glasses," Appl. Phys. B 77(2-3), 227-234 (2003).

[4] Hilligsøe, K. M., Andersen, T., Paulsen, H., Nielsen, C., Mølmer, K., Keiding, S., Kristiansen, R., Hansen, K. and Larsen, J., "Supercontinuum generation in a photonic crystal fiber with two zero dispersion wavelengths," Opt. Express 12(6), 1045-1054 (2004).

[5] Genty, G., Lehtonen, M., Ludvigsen, H. and Kaivola, M., "Enhanced bandwidth of supercontinuum generated in microstructured fibers," Opt. Express 12(15), 3471-3480 (2004).

[6] Knight, J. C., Arriaga, J., Birks, T. A., Ortigosa-Blanch, A., Wadsworth, W. J. and Russell, P. S. J., "Anomalous dispersion in photonic crystal fiber," IEEE Photon. Technol. Lett. 12(7), 807-809 (2000).

[7] Kudlinski, A., George, A. K., Knight, J. C., Travers, J. C., Rulkov, A. B., Popov, S. V. and Taylor, J. R., "Zero-dispersion wavelength decreasing photonic crystal fibers for ultraviolet-extended supercontinuum generation," Opt. Express, 14(12), 5715-5722 (2006).

[8] Falk, P., Frosz, M. and Bang, O., "Supercontinuum generation in a photonic crystal fiber with two zero-dispersion wavelengths tapered to normal dispersion at all wavelengths," Opt. Express, 13(19), 7535-7540 (2005).

[9] Chen, Z., Taylor, A. J. and Efimov, A., "Coherent mid-infrared broadband continuum generation in non-uniform ZBLAN fiber taper," Opt. Express 17(7), 5852–5860 (2009).

[10] Knight, J. C., Broeng, J., Birks, T. A. and Russell, P. S. J., "Photonic band gap guidance in optical fibers," Science 282(5393), 1476-1478 (1998).

[11] Diez-Blanco, V., Siegel, J. and Solis, J., "Waveguide structures written in SF57 glass with fs-laser pulses above the critical self-focusing threshold," Appl. Surf. Sci. 252(13), 4523-4526 (2006).

[12] Schott Glass Catalogue, 2003.

[13] Friberg, S. R. and Smith, P. W., "Nonlinear optical glasses for ultrafast optical switches," IEEE J. Quantum Electron. 23(12), 2089-2094 (1987).

[14] Vogel, E. M., Weber, M. J. and Krol, D., "Nonlinear optical phenomena in glass," Phys. Chem. Glasses 32(6), 231–254 (1991).

[15] Petropoulos, P., Ebendorff-Heidepriem, H., Finazzi, V., Moore, R., Frampton, K., Richardson, D., and Monro, T., "Highly nonlinear and anomalously dispersive lead silicate glass holey fibers," Opt. Express 11(26), 3568–3573 (2003).

[16] Kane, D. J. and Trebino, R., "Characterization of arbitrary femtosecond pulses using frequency-resolved optical gating," IEEE J. Quantum Electron. 29(2), 571-579 (1993).

Chapter 3

[1] Dudley, J. M., Genty, G. and Coen, S., "Supercontinuum generation in photonic crystal fiber," Rev. Mod. Phys. 78(4), 1135-1184 (2006).

[2] Dudley, J. M. and Talor, J. R., [Supercontinuum Generation in Optical Fibers], Cambridge University Press, New York (2010).

[3] Zhang, X., Hu, H., Li, W., and Dutta, N. K., "Supercontinuum generation in dispersion-varying microstructured optical fibers," Proc. SPIE 9834, Laser Technology for Defense and Security XII, 98340F (2016).

[4] Hu, H., Li, W., and Dutta, N. K., "Wide-band coherent supercontinuum generation," Proc. SPIE 8733, Laser Technology for Defense and Security IX, 87330C (2013).

[5] Hu, H., Li, W., Ma, S., and Dutta, N. K., "Supercontinuum generation in dispersion-tailored lead-silicate fiber taper," Proc. SPIE 8647, Next-Generation Optical Communication: Components, Sub-Systems, and Systems II, 86470O (2013).

[6] Hu, H., Li, W., and Dutta, N. K., "Coherence Properties of Supercontinuum Generated in Dispersion-tailored Lead-silicate Microstructured Fiber Taper," Fiber and Integrated Optics 32(3), 209-221 (2013).

[7] Coen, S., Chau, A. H. L., Leonhardt, R., Harvey, J. D., Knight, J. C., Wadsworth, W. J. and Russell, P. S. J., "Supercontinuum generation by stimulated Raman scattering and parametric four-wave mixing in photonic crystal fibers," J. Opt. Soc. Am. B 19(4), 753-764 (2002).

[8] Wadsworth, W. J., Ortigosa-Blanch, A., Knight, J. C., Birks, T. A., Man, T. P. M. and Russell, P. S. J., "Supercontinuum generation in photonic crystal fibers and optical fiber tapers: a novel light source," J. Opt. Soc. Am. B 19(9), 2148-2155 (2002).

[9] Yamamoto, T., Kubota, H., Kawanishi, S., Tanaka, M. and Yamaguchi, S., "Supercontinuum generation at 1.55 m in a dispersion-flattened polarization-maintaining photonic crystal fiber," Opt. Express 11(13), 1537-1540 (2003).

[10] Leong, J. Y. Y., Petropoulos, P., Price, J. H. V., Ebendorff-Heidepriem, H., Asimakis, S., Moore, R. C., Frampton, K. E., Finazzi, V., Feng, X., Monro, T. M. and Richardson, D. J., "High-nonlinearity dispersion-shifted lead-silicate holey fibers for efficient 1-μm pumped supercontinuum generation," J. Lightwave Technol. 24(1), 183-190 (2006).

[11] Chen, Z., Ma, S. and Dutta, N. K., "An efficient method for supercontinuum generation in dispersion-tailored Lead-silicate fiber taper," Opt. Commun. 283(15), 3076-3080 (2010).

[12] Price, J. H. V., Feng, X., Heidt, A. M., Brambilla, G., Horak, P., Poletti, F., Ponzo, G., Petropoulos, P., Petrovich, M., Shi, J., Ibsen, M., Loh, W. H., Rutt, H. N. and Richardson, D. J., "Supercontinuum generation in non-silica fibers," Opt. Fiber Technol. 18(5), 327-344 (2012).

[13] Chen, Z., Taylor, A. J. and Efimov, A., "Coherent mid-infrared broadband continuum generation in non-uniform ZBLAN fiber taper," Opt. Express 17(7), 5852-5860 (2009).

[14] Yeom, D. I., Mägi, E. C., Lamont, M. R., Roelens, M. A., Fu, L. and Eggleton, B. J., "Low-threshold supercontinuum generation in highly nonlinear chalcogenide nanowires," Opt. Lett. 33(7), 660-662 (2008).

[15] Hu, J., Menyuk, C. R., Shaw, L. B., Sanghera, J. S. and Aggarwal, I. D., "Maximizing the bandwidth of supercontinuum generation in As_2Se_3 chalcogenide fibers," Opt. Express 18(7), 6722-6739 (2010).

[16] Granzow, N., Stark, S. P., Schmidt, M. A., Tverjanovich, A. S., Wondraczek, L. and Russell, P. S. J., "Supercontinuum generation in chalcogenide-silica step-index fibers," Opt. Express 19(21), 21003-21010 (2011).

[17] Gattass, R. R., Brandon Shaw, L., Nguyen, V. Q., Pureza, P. C., Aggarwal, I. D. and Sanghera, J. S., "All-fiber chalcogenide-based mid-infrared supercontinuum source," Opt. Fiber Technol. 18, 345-348 (2012).

[18] Marandi, A., Rudy, C. W., Plotnichenko, V. G., Dianov, E. M., Vodopyanov, K. L. and Byer, R. L., "Mid-infrared supercontinuum generation in tapered chalcogenide fiber for producing octave-spanning frequency comb around 3 μm," Opt. Express 20(22), 24218-24225 (2012).

[19] Husakou, A. V. and Herrmann, J., "Supercontinuum generation in photonic crystal fibers made from highly nonlinear glasses," Appl. Phys. B 77(2-3), 227-234 (2003).

[20] Hilligsøe, K. M., Andersen, T., Paulsen, H., Nielsen, C., Mølmer, K., Keiding, S., Kristiansen, R., Hansen, K. and Larsen, J., "Supercontinuum generation in a photonic crystal fiber with two zero dispersion wavelengths," Opt. Express 12(6), 1045-1054 (2004).

[21] Fedotova, O., Husakou, A. and Herrmann, J., "Supercontinuum generation in planar rib waveguides enabled by anomalous dispersion," Opt. Express 14(4), 1512-1517 (2006).

[22] Yin, L., Lin, Q. and Agrawal, G. P., "Soliton fission and supercontinuum generation in silicon waveguides," Opt. Lett. 32(4), 391-393 (2007).

[23] Lamont, M. R., Luther-Davies, B., Choi, D. Y., Madden, S. and Eggleton, B. J., "Supercontinuum generation in dispersion engineered highly nonlinear (γ = 10 /W/m) As_2S_3 chalcogenide planar waveguide," Opt. Express 16(19), 14938-14944 (2008).

[24] Diez-Blanco, V., Siegel, J. and Solis, J., "Waveguide structures written in SF57 glass with fs-laser pulses above the critical self-focusing threshold," Appl. Surf. Sci. 252(13), 4523-4526 (2006).

[25] Schott Glass Catalogue, 2003.

[26] Friberg, S. R. and Smith, P. W., "Nonlinear optical glasses for ultrafast optical switches," IEEE J. Quantum Electron. 23(12), 2089-2094 (1987).

[27] Petropoulos, P., Ebendorff-Heidepriem, H., Finazzi, V., Moore, R. C., Frampton, K., Richardson, D. J. and Monro, T. M., "Highly nonlinear and anomalously dispersive lead silicate glass holey fibers," Opt. Express 11(26), 3568-3573 (2003).

[28] Price, J. H. V., Monro, T. M., Ebendorff-Heidepriem, H., Poletti, F., Finazzi, V., Leong, J. Y. Y., Petropoulos, P., Flanagan, J. C., Brambilla, G., Feng, X. and Richardson, D. J., "Non-silica microstructured optical fibers for mid-IR supercontinuum generation from 2 μm-5 μm," Proc. SPIE 6102, 61020A (2006).

[29] Lorenc, D., Aranyosiova, M., Buczynski, R., Stepien, R., Bugar, I., Vincze, A. and Velic, D., "Nonlinear refractive index of multicomponent glasses designed for fabrication of photonic crystal fibers," Appl. Phys. B 93(2-3), 531-538 (2008).

[30] Murphy, T. E., Software available at http://www.photonics.umd.edu.

[31] Mörl, L., Weinert, C. M., Reier, F., Stoll, L. and Nolting, H. P., "Uncladded InGaAsP/InP rib waveguides with integrated thickness tapers for efficient fibre-chip butt coupling," Electron. Lett. 32(1), 36-38 (1996).

[32] Zwanenburg, M. J., Bongaerts, J. H. H., Peters, J. F., Riese, D. and Van der Veen, J. F., "Focusing of coherent x-rays in a tapered planar waveguide," Physica B 283(1), 285-288 (2000).

[33] Bolaños, W., Carvajal, J. J., Mateos, X., Murugan, G. S., Subramanian, A., Wilkinson, J. S., Cantelar, E., Lifante, G., Aguiló, M. and Díaz, F., "$KY_{0.58}Gd_{0.22}Lu_{0.17}Tm_{0.03}(WO_4)_2$ buried rib waveguide lasers," Opt. Mater. 34(2), 475-480 (2011).

[34] Kalashnikov, V. L., Sorokin, E. and Sorokina, I. T., "Raman effects in the infrared supercontinuum generation in soft-glass PCFs," Appl. Phys. B 87(1), 37-44 (2007).

[35] Agrawal, G.P., [Nonlinear Fiber Optics], Academic Press, Burlington, MA (2007).

Chapter 4

[1] Dudley, J. M., Genty, G. and Coen, S., "Supercontinuum generation in photonic crystal fiber," Rev. Mod. Phys. 78(4), 1135–1184 (2006).

[2] Dudley, J. M. and Talor, J. R., [Supercontinuum Generation in Optical Fibers], Cambridge University Press, New York (2010).

[3] Dudley, J. M. and Coen, S., "Coherence properties of supercontinuum spectra generated in

photonic crystal and tapered optical fibers," Opt. Lett. 27(13), 1180-1182 (2002).

[4] Genty, G., Surakka, M., Turunen, J. and Friberg, A. T., "Complete characterization of supercontinuum coherence," J. Opt. Soc. Am. B 28(9), 2301-2309 (2011).

[5] Nakazawa, M., Tamura, K., Kubota, H. and Yoshida, E., "Coherence degradation in the process of supercontinuum generation in an optical fiber," Opt. Fiber Technol. 4(2), 215–223 (1998).

[6] Dudley, J. M. and Coen, S., "Numerical Simulations and Coherence Properties of Supercontinuum Generation in Photonic Crystal and Tapered Optical Fibers," IEEE J. Sel. Topics Quantum Electron. 8(3), 651-659 (2002).

[7] Gu, X., Kimmel, M., Shreenath, A., Trebino, R., Dudley, J., Coen, S. and Windeler, R., "Experimental studies of the coherence of microstructure-fiber supercontinuum," Opt. Express 11(21), 2697-2703(2003).

[8] Corwin, K. L., Newbury, N. R., Dudley, J. M., Coen, S., Diddams, S. A., Washburn, B. R., Weber, K. and Windeler, R. S., "Fundamental amplitude noise limitations to supercontinuum spectra generated in a microstructured fiber," Appl. Phys. B 77(2-3), 269-277(2003).

[9] Newbury, N. R., Washburn, B. R., Corwin, K. L. and Windeler, R. S., "Noise amplification during supercontinuum generation in microstructure fiber," Opt. Lett. 28(11), 944–946 (2003).

[10] Zeylikovich, I., Kartazaev, V. and Alfano, R. R., "Spectral, temporal, and coherence properties of supercontinuum generation in microstructure fiber," J. Opt. Soc. Am. B 22(7), 1453–1460 (2005).

[11] Kobtsev, S. M. and Smirnov, S. V., "Coherent properties of super-continuum containing clearly defined solitons," Opt. Express 14(9), 3968-3980 (2006).

[12] Türke, D., Pricking, S., Husakou, A., Teipel, J., Herrmann, J. and Giessen, H., "Coherence of subsequent supercontinuum pulses generated in tapered fibers in the femtosecond regime," Opt. Express 15(5), 2732–2741 (2007).

[13] Genty, G., Surakka, M., Turunen, J. and Friberg, A.T., "Second-order coherence of supercontinuum light," Opt. Lett. 35(18), 3057–3059 (2010).

[14] Chen, Z., Taylor, A. J. and Efimov, A., "Coherent mid-infrared broadband continuum generation in non-uniform ZBLAN fiber taper," Opt. Express 17(7), 5852-5860 (2009).

Chapter 5

[1] Dudley, J. M., Genty, G. and Coen, S., "Supercontinuum generation in photonic crystal fiber," Rev. Mod. Phys. 78(4), 1135–1184 (2006).

[2] Dudley, J. M. and Talor, J. R., [Supercontinuum Generation in Optical Fibers], Cambridge University Press, New York (2010).

[3] Zhang, X., Li, W., Hu, H. and Dutta, N. K., "Broadband on-chip mid-IR supercontinuum generation," Proc. SPIE 9832, Laser Radar Technology and Applications XXI, 983211 (2016).

[4] Hu, H., Li, W., Zhang, X. and Dutta, N. K., "Broadband Supercontinuum Generation in a Tapered-Rib Lead-Silicate Waveguide," International Journal of High Speed Electronics and Systems 24(3n04), 1550009 (2015).

[5] Hu, H., Li, W. and Dutta, N. K., "Supercontinuum generation in tapered rib waveguide," Proc. SPIE 9202, Photonics Applications for Aviation, Aerospace, Commercial, and Harsh Environments V, 92021C (2014).

[6] Zhang, X., Hu, H., Li, W. and Dutta, N. K., "Mid-infrared supercontinuum generation in

tapered As_2S_3 chalcogenide planar waveguide," J. Mod. Opt. 63(19), 1965-1971 (2016).

[7] Coen, S., Chau, A. H. L., Leonhardt, R., Harvey, J. D., Knight, J. C., Wadsworth, W. J. and Russell, P. S. J., "Supercontinuum generation by stimulated Raman scattering and parametric four-wave mixing in photonic crystal fibers," J. Opt. Soc. Am. B 19(4), 753–764 (2002).

[8] Heidt, A. M., Hartung, A., Bosman, G. W., Krok, P., Rohwer, E. G., Schwoerer, H. and Bartelt, H., "Coherent octave spanning near-infrared and visible supercontinuum generation in all-normal dispersion photonic crystal fibers," Opt. Express 19(4), 3775-3787 (2011).

[9] Ranka, J. K., Windeler, R. S. and Stentz, A. J., "Visible continuum generation in air-silica microstructure optical fibers with anomalous dispersion at 800 nm," Opt. Lett. 25(1), 25-27 (2000).

[10] Mussot, A., Lantz, E., Maillotte, H., Sylvestre, T., Finot, C. and Pitois, S., "Spectral broadening of a partially coherent CW laser beam in single-mode optical fibers," Opt. Express 12(13), 2838-2843 (2004).

[11] Chen, Z., Taylor, A. J. and Efimov, A., "Coherent mid-infrared broadband continuum generation in non-uniform ZBLAN fiber taper," Opt. Express 17(7), 5852–5860 (2009).

[12] Chen, Z., Ma, S. and Dutta, N. K., "An efficient method for supercontinuum generation in dispersion-tailored lead silicate fiber taper," Opt. Commun. 283(15), 3076–3080 (2010).

[13] Leong, J. Y. Y., Petropoulos, P., Price, J. H. V., Ebendorff-Heidepriem, H., Asimakis, S., Moore, R. C., Frampton, K. E., Finazzi, V., Feng, X., Monro, T. M. and Richardson, D. J., "High-nonlinearity dispersion-shifted lead-silicate holey fibers for efficient 1-μm pumped supercontinuum generation," J. Lightwave Technol. 24(1), 183–190 (2006).

[14] Price, J. H. V., Feng, X., Heidt, A. M., Brambilla, G., Horak, P., Poletti, F., Ponzo, G.,

Petropoulos, P., Petrovich, M., Shi, J., Ibsen, M., Loh, W. H., Rutt, H. N. and Richardson, D. J., “Supercontinuum generation in non-silica fibers,” Opt. Fiber Technol. 18(5), 327–344 (2012).

[15] Feng, X., Loh, W., Flanagan, J. C., Camerlingo, A., Dasgupta, S., Petropoulos, P., Horak,P., Frampton, K., White, N. M., Price, J. H., Rutt, H. N. and Richardson, D. J., "Single-mode tellurite glass holey fiber with extremely large mode area for infrared nonlinear applications," Opt. Express 16(18), 13651-13656 (2008).

[16] Hu, J., Menyuk, C. R., Shaw, L. B., Sanghera, J. S. and Aggarwal, I. D., “Maximizing the bandwidth of supercontinuum generation in As_2Se_3 chalcogenide fibers,” Opt. Express 18(7), 6722–6739 (2010).

[17] Granzow, N., Stark, S. P., Schmidt, M. A., Tverjanovich, A. S., Wondraczek, L. and Russell, P. S. J., “Supercontinuum generation in chalcogenide-silica step-index fibers,” Opt. Express 19(21), 21003–21010 (2011).

[18] Xie, S., Tani, F., Travers, J. C., Uebel, P., Caillaud, C., Troles, J., Schmidt, M. A. and Russell, P. S. J., "As_2S_3-silica double-nanospike waveguide for mid-IR supercontinuum generation," Opt. Lett. 39(17), 5216-5219 (2014).

[19] Rudy, C. W., Marandi, A., Vodopyanov, K. L. and Byer, R. L., "Octave-spanning supercontinuum generation in *in situ* tapered As_2S_3 fiber pumped by a thulium-doped fiber laser," Opt. Lett. 38(15), 2865-2868 (2013).

[20] Mori, K., Takara, H. and Kawanishi, S., "Analysis and design of supercontinuum pulse generation in a single-mode optical fiber," J. Opt. Soc. Am. B 18(12), 1780-1792 (2001).

[21] Fedotova, O., Husakou, A. and Herrmann, J., “Supercontinuum generation in planar rib waveguides enabled by anomalous dispersion,” Opt. Express 14(4), 1512–1517 (2006).

[22] Yin, L., Lin, Q. and Agrawal, G. P., “Soliton fission and supercontinuum generation in silicon waveguides,” Opt. Lett. 32(4), 391–393 (2007).

[23] Lamont, M. R., Luther-Davies, B., Choi, D. Y., Madden, S. and Eggleton, B. J., “Supercontinuum generation in dispersion engineered highly nonlinear (γ=10/W/m) As_2S_3 chalcogenide planar waveguide,” Opt. Express 16(19), 14938–14944 (2008).

[24] Zhang, L., Lin, Q., Yue, Y., Yan, Y., Beausoleil, R. G., Agarwal, A., Kimerling, L. C., Michel, J., and Willner, A. E., "On-chip octave-spanning supercontinuum in nanostructured silicon waveguides using ultralow pulse energy," Selected Topics in Quantum Electronics, IEEE Journal of 18(6), 1799-1806 (2012).

[25] Yu, Y., Gai, X., Ma, P., Choi, D. Y., Yang, Z., Wang, R., Debbarma, S., Madden, S. J. and Luther‐Davies, B., "A broadband, quasi‐continuous, mid‐infrared supercontinuum generated in a chalcogenide glass waveguide," Laser & Photonics Rev. 8(5), 792-798 (2014).

[26] Leo, F., Safioui, J., Kuyken, B., Roelkens, G. and Gorza, S. P., "Generation of coherent supercontinuum in a-Si: H waveguides: experiment and modeling based on measured dispersion profile," Opt. Express 22(23), 28997-29007 (2014).

[27] Zhang, L., Yan, Y., Yue, Y., Lin, Q., Painter, O., Beausoleil, R. G. and Willner, A. E., "On-chip two-octave supercontinuum generation by enhancing self-steepening of optical pulses," Opt. Express 19(12), 11584-11590 (2011).

[28] Hu, H., Li, W. and Dutta, N. K., "Supercontinuum generation in dispersion-managed tapered-rib waveguide," Appl. Opt. 52(30), 7336-7341 (2013).

[29] Hu, H., Li, W. and Dutta, N. K., "Dispersion-engineered tapered planar waveguide for coherent supercontinuum generation," Opt. Commun. 324, 252-257 (2014).

[30] Diez-Blanco, V., Siegel, J. and Solis, J., "Waveguide structures written in SF57 glass with fs-laser pulses above the critical self-focusing threshold," Appl. Surf. Sci. 252(13), 4523–4526 (2006).

[31] Vogel, E. M., Weber, M. J. and Krol, D., "Nonlinear optical phenomena in glass," Phys. Chem. Glasses 32(6), 231–254 (1991).

[32] Petropoulos, P., Ebendorff-Heidepriem, H., Finazzi, V., Moore, R., Frampton, K., Richardson, D., and Monro, T., "Highly nonlinear and anomalously dispersive lead silicate glass holey fibers," Opt. Express 11(26), 3568–3573 (2003).

[33] Schott Glass Catalogue, 2003.

[34] Friberg, S. R. and Smith, P. W., "Nonlinear optical glasses for ultrafast optical switches," IEEE J. Quantum Electron. 23(12), 2089–2094 (1987).

[35] Lorenc, D., Aranyosiova, M., Buczynski, R., Stepien, R., Bugar, I., Vincze, A. and Velic, D., "Nonlinear refractive index of multicomponent glasses designed for fabrication of photonic crystal fibers," Appl. Phys. B 93(2-3), 531-538 (2008).

[36] Mörl, L., Weinert, C. M., Reier, F., Stoll, L. and Nolting, H. P., "Uncladded InGaAsP/InP rib waveguides with integrated thickness tapers for efficient fibre-chip butt coupling," Electron. Lett. 32(1), 36–38 (1996).

[37] Zwanenburg, M. J., Bongaerts, J. H. H., Peters, J. F., Riese, D. and Van der Veen, J. F., "Focusing of coherent x-rays in a tapered planar waveguide," Physica B 283(1), 285–288 (2000).

[38] Bolaños, W., Carvajal, J. J., Mateos, X., Murugan, G. S., Subramanian, A., Wilkinson, J. S., Cantelar, E., Lifante, G., Aguiló, M. and Díaz, F., "$KY_{0.58}Gd_{0.22}Lu_{0.17}Tm_{0.03}(WO_4)_2$ buried rib waveguide lasers," Opt. Mater. 34(2), 475–480 (2011).

[39] Jedamzik, R. and Elsmann, F., "Recent results on bulk laser damage threshold of optical glasses," Proc. SPIE 8603, 860305 (2013).

[40] Kane, D. J. and Trebino, R., "Characterization of arbitrary femtosecond pulses using frequency-resolved optical gating," IEEE J. Quantum Electron. 29(2), 571-579 (1993).

[41] Biancalana, F., Skryabin, D. V. and Yulin, A. V., "Theory of the soliton self-frequency shift compensation by the resonant radiation in photonic crystal fibers," Phys. Rev. E 70(1), 016615 (2004).

Chapter 6

[1] P. V. Mamyshev, S. V. Chernikov, and E. M. Dianov, "Generation of fundamental soliton trains for high-bit-rate optical fiber communication lines," IEEE J. Quant. Electron. 27(10), 2347-2355 (1991).

[2] D. J. Jones, S. A. Diddams, J. K. Ranka, A. Stentz, R. S. Windeler, J. L. Hall, and S. T. Cundiff, "Carrier-envelope phase control of femtosecond mode-locked lasers and direct optical frequency synthesis," Science 288(5466), 635–639 (2000).

[3] S. Richter, F. Zimmermann, S. Döring, A. Tünnermann, and S. Nolte, "Ultrashort high repetition rate exposure of dielectric materials: laser bonding of glasses analyzed by micro-Raman spectroscopy," Appl. Phys. A 110(1), 9-15 (2013).

[4] A. Ehlers, I. Riemann, S. Martin, R. Le Harzic, A. Bartels, C. Janke, and K. König, K, "High (1GHz) repetition rate compact femtosecond laser: A powerful multiphoton tool for nanomedicine and nanobiotechnology," J. Appl. Phys. 102(1), 014701 (2007).

[5] S. Nolte, S. Döring, A. Ancona, J. Limpert, and A. Tünnermann, "High repetition rate ultrashort pulse micromachining with fiber lasers," in Advances in Optical Materials, OSA Technical Digest (CD) (Optical Society of America), paper FThC1 (2011).

[6] U. Keller, K. J. Weingarten, F. X. Kartner, D. Kopf, B. Braun, I. D. Jung, R. Fluck, C. Honninger, N. Matuschek, and J. Aus der Au, "Semiconductor saturable absorber mirrors (SESAM's) for femtosecond to nanosecond pulse generation in solid-state lasers," IEEE J. Sel. Topics Quantum Electron. 2(3), 435-453 (1996).

[7] I. N. Duling, III, C.-J. Chen, P. K. A. Wai, and C. R. Menyuk, "Operation of a nonlinear loop mirror in a laser cavity," IEEE J. Quant. Electron. 30(1), 194-199 (1994).

[8] M. E. Fermann, M. L. Stock, M. J. Andrejco, and Y. Silberberg, "Passive mode locking by using nonlinear polarization evolution in a polarization-maintaining erbium-doped fiber," Opt. Lett. 18(11), 894-896 (1993).

[9] S. Y. Set, H. Yaguchi, Y. Tanaka, M. Jablonski, "Laser mode locking using a saturable absorber incorporating carbon nanotubes," IEEE J. Lightwave Technol. 22(1), 51-56 (2004).

[10] J. Sotor, G. Sobon, W. Macherzynski, P. Paletko, K. Grodecki, and K. M. Abramski, "Mode-locking in Er-doped fiber laser based on mechanically exfoliated Sb_2Te_3 saturable absorber," Opt. Mater. Express 4(1), 1-6 (2013).

[11] H. Xia, H. Li, C. Lan, C. Li, X. Zhang, S. Zhang, and Y. Liu, "Ultrafast erbium-doped fiber laser mode-locked by a CVD-grown molybdenum disulfide (MoS_2) saturable absorber," Opt. Express 22(14), 17341-17348 (2014).

[12] Y.-H. Lin, Y.-C. Chi, and G.-R. Lin, "Nanoscale charcoal powder induced saturable absorption and mode-locking of a low-gain erbium-doped fiber-ring laser," Laser Phys. Lett. 10(5), 055105 (2013).

[13] Y.-H. Lin, C.-Y. Yang, S.-F. Lin, W.-H. Tseng, Q. Bao, C.-I. Wu, and G.-R. Lin, "Soliton compression of the erbium-doped fiber laser weakly started mode-locking by nanoscale p-type Bi2Te3 topological insulator particles," Laser Phys. Lett. 11(5), 055107 (2014).

[14] Q. Bao, H. Zhang, Y. Wang, Z. Ni, Y. Yan, Z. X. Shen, K. P. Loh, and D. Y. Tang, "Atomic-Layer Graphene as a Saturable Absorber for Ultrafast Pulsed Lasers," Adv. Funct. Mater. 19(19), 3077–3083 (2009).

[15] Y. M. Chang, H. Kim, J. H. Lee, and Y. W. Song, "Multilayered graphene efficiently formed by mechanical exfoliation for nonlinear saturable absorbers in fiber mode-locked lasers," Appl. Phys. Lett. 97(21), 211102, (2010).

[16] G. Sobon, J. Sotor, and K. M. Abramski, "Passive harmonic mode-locking in Er-doped fiber laser based on graphene saturable absorber with repetition rates scalable to 2.22 GHz," Appl. Phys. Lett. 100(16), 161109 (2012).

[17] A. Martinez, and S. Yamashita, "10 GHz fundamental mode fiber laser using a graphene saturable absorber," Appl. Phys. Lett. 101(4), 041118 (2012).

[18] Y. W. Song, S. Y. Jang, W. S. Han, and M. K. Bae, "Graphene mode-lockers for fiber lasers functioned with evanescent field interaction," Appl. Phys. Lett. 96(5), 051122 (2010).

[19] H.-R. Chen, C.-Y. Tsai, H.-M. Cheng, K.-H. Lin, and W.-F. Hsieh, "Passive mode locking of ytterbium- and erbium-doped all-fiber lasers using graphene oxide saturable absorbers," Opt. Express 22(11), 12880-12889 (2014).

[20] N. H. Park, H. Jeong, S. Y. Choi, M. H. Kim, F. Rotermund, and D.-I. Yeom, "Monolayer graphene saturable absorbers with strongly enhanced evanescent-field interaction for ultrafast fiber laser mode-locking," Opt. Express 23(15), 19806-19812 (2015).

[21] Y.-L. Qi, H. Liu, H. Cui, Y.-Q. Huang, Q.-Y. Ning, M. Liu, Z.-C. Luo, A.-P. Luo, and W.-C. Xu, "Graphene-deposited microfiber photonic device for ultrahigh-repetition rate pulse generation in a fiber laser," Opt. Express 23(14), 17720-17726 (2015).

[22] A. Martinez, K. Fuse, B. Xu, and S. Yamashita, "Optical deposition of graphene and carbon nanotubes in a fiber ferrule for passive mode-locked lasing," Opt. Express 18(22), 23054-23061, (2010).

[23] G. Zhu, H. Chen, and N. Dutta, "Time domain analysis of a rational harmonic mode locked ring fiber laser," J. Appl. Phys. 90(5), 2143-2147 (2001).

[24] Y. Fukuchi and J. Maeda, "Characteristics of rational harmonic mode‐locked short‐cavity fiber ring laser using a bismuth‐oxide-based erbium‐doped fiber and a bismuth‐oxide‐based highly nonlinear fiber," Opt. Express 19(23), 22502-22509 (2011).

[25] Y. Zi, Y. Jiang, C. Ma, G. Bai, Z. Jia, T. Wu, F. Huang, "A dual-wavelength rational harmonic mode-locked fiber ring laser with different repetition frequencies," IEEE Photon. J. 7(2), 1-9(2015).

[26] S. Ma, W. Li, H. Hu, and N. K. Dutta, "Ultra-short pulsed fiber ring laser using photonic crystal fiber," Proc. SPIE 8381, Laser Technology for Defense and Security VIII, 838116 (2012).

[27] X. Zhang, H. Hu, W. Li, and N. K. Dutta, "High-repetition-rate ultrashort pulsed fiber ring laser using hybrid mode locking," Appl. Opt. 55(28), 7885-7891 (2016).

[28] W. Li, H. Hu, X. Zhang, S. Zhao., K. Fu, and Niloy K. Dutta, "High-speed ultrashort pulse fiber ring laser using charcoal nanoparticles," Appl. Opt. 55(9), 2149-2154 (2016).

[29] S. Ma, W. Li, H. Hu, and N. K. Dutta, "High speed ultra short pulse fiber ring laser using photonic crystal fiber nonlinear optical loop mirror," Opt. Commun. 285(12), 2832-2835 (2012).

[30] I. Hernandez-Romano, J. Davila-Rodriguez, D. Mandridis, J. J. Sanchez-Mondragon, D. A. May-Arrioja, P. J. Delfyett, "Hybrid Mode Locked Fiber Laser Using a PDMS/SWCNT Composite Operating at 4 GHz," IEEE J. Lightwave Technol. 29(21), 3237-3242 (2011).

[31] J. Jeon, J. Lee, and J. H. Lee, "Numerical study on the minimum modulation depth of a saturable absorber for stable fiber laser mode locking," J. Opt. Soc. Am. B 32(1), 31-37 (2015).

[32] H. Dong, H. Sun, G. Zhu, Q. Wang, and N. Dutta, "Clock recovery using cascaded $LiNbO_3$ modulator," Opt. Express 12(20), 4751-4757 (2004).